10.35662/unine-thesis-3029

Université de Neuchâtel
Faculté des sciences

Center for Hydrogeology and Geothermics

A thermo-hydro-mechanical analysis of pore pressure development due to mineral deposition in geothermal systems and subduction zones

A doctoral thesis submitted for the degree of
Doctor of Natural Sciences

by

Batoul M. Gisler

Accepted on the recommendation of:

Prof. Stephen A. Miller, University of Neuchâtel, Switzerland

Prof. Benoît Valley, University of Neuchâtel, Switzerland

Prof. Stefan Schmalholz, University of Lausanne, Switzerland

Defended on December 16th 2022

Université de Neuchâtel
Faculté des sciences

Rue Emile-Argand 11
CH-2000 Neuchâtel
doctorat.sciences@unine.ch

IMPRIMATUR POUR THESE DE DOCTORAT

La Faculté des sciences de l'Université de Neuchâtel autorise l'impression de la présente thèse soutenue par

Madame Batoul GISLER

Titre :

"A thermo-hydro-mechanical analysis of pore pressure development due to mineral deposition in geothermal systems and subduction zones"

sur le rapport des membres du jury composé comme suit:

- Prof. Stephen Miller, directeur de thèse, Université de Neuchâtel, Suisse
- Prof. Benoît Valley, Université de Neuchâtel, Suisse
- Prof. Stefan Schmalholz, Université de Lausanne, Suisse

Neuchâtel, le 30 mai 2023

Le Doyen, Prof. R. Bshary

Life is a series of natural and spontaneous changes. Don't resist them; that only creates sorrow. Let reality be reality. Let things flow naturally forward in whatever way they like.

Lao Tzu

Acknowledgments

When I first saw Steve for a PhD thesis in 2017, I was eight months pregnant with my son Louis, and I am grateful to him for giving me a chance rather than making me feel like having children was an obstacle. I am the only author of this thesis, but this work was made possible with the help of my colleagues. I have immense gratitude for Boris Galvàn for introducing me to THMC processes in geothermal reservoirs and Reza Sohrabi for his enthusiasm when it came to numerical modeling and clusters calculations. I also deeply acknowledge the scientific discussions I had with my friend and colleague Thanushika Gunatilake about subduction zones and dehydration processes. I also thank my advising committee for accepting to be part of my jury, reading my work and giving me input and suggestions to improve the manuscript.

I am grateful to my advisor Steve, for his unrelenting love for science, his guidance, his friendship, chillout mood and all his teachings. Most importantly, I thank Steve for his trust in me and his patience towards me, his kindness and empathy, specially through the hard times of child care and Covid. Steve you are the real MVP.

I thank my colleagues for funny and unforgettable moments at the CHYN; namely, Asmae and Dan. I particularly thank dear Thanushika, my office mate and my chillout buddy for all the fun memories together. I thank my children for teaching me to be a mother and all the messiness that goes with it. I thank my husband Christophe for challenging me to do better always. I am also grateful for my family for being present. Lastly, I am infinitely indebted to my parents, who showered me with constant support and encouragement. Their unconditional love has always driven me to do my best and forget the rest. I dedicate this thesis to them.

Résumé

Une gestion optimale des réservoirs géothermiques requiert l'étude de la précipitation des minéraux et de leurs effets sur le comportement du système. En effet, la précipitation des minéraux, plus précisément de la silice, entraîne une diminution de la porosité de la roche et par conséquent pourrait affecter la pression dans le système. Une recherche première confirme que la vitesse de réduction de la porosité est le facteur déterminant une augmentation potentielle de la pression dans le système. Quand la vitesse de réduction de la porosité est assez importante, le système subit une augmentation de pression de sorte que l'écoulement de Darcy est inversé, transportant ainsi la chaleur dans le sens inverse, expliquant ainsi une sous-performance de certains réservoirs géothermiques.

En présence de fracture hydraulique, la diminution rapide de la porosité entraîne d'une part une diminution de la largeur de la fracture et d'autre part l'absence de fuite de fluide de la fracture vers la roche environnante. Cependant, une fois que le transfert de chaleur dans le sens inverse a lieu (dû à l'augmentation de la pression en excès de celle hydrostatique), la largeur de la fracture recommence à croître. Le développement de la surpression dans le système et l'introduction des contraintes de chaleur (en excès) diminuent les contraintes effectives, affaiblissant ainsi la roche et provoquant sa rupture.

Une étude finale des zones de subductions prouve que les tremblements et glissements épisodiques sont liés à la diminution de la porosité de la roche en présence de la précipitation de la silice (en forme de Quartz). En effet, la vitesse de diminution de la porosité est le facteur contrôlant l'augmentation de la pression et par conséquent une diminution des contraintes effectives et la rupture éventuelle de la roche. Une fois que le glissement a lieu, la pression diminue et le processus de précipitation de silica recommence. Ceci est un processus répétitif.

Mots-clés: *Précipitation de silica, Diminution de la porosité, Réservoir géothermique, Fracture hydraulique, COMSOL Multiphysics, Zone de subduction, Tremblements et glissements épisodiques, Quantification des* *incertitudes, Modèles THC.*

Abstract

One fundamental aspect of geothermal reservoir management involves the study of mineral deposition and its controlling factors. Silica, in its various forms, is one of the most studied minerals and its deposition has been linked to porosity reduction and fluid flow impairment. In geothermal systems, heat is exchanged between the porous rock and the fluid leading to shifts in the mechanical behaviour of the rock. The mechanical behaviour of the reservoir rock is further unsettled by the presence of silica (or other mineral) deposition and its resulting pore pressure buildup. In fact, pore pressure may become in excess of hydrostatic thus decreasing the effective stresses and rendering the reservoir rock unstable. This concerning issue is a source of disagreement within the scientific community, where researchers differ in approaches to incorporate porosity reduction in the suite of governing equations describing the geothermal system, and in some cases suggesting simplifications by neglecting the porosity reduction problem. While the simplification may be true in some scenarios, an increasing number of literature agrees on the importance of porosity reduction, its effects on fracture instability, and its link to slow earthquakes or episodic tremors and slip in subduction zones.

Accordingly, the main purpose of this thesis is to reconcile the equations governing the behaviour of the geothermal system with the porosity reduction and evaluate its influence. We introduce a key concept of a time-dependent porosity reduction rate based on the variation of the concentration of deposited silica in the system. That is, the evolution of pore pressure in the geothermal reservoir becomes dependent on this introduced porosity reduction rate, thus affecting the advection term and eventually the effective stresses. Furthermore, geothermal systems are constituted of solid and fluid phases, and include inherent discontinuities, i.e. fractures, and the superposition of several continua, each with its unique properties and constraints but interacting and interchanging fluid, heat and minerals. This thesis extends the porosity reduction study to target fractured geothermal reservoirs and explores its effects on fracture aperture evolution and their stability.

Silica deposition, a primarily temperature-dependent process, is also encountered in subduction zones due to dehydration processes and fluid transport by the subducting slab and the corner flow of the mantle wedge. The study of tremor data in the Cascadia subduction zone shows that slip events vary from large and infrequent to small and frequent with increasing depth. Measured ratios of compressional (P)-wave to shear (S)-wave velocities are in the range of 1.6 and 2.0, decreasing with increasing depth and are proportional to the episodic recurrence intervals. This observation indicates the presence of quartz at greater depth. All evidence shows that porosity reduction via progressive silica enrichment near the base of the forearc crust and upward mineralization of quartz veins enables slow earthquakes at subduction zone forearcs, otherwise called episodic tremor and slip (ETS). Episodic healing and permeability reduction of the silica-rich fault gauge elicit a reduction in tremor recurrence time. At higher temperature, faster silica deposition occurs, leading to faster porosity reduction rates, and consequently faster fluid overpressure. Accordingly, the fault is subjected to lower effective normal stress and hence shorter tremor recurrence times.

In this study, we present numerical simulations of fluid pressure, heat transfer and reactive transport in a geometrically constrained fractured hydrothermal system undergoing time-dependent porosity reduction. We use the finite element based commercial software COMSOL Multiphysics. The simulations explore the effects of porosity reduction which occurs at the vicinity of the injection well, where temperatures are low, on injectivity and fracture stability. The simulation also identifies the controlling factors, such as the porosity reduction rate and the fracture initial aperture, the injection pressure and concentration of silica (as quartz) in excess of the equilibrium concentration. The simulations further highlight the consequences of silica enrichment (porosity reduction) in subduction zones and the resulting heat and fluid flow dynamics. Although fluid in these high enthalpy systems is saline, we opt for water as the modeling fluid.

Simulations results show that porosity reduction rate is the principal controlling factor of the behavior and stability of the hydrothermal system undergoing mineral deposition. In fact, pore pressure can become in excess of hydrostatic and lead to a reverse Darcy flow (in reverse of its presumable direction) at the vicinity of the injection well, overtime decreasing the injectivity rate and producing underperforming wells. Furthermore, excess pore pressure at the fracture boundary brings a decrease in the effective stresses and instability for a range of fracture inclination angles. Finally, fault reactivation and ETS are not large scale events, rather events caused by local variations in porosity and pore pressure. Furthermore, only a time-dependent porosity reduction rate at the subduction zone controls the decrease in the effective stress and causes ETS. Nevertheless, the cycle of fault reactivation then healing is incessant, and faster pore pressure development leads to lower changes in effective stress and hence shorter recurrence times of episodic tremors and slip (ETS).

Keywords: *Silica deposition, Porosity reduction, Geothermal reservoir, Hydraulic fracture, COMSOL Multiphysics, subduction zones, Episodic tremor and slip, Uncertainty quantification, THC models.*

Contents

List of Figures

List of Tables

List of Abbreviations

ETS	**E**pisodic **T**remor and **S**lip
SPARROW	**S**imulator for **P**orosity Reduction and Fracture **A**perture Evolution in a geothermal **R**eservoir with **R**eactive fl**OW**
REV	**R**epresentative **E**lementary and **V**olume
THC	**T**hermo **H**ydro and **C**hemical
FEM	**F**inite **E**lement and **M**ethod
BEM	**B**oundary**E**lement and **M**ethod
PDE	**P**artial**D**ifferential and **E**quations
MC	**M**ohr **C**oulomb

Physical Constants

Density of quartz	$\rho_q = 2700$ kg m^3
Fluid density at reference temperature (at 20°C)	$\rho_0 = 1000$ kg m^{-3}

List of symbols

T	temperature	°C
p	pressure	MPa
C	concentration	ppm
t	time	s
0	initial	
c	critical	
s	specie/mineral	
q	Quartz	
eq	equilibrium	
m	matrix	
adv	advection	
inj	injection	

ϕ	rock-matrix porosity	1
ρ	density	$\mathrm{kgm^{-3}}$
β	bulk compressibility	$\mathrm{Pa^{-1}}$
μ	fluid viscosity	Pas
Ψ	porosity reduction factor	$\mathrm{s^{-1}}$
α	thermal expansion coefficient of the fluid	$\mathrm{K^{-1}}$
λ	thermal conductivity	$\mathrm{kgm^{-3}}$
ν_{js}	stoichiometric reaction coefficient	$\mathrm{Wm^{-1}K^{-1}}$
κ	thermal diffusivity	$\mathrm{m^{2}s^{-1}}$

To my parents

Chapter 1

Introduction

1.1 Objectives

Geothermal systems are regions of both economic and political importance that lessen our dependency on fossil fuel. In these extremely hot systems, rock and fluid interact to transfer heat from the subsurface porous rock to production wells which is ultimately converted into energy. The depth and enthalpy/temperature levels of the system are some of the determining factors when it comes to designing a geothermal application, thus distinguishing between shallow and deep geothermal energy. Both systems allow for heating, cooling and heat storage, except for electrical power generation which requires higher thermal capacities, typically provided by deep geothermal reservoirs (1 MW to >50 MW) in comparison to shallow geothermal reservoirs (<10 kW to <5 MW). Shallow reservoirs are mainly used to heat individual buildings and have free cooling capacities, whereas deep geothermal systems are used for industrial heating networks and provide forced cooling using adsorption and absorption. Deep geothermal systems include high enthalpy reservoirs that are situated in volcanic areas, where an active magmatic heat source is present (Wohletz and Heiken, 1992). These systems are also known for being ore-forming systems (Heinrich et al., 2014; Henley and Ellis, 1983).

The heat stored in the subsurface rock depends on both the porosity (storage coefficient) and the permeability distribution (hydraulic conductivity) and is available year round. Its extraction requires working fluid that can either be naturally supplied by the system itself or artificially supplied by injecting fluids into the earths surface. The difference in density between the cold downward circulating working fluid and the hot geothermal water drives the fluid towards the earths surface (Rybach and Muffler, 1981). This fluid flow process can lead to concomitant instabilities in the reservoir mainly along hydraulic fractures, faults and injection/extraction wells. A sustainable exploitation of this energy requires careful planning and management from the reservoir characterization phase, to the drilling operations and the production phase. Boreholes provide insight into pressure-temperature conditions and the fluid flow in the reservoir. Geothermal project developers rely on geophysical reservoir characterization (fault zones, weak zones, etc.) before deciding whether to invest millions of USD (5-50 Million) on drilling one exploration well (Lubawski and Marzantowicz, 2015); a cost that exponentially increases with increasing depth (Scott, 2017; Tester et al., 2006).

Furthermore, geothermal plants regularly encounter clogging and scaling problems which are detrimental to long term injectivity and productivity of the geothermal system and its sustainable exploitation. Clogging problems are due to precipitation of minerals (i.e. calcite in limestone reservoirs, quartz, dolomite, K-feldspar, amorphous silica, albite and illite) inside the wellbores and equipment, and inside the reservoir itself. Under certain reservoir pressure and temperature conditions, minerals tend to either dissolve or precipitate in the porous reservoir rock, giving rise to thermo-hydro-chemical (THC) processes. These processes also depend on the mineralogy of the reservoir and the injection fluid characteristics (injection rate, temperature, pressure and concentration of minerals) and overtime lead to either reservoir porosity/transmissivity reduction or increase (Walder and Nur, 1984; Ghassemi and Kumar, 2007; Pandey et al., 2014; Rawal and Ghassemi, 2014). Consequently, geothermal development projects rely on mineralogy information to better assess the maintenance cost of the wells and their projected production capacity.

Central to many of the studied minerals is silica, in its various forms. Precipitation and dissolution cycles of silica (as quartz or amorphous silica) have been the highlight of the geothermal scientific community since the early 50s. Indeed, every cycle alters porosity and transmissivity thus affecting injectivity and the performance of the production wells (Robinson and Pendergrass, 1989; Rimstidt and Barnes, 1980; Horne, 1982), as seen at the Hatchobaru and Otake geothermal fields in Japan which identified silica deposition as the most likely cause of lowered permeability near reinjection wells. Furthermore, altered permeability affects the pore pressure in the system and hence, the effective stresses. By placing the mechanical aspect into the behavior of the geothermal system, one is confronted by a fully coupled multiphysics problem, nearly impossible to solve using analytical methods, and even more so to design experimentally. Therefore, scientists rely on numerical methods to predict the behavior of the geothermal system, which becomes even more complex in the presence of fractures. Rock-water complex interactions are modeled by coupling the chemical content of the fluid with heat and fluid flow and ultimately the state of stress of the rock.

In addition, Audet and Bürgmann (2014) demonstrate possible control of subduction zone slow-earthquake periodicity by silica enrichment. A slow earthquake recurs at regular intervals on the plate interface within the forearc of young and warm subduction zones, downdip of the locked zone (Schwartz and Rokosky, 2007; Beroza and Ide, 2011). It is worth pointing out that Audet and Bürgmann (2014) show a linear correlation between the observed forearc v_p/v_s values in Northern Cascadia and the average recurrence times of the slow earthquakes, which decrease with increasing depth. A possible explanation is that the temperature-dependent silica deposition (enrichment)- which prevails near the base of the forearc crust where temperature is high- is reducing the permeability. Consequently, the system undergoes overpressure (pressure in excess of hydrostatic), which lowers the effective normal stress in the high enthalpy system and therefore shortens the recurrence times of the slow earthquakes. As a conclusion, progressive silica enrichment possibly control dilatancy and slow earthquake behavior (Audet and Bürgmann, 2014).

In spite of the extensive research that we will detail in paragraph 1.1, scientists contest incorporating porosity, hence permeability, reduction into this multiphysics modeling problem. While some may agree that porosity reduction must be included in the pore pressure estimation process (Walder and Nur, 1984; Canals and Meunier, 1995; Civan, 2001), the problem lies in the absence of a unique method to calculate the porosity reduction rate and to incorporate it in the pore pressure diffusion equation. Simplifying the mathematics of the problem may seem inconsequential, but the fact that porosity/permeability is a time dependent variable affects the long term behavior of the geothermal system, and must be considered in the numerical solution. Although this theory cannot be discerned true or false without experimental literature, we rely on the well established equations and numerical models at our disposal.

The purpose of this work is to qualitatively and quantitatively understand the important contribution of porosity reduction in pore pressure development due to mineral deposition in fractured geothermal reservoirs. Furthermore, we numerically investigate the relation between porosity reduction due to silica enrichment and slow earthquakes near subduction zones (Audet and Bürgmann, 2014). We examine the role of several controlling factors with a focus on injection fluid pressure, temperature and chemical concentration, as well as the rock characteristics. Despite the many uncertainties at work, we convey the importance of the subject in a series of papers in a geometrically-realistic numerical conceptual setting with an attempt to model overpressure and the resulting effective normal stress in a subduction zone; a topic which is still not adequately addressed.

This chapter provides a brief literature review of previous modeling efforts in mineral dissolution/deposition problems that take place in geothermal systems, specifically silica deposition, and the accompanying porosity, and hence permeability, reduction problem. We present case studies for porosity reduction in geothermal systems and subduction zones to visualize the important issue of slow-earthquake periodicity by silica enrichment. Furthermore, we describe how porosity reduction can be introduced into the system of partial differential equations (PDEs) that we solve using the finite element based commercial software, COMSOL multiphysics. We briefly present its modeling capacities, in particular with the equation based models, meshing options, stability and time step, and precision of the numerical solution. Finally, we detail our Outline.

1.2 State of the art

Numerical modeling of temperature-driven dissolution/precipitation problems in geothermal systems helps to determine the productivity potential of the reservoir. These problems alter reservoir initial porosity and permeability thus affecting the pore pressure, and consequently the effective stress in the system. Simulation efforts can only be achieved based on assumptions of fluid and rock properties that we incorporate in the set of partial differential equations describing the physics of the system. These include, fluid and rock pressure and temperature, injection fluid pressure, temperature and concentration of minerals, equilibrium concentration, and the presence of fractures or other discontinuities in the rock.

A coupled model for reactive transport of multiple chemical species in single phase hydrothermal systems was presented by Steefel (1994) with kinetic precipitation/dissolution reactions. The proposed numerical model couples between the multi component chemical reactions, multiple specie reactive transport, hydrodynamic flow and heat transfer in 1D or 2D. Furthermore, the study examines the precipitation/dissolution reactions-induced porosity and permeability changes in a fractured hydrothermal system. Their result shows that disequilibrium with respect to silica phases are more pronounced at low temperatures and high permeability layers due to the flow velocity. This disequilibrium also depends on fracture spacing in fractured reservoirs and flow rate and is more favorable in widely spaced fractures. A rapid alteration of permeability can prevent the convection cell to attain hydrodynamic or thermal steady state. It is shown that permeability reduction causes the plume to become increasingly diffuse due to the ascending fluids diverging around the cemented zone. In contrast, permeability increases in regions where the temperature of the fluid is high, which can result in instability and channeling of flow. Steefel (1994) point out that these results do not depend on the boundary conditions (concentration of the mineral) but rather on the naturally imposed thermal gradients of the hydrothermal system. Later, Steefel and Lichtner (1998) present a multi-component reactive transport in discrete fractures combining analytical solutions and numerical modeling and establish a method to predict the mineralization along a fracture based on field observations of wall rock alteration. They present a system of equations that best describes the change in effective concentration of precipitated or dissolved minerals in both the matrix and the fracture. Steefel and Lichtner (1998) use a scaling factor, independent from the mineral reaction kinetics to predict the distribution concentrations of mineral zones assuming prior knowledge of the diffusion-controlled mineral zoning in the rock. In a series of publications, Ghassemi and Kumar (2007); Ghassemi, Nygren, and Cheng (2008); Kumar and Ghassemi (2005) present solutions for fracture aperture evolution due to silica deposition in fractured geothermal reservoirs by coupling fluid flow with thermoelasticity and reactive transport. Some of the widely used softwares for coupled modeling of subsurface multi phase, non-isothermal fluid flow, solute transport and chemical reactions, include TOUGHREACT (Xu, 1998) and PFLOTRAN (Hammond, Lichtner, and Mills, 2014). Modeling complex multiphysics problems often requires simplifications and neglecting some aspects of the problem, specially when one wishes to model in 3D.

An important aspect that is yet to be well established is the reservoir scale porosity and permeability reduction and more importantly how to incorporate it into the system of partial differential equations (PDEs) to help explain why some geothermal doublets become underperforming and why we face low injectivity rates near reinjection wells. Walder and Nur (1984) introduce a porosity rate change factor to study pore pressure development due to dissolution/deposition of solutes. By combining this rate factor with mass conservation and Darcy's law, they arrive to a diffusion-type equation for pore pressure which increases when the reservoir undergoes porosity reduction. This rate of porosity change is time dependent as it depends on the evolving concentration of dissolved/precipitated mineral (Canals and Meunier, 1995; Scott and Driesner, 2018). Walder and Nur (1984) suggest that elevated pore pressure (above hydrostatic) due to porosity reduction processes is local and leads to brittle failure and fracturing. By fracturing, one can anticipate a partial relief in terms of pore pressure, but observations show that it does not eliminate pore pressure buildup. Episodic fracturing, healing and sealing is common in much of the crust and affect the compressional waves, as supported by laboratory studies.

A later study by Audet and Bürgmann (2014) finds a linear relation between the compressional/shear waves data and the recurrence time of the episodic tremor and slip (ETS) in the cascadia subduction zone, thus postulating that porosity/permeability reduction due to silica enrichment possibly controls slow earthquake periodicity. Quartz-rich rocks are not abundantly available in lower continental crust and the presence of quartz enrichment is primarily due to the precipitation of fluid dissolved silica derived from the progressive dehydration of the downgoing slab. Note that silica enrichment depends on the subduction zone age, temperature and plate interface depth. The availability of silica is further enhanced by complete serpentinization of the mantle near the wedge corner. Miller et al. (2003) suggest that dehydration is controlled by the presence of a free (drained) boundary and that pore pressure generated from dehydration or melting reactions may cause hydrofracturing, thus influencing the porosity and permeability structure of the dehydrating/melting zone. Peacock (2009) suggests that prograde metamorphic dehydration reactions trigger or enable ETS within the subducting plate as seen in the Cascadia and southwest Japan subduction zones, where tremors occur within the overlying forearc crust where temperatures are lower.

1.3 Geothermal resources and mineral deposition case studies

The study of geochemistry is of great importance in order to insure optimal geothermal energy utilization. For example, water chemistry allows project developers to determine underground temperatures and boiling and mixing relations required in both exploration and production phases (Rybach and Muffler, 1981). Browne (1978) classified the controlling factors of mineral composition in active hydrothermal systems as follows: 1) temperature, 2) pressure, 3) rock type, 4) permeability, 5) fluid composition and 6) duration of activity. Nevertheless, the effect of rock type is temperature dependent and becomes negligible above 280°C, at which a stable suite of minerals exist: albite, K-feldspar, chlorite, Fe-epidote, calcite, quartz, illite, and pyrite. Furthermore, equilibrium between rocks and reservoir fluids is rarely achieved in low permeability reservoirs, as opposed to high permeability reservoirs where water residence times are longer (months and years) at high temperatures (above 200°C) (Rybach and Muffler, 1981). The silica geothermometer is the geochemical thermometer of choice when estimating reservoir temperatures. First an empirical geothermometer was suggested by Bödvarsson (1960) based on silica concentrations in natural thermal waters in Iceland (Rybach and Muffler, 1981), and was extended to a theoretical one based on the work of Morey, Fournier, and Rowe (1962) who tested solubility of quartz in water at the vapor pressure of the solution and Kennedy (1950) who specifically targeted higher temperature systems. It is worth mentioning that studies show that silica concentrations are controlled by quartz solubility based on in geothermal fluids from wells in new Zealand. Figure 1.1 depicts solubility of quartz and amorphous silica as a function of temperature valid for $T = 0 - 250°C$. The quartz geothermometer works best at temperatures above 150°C and may be erroneous when neglecting some key factors, to name a few: 1) temperature range (0-250 °C) 2) steam separation, 3) pH, 4) control of aqueous silica by solids other than quartz, and 5) possible dilution of hot water with cold water before the thermal water reaches the surface. Although the thesis does not cover these factors in detail, we briefly elaborate for completeness. To illustrate the effect of temperature and PH on quartz precipitation, we point out that water reaches equilibrium with quartz in a few hours at 200 °C , in comparison to a few days at 250 °C, also depending on the initial level of super/under saturation and PH level (5-8 are favorable for faster reaction rates) (Rybach and Muffler, 1981). As fluid flows upwards and temperature decreases, quartz precipitation is minimum and amorphous silica is most likely to precipitate. As shown in Figure 1.1, amorphous silica precipitates much faster than quartz for similar temperatures, i.e. a solubility of 115[mg/kg] is registered at 145 °C for quartz and at 25 °C for amorphous silica. That is, water flowing upward from a reservoir at 145 °C will become supersaturated with respect to amorphous silica at 25 °C. Note that Quartz is the most stable and least soluble polymorphic form of silica under pressure/temperature conditions found in most geothermal systems and controls the dissolved silica in temperatures above 150 °C. However, there is not scientific evidence that a pH correction is necessary due to high silica concentration (Rybach and Muffler, 1981). The effect of pH is most pronounced at about 175 °C, where a pH of 7.6 increased the solubility of quartz by 10%. Silica scaling is a problem that hinders the machinery and productivity of geothermal wells. One relevant example is that of the geothermal reservoir in Takinoue, where a power generation of 50 [MWe] was predicted using 11 production wells and 15 injection wells, officially in use since 1978. They measured 500 [mg/kg] of precipitated silica in the separated hot water. Upon experiments, they concluded that the precipitation of silica did not occur in the pipes carrying the hot water from the well, rather from the hot water being exposed to the air. The solution to this problem, was hot water reinjection directly through the pipes connected to the separator and thus avoiding contact with air (Rybach and Muffler, 1981). However, silica deposition inside the reservoir and porosity reduction has been suggested as a precursor for low injectivity and production at Hatchobaru and Otake geothermal fields in Japan (Robinson and Pendergrass, 1989). Nevertheless, scientists are still elaborating methods to design an experiment that would test any tenets of the theory of porosity reduction in order to support or dismiss it.

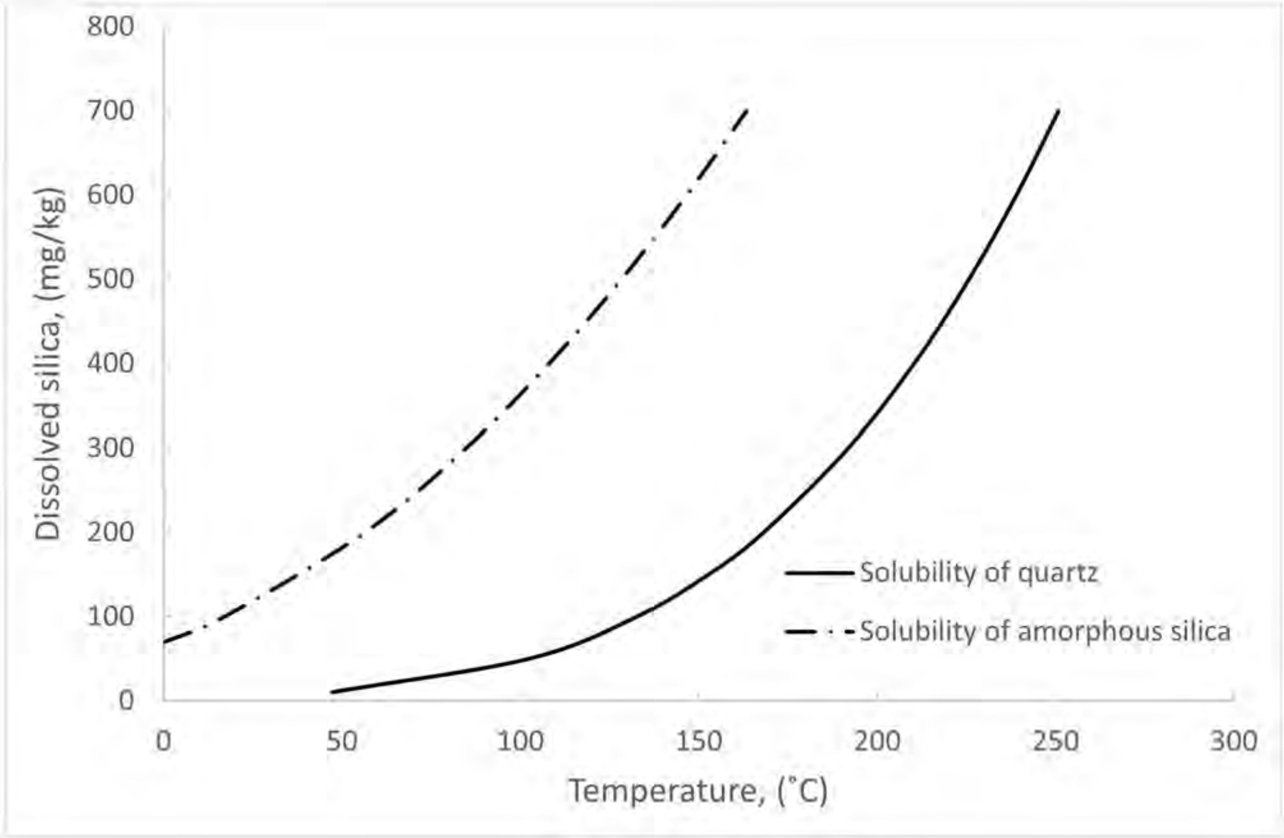

FIGURE 1.1: Concentration of dissolved silica (mg/kg) for quartz and amorphous silica as a function of temperature (Rybach and Muffler, 1981).

1.4 Slow-earthquake periodicity by mineral deposition case studies

Seismicity in high enthalpy systems is fluid driven and is the consequence of a shift in porosity and permeability (Miller et al., 2004, Miller, 2020). Fluids rising from dehydration and melting processes play a crucial role in subduction zone seismicity (Miller et al., 2003; Peacock, 2009; Lee and Kim, 2021). These generated large volumes of fluids introduce an increase in pore pressure and induce hydrofractures, thus affecting the porosity/permeability dynamics of the system. Miller et al. (2003) propose a fluid-pressure feedback model for dehydration processes to describe the evolution of these transient networks and their influence on subduction zone seismicity. Quartz is likely to precipitate in the deep part of the hydrothermal system with temperatures above 250 °C as the solution cools. Literature provides solid evidence that slow earthquakes are triggered by the deposition of minerals in the mantle (Audet and Bürgmann, 2014; Peacock, 2009). As mentioned in paragraph 1.1, it is no coincidence that tremors coincide with mineral deposition in supercritical geothermal systems at subduction zones, where silica enrichment and gold deposits take place. Model established by Audet and Bürgmann (2014) suggests that the faster the permeability reduction, the faster the pore pressure buildup and the smaller the stress drop between slip events. This explains the decrease in recurrence times of ETS with depth. Furthermore, recent studies continue to shed some light on the role of water transport in the subducting zone. In a recent study, Lee, Seoung, and Cerpa (2021) highlights the importance of the corner flow in the deep mantle using a 2D numerical model. They run a series of numerical experiments to quantitatively represent the effects of dehydration of the subducting slab and the mantle wedge using water solubilities of basalt and peridotite. The model provided by Lee, Seoung, and Cerpa (2021) shows that most of the water in the oceanic crust is dehydrated by a depth of 100 km and proves a negligible effects of the convergence rate and age of the subducting slab on the dehydration of the subducting slab. Fluid flux and slab melting are bound to hydrous minerals such as serpentine and chlorite, which are dragged by mantle corner flow to backarc depths and transformed into low water-soluble hydrous minerals (Lee, Seoung, and Cerpa, 2021). Lee and Kim (2021) suggests that deep nonvolcanic tremors in the forearc mantle result from continuous free flow of fluid through the serpentinite layer toward the corner of the mantle wedge.

1.5 Numerical modeling using COMSOL multiphysics

Despite the list of available softwares (as mentioned previously), we opt for COMSOL multiphysics to perform our simulations. COMSOL multiphysics is a finite elements based, top performance software which allows its user a wide variety of physics, coupled or uncoupled with the unique option of designing its own partial differential equations. The advantage of COMSOL multiphysics in our case is the capacity to couple pressure, temperature and concentration variables with the mechanical aspect of the problem. Furthermore, one can estimate the effective stresses to which the boundaries are subjected to (in our case the fractures) and their displacement. Furthermore, porosity is included as a time-dependent variable, the mesh adapts to the solution, the time step stability is fixed. One can choose time dependent or steady state solution, the properties of the fluid change by default with the changing temperature simulated by the software.

1.6 Outline of the thesis

A final comment on the structure of the thesis. Each chapter builds on the previous one and introduces an additional key concept. This thesis is divided into three papers, investigating the effects of porosity reduction due to mineral deposition in fractured geothermal systems. In the first paper we investigate the effects of porosity reduction rate on pore pressure development in a geothermal system with a classic doublet system for heat extraction. In the second paper, we expand the first paper to include hydraulic fracture and study the influence of the porosity reduction rate on fracture aperture and system evolution. The third paper provides a simplified model of a subduction zone subjected to porosity reduction due to silica enrichment and focuses on the change of effective stress to establish a relation between the effective stress and failure slip potential of the fault. For completeness, the appendix includes a paper on uncertainty quantification for a hydraulic fracture geometry, in which we highlight the sensitivity of fractures to the elastic properties of the rock at initial times and to the thermal properties of the geothermal system at later times.

Chapter 2

A thermo-hydro-chemical model with porosity reduction and enthalpy production: Application to silica precipitation in geothermal reservoirs

2.1 Abstract

This work investigates the influence of porosity reduction by silica precipitation on pore pressure development, heat transfer and reactive flow in a geothermal system. Porosity reduction due to silica precipitation can generate excess pore pressure, thus affecting the stability of the rock mass. In addition, porosity reduction increases the thermal diffusivity of the rock, affecting the thermal front, while silica precipitation generates enthalpy. Consequently, the effective stresses associated with solute deposition must be considered for accurate studies of rock failure. We use COMSOL multiphysics to solve the governing equations and explore these complex and interacting processes. We investigate a single-phase, reactive flow model coupled to hydrodynamic flow and heat transfer. Model results show that porosity reduction rate depends on the initial porosity and can lead to overpressure in the matrix, thus reversing the Darcy velocity. This would result in silica deposits on the walls of the well and heat transfer from the reservoir to the well, thus accelerating the cooling front. Consequently, the system observes a drastic decrease in the effective stresses and an increased likelihood of tensile failure of the rock. These results have important implications regarding the long-term thermo-hydraulic properties of geothermal reservoirs.

2.2 Introduction

Typically, geothermal energy is extracted by injecting a fluid into the reservoir, circulating it to absorb stored heat and produce electricity at the surface. After heat extraction, the geothermal fluid is re-injected into the reservoir, leading over time to silica rich fluid. Silica precipitation/scaling often clogs the system, thus reducing efficiency and increasing operating costs. In this work, we numerically investigate this problem of coupled fluid flow, heat transfer and reactive solute transport to quantify silica precipitation problems arising during the lifespan of a geothermal power plant.

The abundant literature in thermo-hydro-chemical modeling contributes to our present understanding of coupled heat and fluid behavior in the presence of reactive transport. Walder and Nur (1984) suggest that porosity, permeability, and pore pressure are time dependent and the increase in pore pressure may cause brittle failure of the rock. However, this is a local and sluggish process rather than a 'large scale' mechanism. Studies of intrusions (Scott and Driesner, 2018) propose porosity reduction is proportional to the mass of precipitated silica (as quartz) and also that initial porosity and permeability of host rocks determine timescale and extent of quartz precipitation. Experimental and modelling studies of precipitation of Gypsum and Quartz (Civan, 2001) lead to a mathematical formulation for porosity reduction that matched empirical observations. Quartz cementation studies and its influence on the porosity of the rock (Canals and Meunier, 1995) estimates the new porosity based on the mass conservation of silica during precipitation and the change in the grain surface area. A separate line of research (Yu and Li, 2001; Costa, 2006; Xu and Yu, 2008) estimates porosity-permeability variation assuming a fractal pore space. In addition, clogging of the system via silica precipitation leads to porosity and permeability reduction, and the consequent overpressure decreases the effective normal stress and can jeopardize well integrity. Reductions in the effective normal stress also promote slip on incipient planes, leading to shear failure within the rock mass (Miller and Nur, 2000; Collettini and Holdsworth, 2004; Miller, 2015). In cases where pore pressure exceeds the minimum principal stress (plus the tensile strength), hydro-fractures occur that propagate in the direction of the maximum principal stress. An important process recognized but not typically considered (Steefel, DePaolo, and Lichtner, 2005; Pandey, Vishal, and Chaudhuri, 2018; Scott and Driesner, 2018) is the contribution of enthalpy to the overall heat transfer and is included in our model.

More complex subjects were investigated by Ghassemi and Kumar (2007); Kumar and Ghassemi (2005) and Rawal and Ghassemi (2014) were they study the effects of silica dissolution/deposition and thermal stress on fracture aperture and reservoir behavior, using advanced numerical methods. Their results exposes the influence of the initial fracture aperture on the solution Ghassemi and Kumar, 2007, where they found that for lower initial values of fracture aperture, the fracture tends to widen at the injection point due to the dominating thermoelastic effects and that the fracture tends to widen at the extraction well due to the prevalent effects of silica dissolution. Further, Ghassemi and Kumar (2007) show that for larger initial values of fracture width, the effects of silica deposition/dissolution were minimal compared to the thermoelastic effects. Furthermore, Kumar and Ghassemi (2005) apply a thermo-hydro-chemical (THC) numerical model for fluid, heat and reactive transport in the fracture-matrix coupled system and compute the changes in fracture aperture while considering silica dissolution and precipitation. Their sensitivity analysis displays the main parameters controlling the fracture aperture evolution, mainly reservoir thermal conductivity, reservoir porosity and effective diffusion coefficient, velocity and initial fracture aperture. Advanced numerical schemes such as finite element methods (FEM) and boundary element methods (BEM) were proposed by Rawal and Ghassemi (2014) to analyze the three-dimensional numerical thermo-poro-chemo-mechanical processes in the geothermal system. Results reveal the transient nature of the effects of silica deposition and dissolution on fracture aperture, clearly showing that fracture width is initially dominated by silica behavior and later becomes controlled by thermoelastic effects.

Although important work was presented in modeling coupled thermo-hydro-chemical processes, in 2D and 3D with advanced numerical schemes, most ignore the porosity reduction source term, which we include in our model. Here, we develop a fully coupled thermo-hydro-chemical (THC) model that examines the coupled effects of porosity and enthalpy changes on the (simplified) mechanical response of the rock-matrix system and show that the behavior of fluid, heat and solute transport is driven by the porosity reduction rate.

2.3 System and modeling approach

The numerical model consists of three main components: 1) a formulation for silica precipitation and equilibrium concentration (solubility), 2) the governing equations for fluid flow, heat transfer and reactive flow, solved using finite element methods, and 3) a model to estimate the time-dependent changes in porosity ϕ of the matrix due to quartz precipitation.

2.3.1 Conceptual model

Although amorphous silica deposits near the injection well, its transport is governed by quartz solubility (Ghassemi and Kumar, 2007). For this reason, we assume that quartz is the main mineral precipitating, and thus affecting the porosity - consequently the permeability of the reservoir. Furthermore, the equilibrium concentration of silica, specifically quartz is exceptionally low (6-14 [mg L^{-1}]) (note that amorphous silica is (100-140 [mg L^{-1}]) (Rawal and Ghassemi, 2014), thus justifying the assumption that the solubility is not affected by changes in pressure. We investigate pore space alteration due to silica (as quartz) precipitation at the vicinity of an injection source

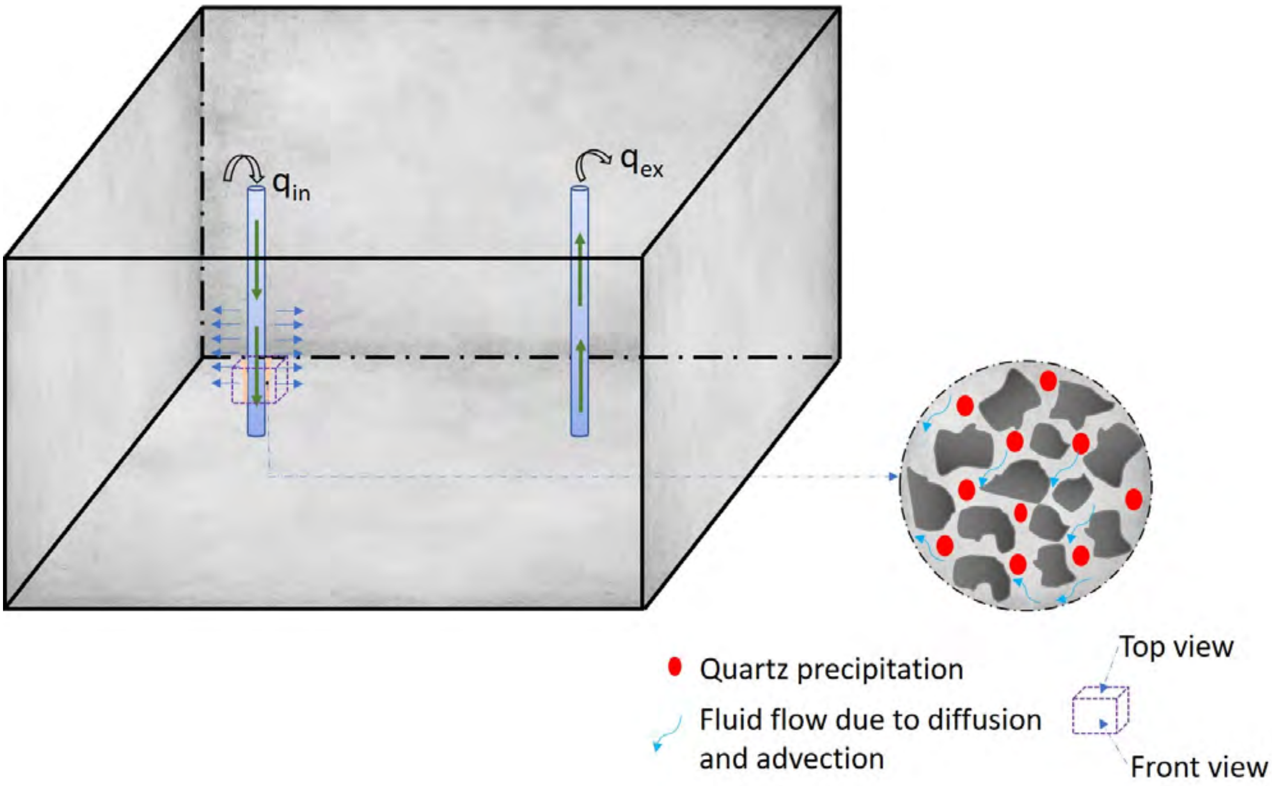

FIGURE 2.1: The conceptual model. Injection into a geothermal doublet system, where precipitation of silica occurs at the injection well (pink region) because of the low temperatures and high pressures (q_{in} is the injection flow rate and q_{ext} is the extraction flow rate). The purple dashed box represents the studied region.

Figure 2.1 illustrates a typical geothermal doublet system, consisting of injection and extraction wells. Silica deposition (in light pink) occurs when the concentration of solute in the injected fluid exceeds the concentration of solute in the pore fluid. Quartz solubility is higher at the outlet (higher temperatures) and silica deposits more at the inlet, where temperature decreases, and pressures are high.

2.3.2 Kinetics of silica deposition

Enhanced geothermal reservoirs typically target granite bedrock rich in quartz, and the reversible silica precipitation-dissolution reaction is:

$$Si(OH)_{4(aq)} <=> SiO_{2(s)} + 2H_2O \tag{2.1}$$

Equilibrium concentration represents the temperature-dependent solubility of quartz in the pore fluid, and is given by (Rimstidt and Barnes, 1980; Robinson and Pendergrass, 1989):

$$C_{eq} = 6 \times 10^4 \times 10^{\left(1.881 - 2.028 \times 10^{-3} T - 1560/T\right)} \tag{2.2}$$

where, C_{eq} is the equilibrium silica concentration [ppm] and T is the initial temperature in the matrix [K].

2.4 Governing equations

The model solves three coupled partial differential equations, one each for pore pressure, temperature and concentration, each described in turn below.

2.4.1 Fluid flow in the reservoir matrix

Mass conservation of fluid in a porous media is the diffusion-type equation:

$$\phi\beta\frac{\partial p}{\partial t} = \frac{k}{\mu}\nabla^2 p + \Psi \tag{2.3}$$

Where p is the excess pore pressure [Pa], k is the matrix permeability [m^2], μ is fluid viscosity [Pa s] and β is the bulk compressibility modulus [Pa^{-1}]. Ψ is the source term given by (Walder and Nur, 1984):

$$\Psi = -\frac{\partial \phi}{\partial t} \tag{2.4}$$

Where Ψ is the porosity reduction factor [s^{-1}], assumed positive when porosity is decreasing. Darcy velocity ($\mathbf{u}$) is:

$$\mathbf{u} = -\frac{k}{\phi\mu}\left(\nabla p - \rho_f g \mathbf{e}\right) \tag{2.5}$$

Where ρ_f is the fluid density [kg m^{-3}], g is gravity acceleration [m^2 s^{-1}] and **e** is the unit vector [ ], oriented in the vertical direction.

2.4.2 Solute transport in the matrix

Although amorphous silica is precipitating at the wellbore wall (Ghassemi and Kumar, 2007) the precipitation of silica is controlled by quartz kinetics away from the well. Quartz has a low solubility and hence one can neglect pressure effects on solubility. once precipitation occurs, depositin is rapid

Advection-diffusion of the solute mass is given by (Steefel, DePaolo, and Lichtner, 2005):

$$\frac{\partial\left(\phi_m C_j^m\right)}{\partial t} = \nabla.\left(\phi_m D_m \nabla C_j^m\right) - \nabla.\left(\phi_m u C_j^m\right) - \sum_{s=1}^{N_s} \nu_{js} r_s \tag{2.6}$$

Where ϕ_m is matrix porosity [1], D_m is the effective solute diffusion coefficient in the rock matrix [m^2 s^{-1}], **u** is Darcy velocity vector [m s^{-1}], C_j^m is the concentration of chemical specie j in the matrix m [ppm], ν_{js} is a stoichiometric reaction coefficient [1], and r_s is the reaction rate of mineral s [kg m^{-3} s^{-1}]. While $\Psi \neq 0$ and assuming linear reaction kinetics, (Eq. 2.6) is rewritten as (Steefel and Lichtner, 1998, Kumar and Ghassemi, 2005, Ghassemi and Kumar, 2007):

$$\frac{\partial\left(\phi_m C_m^{'}\right)}{\partial t} = \nabla\cdot\left(\phi_m D_m \nabla C_m^{'}\right) - \nabla\cdot\left(\phi_m u C_m^{'}\right) - K_m C_m^{'} \tag{2.7}$$

Where K_m is the silica reaction rate [s^{-1}], and $C_m^{'}$ is the effective concentration of the chemical specie in the matrix [ppm] and is given by:

$$C_m^{'} = C_m - C_m^{eq} \tag{2.8}$$

Where C_m^{eq} is the equilibrium concentration [ppm] in the matrix (Eq.2).

2.4.3 Heat transport in the reservoir matrix

The complete form of conservation of energy is given by (Steefel, DePaolo, and Lichtner, 2005):

$$\left[(1-\phi_m){C_p}^m\rho_m + \phi_m {C_p}^f\rho_f\right]\frac{\partial T}{\partial t} = \nabla.\left(\lambda\nabla T\right) - \nabla.\left(\rho_f C_p^f \phi_m u T\right) + \sum_{s=1}^{N_s}\Delta H_s r_s \tag{2.9}$$

Where ΔH_s is the enthalpy of reaction [J kg^{-1}], λ is the thermal conductivity [W m^{-1} K^{-1}], C_p is the specific heat [J kg^{-1} K^{-1}], ρ is the density [kg m^{-3}], subscripts m and f are for matrix (rock) and fluid respectively, and r_s is the volume-normalized quartz reaction rate [kg m^{-3} s^{-1}] given by (Scott and Driesner, 2018):

$$r_s = \phi_m . \frac{\Delta m_{rock}^{SiO_2}}{\Delta t} \tag{2.10}$$

Where $\Delta m_{rock}^{SiO_2}$ is the mass of silica precipitated in the system [kg of SiO_2 per m^3 of fluid] (Scott and Driesner, 2018):

$$\Delta m_{rock}^{SiO_2} = m_{adv}^{SiO_2} - m_{eq}^{SiO_2} \tag{2.11}$$

The equation of state for the fluid density is (Simpson, 2017):

$$\rho_f = \rho_0(1 - \alpha T) \tag{2.12}$$

Where α is the thermal expansion coefficient of the fluid [°C^{-1}], T is the temperature of the fluid [°C], and ρ_0 is the pore fluid density at the reference temperature [kg m^{-3}].

2.5 Algorithm flowchart

Figure 2.2 shows the model flowchart (assuming incompressible and supersaturated fluid) of the coupled governing equations for pressure, concentration and temperature.

1. Evaluate the porosity reduction rate Ψ and calculate the new permeability of the rock matrix.
2. Add the porosity reduction source term to the pressure diffusion equation and calculate p.
3. Derive Darcy velocities.
4. Couple conservation of solute mass with fluid flow and the transient porosity of the matrix to calculate the effective silica concentration $C_m^{'}$.
5. Multiply the enthalpy of the reaction by the effective silica concentration, then introduce to the conservation of energy equation.
6. Couple conservation of energy with fluid flow and the transient porosity to solve the Temperature T.

Repeat the process for the next time step t+Δ t.

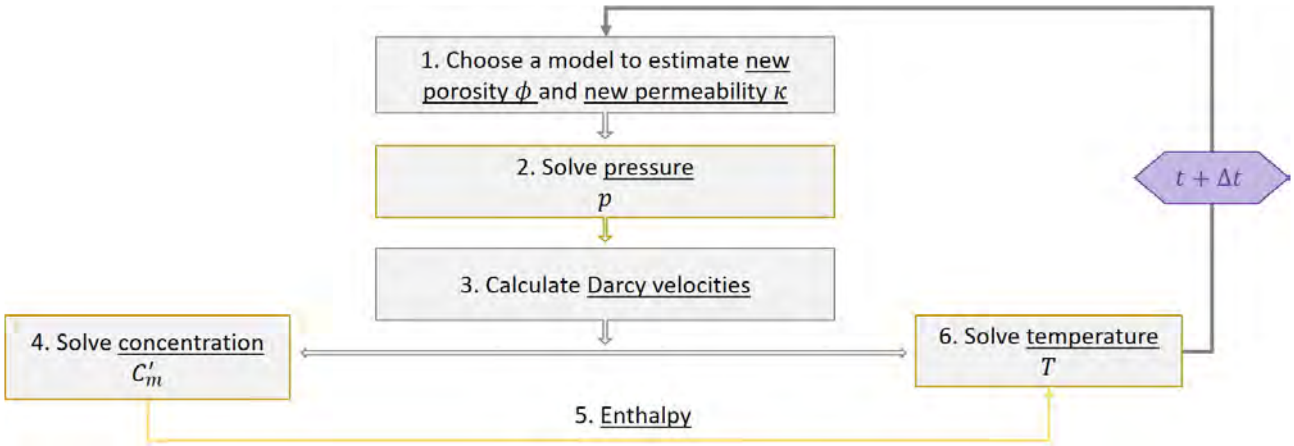

FIGURE 2.2: Algorithm flowchart of the THC model at a given time step (see text for details).

2.6 Numerical simulation

We use COMSOL multiphysics to solve the coupled partial differential equations (PDEs) describing the system, employing an explicit formulation of the finite element method and define the porosity as a time-dependent variable. Note that the system is characterized by non-isothermal and single-phase fluid flow.

TABLE 2.1: Rock properties for the THC model. Subscript m, matrix (rock). (a) (Rawal and Ghassemi, 2014), (b) (Kumar and Ghassemi, 2005)

Initial porosity of the rock, ϕ_o	$0.05\text{-}0.1^{(b)}\text{-}0.2^{(a)}$
Reaction rate constant in the rock matrix, K_m	10^{-6} $s^{-1(b)}$
Initial matrix permeability, k_o	10^{-16} m^2
Density of the rock, ρ_m	2600 kg m^{-3}
Compressibility of the rock, β_m	1.10^{-10} Pa^{-1}
Effective solute diffusion coefficient, D_m	5.10^{-6} m^2 $s^{-1(a)}$
Heat capacity of the solid, C_p^m	1000 J kg^{-1} K^{-1}
Solid heat conductivity, λ	2.6 J m^{-1} K^{-1}

TABLE 2.2: Fluid properties for the THC model. Subscript f, fluid.

Injection fluid pressure, P_{inj}	10 MPa
Compressibility of the fluid, β_f	5.10^{-10} Pa^{-1}
Fluid heat capacity, C_p^f	4000 J kg^{-1} K^{-1}
Thermal expansion coefficient of the fluid, α at 20°C	210.10^{-6} °C^{-1}
Fluid density at reference temperature (at 20 °C), ρ_0	1000 kg m^{-3}
Temperature of the injected fluid, T_{inj}	40 °C

Tables 2.1 and 2.2 show the rock and fluid input properties. Table 2.3 shows the silica (as quartz) kinetics related data which will enable us to calculate the effective concentration of silica from Eq. 2.7

TABLE 2.3: Quartz related data chosen for the THC model. Subscript q, quartz; m, matrix and s for mineral.

Equilibrium concentration of solute, C_m^{eq}	253 ppm
Concentration of silica in the supersaturated fluid, C_{inj}	1000 ppm
Density of quartz, ρ_q	2700 kg m^{-3}
Enthalpy of the reaction, ΔH_s	0.9.10^6 J kg^{-1}

and 2.8. The enthalpy of the reaction is taken from Manning in (Manning, 1994; Scott and Driesner, 2018).

2.7 Model geometry and setup

We develop a 1D model to study the multi-component reactive flow problem. We opt for the 1D solution rather than an axisymmetric solution to save both modeling and computational resources as our future goal is to study the effect of silica deposition and porosity reduction on a 1D fracture aperture evolution. The geometry (Figure 2.3) shows a constant fluid pressure applied at the left ($x = 0$) and no flow boundary conditions on the top and bottom boundaries. Because porosity reduction is a local problem, we study the system for a short distance L=10 [m], and constrain a no flow boundary condition on the right boundary ($x = L$).

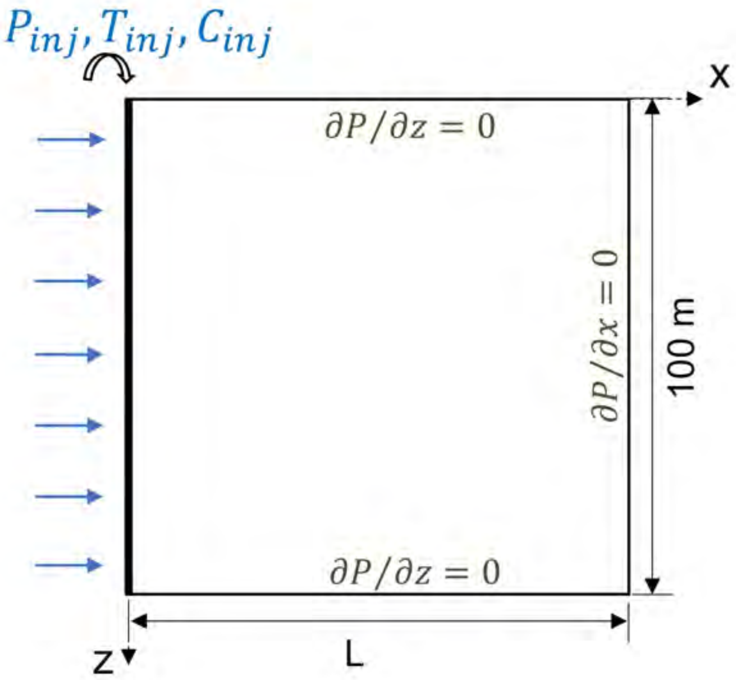

FIGURE 2.3: Front view (Figure 1) model geometry showing a constant fluid injection pressure P_{inj} in the well and no flow boundary conditions at the top, bottom, and right. T_{inj} and C_{inj} describe the temperature, and silica concentration in the well, respectively.

Although the injection temperature at the surface is 40[°C], the temperature at the studied depth of 5[km] is calculated with the following expression (Satman et al., 2017; Jansen and Miller, 2017):

$$T(z) = T_{surf} + \alpha z - \alpha A + \left(T_{inj} - T_{surf} + \alpha A\right) e^{(-z/A)} \tag{2.13}$$

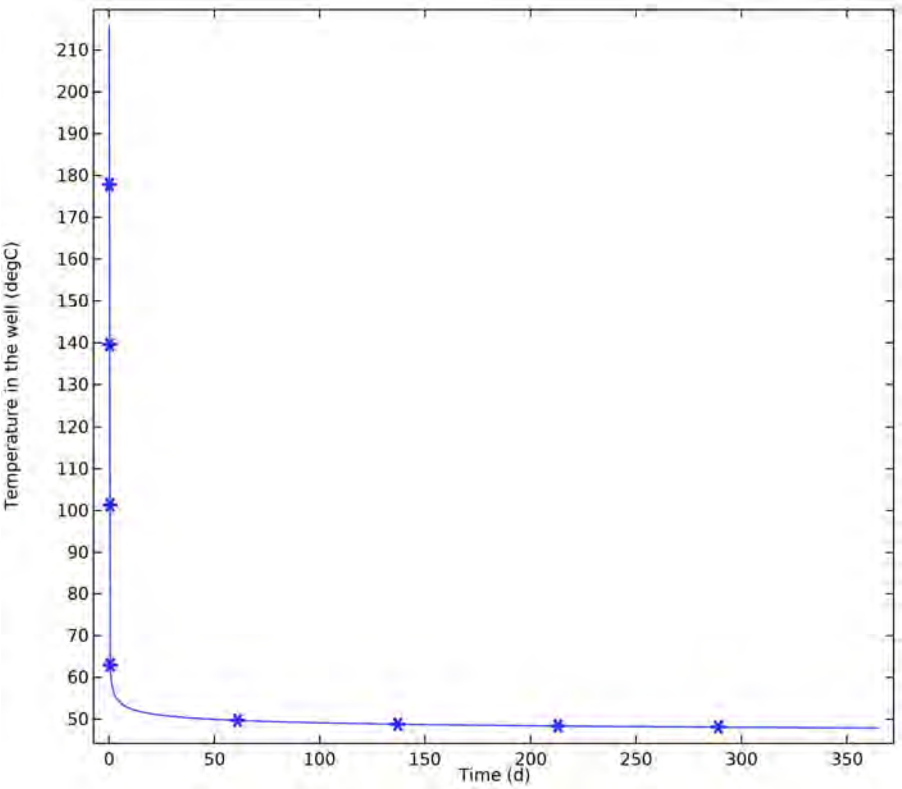

FIGURE 2.4: Temperature in the well at 5[km] depth assuming a discharge rate of 40[kg s^{-1}] and an injection temperature of 40[°C]. The temperature in the well reaches 48[°C] after 365 days of injection.

Assuming a silica rich fluid is injected into the reservoir from the surface with a temperature T_{inj}. The injection temperature at the studied depth z is time-dependent as per (Kutun, Tureyen, and Satman, 2014) and Figure 2.4 shows the results for time-dependent temperature at the injection well for 1 year of injection. Where z is the depth downwards from the top of the well [m] , T_{surf} is the surface temperature and T_{inj} is the injection temperature, both in [°C], α is the geothermal gradient [°C m^{-1}], and A is defined as:

$$A = \frac{Qc_f f(t)}{2\pi\lambda} \tag{2.14}$$

Where Q is the mass flow rate [kg s^{-1}], C_f^p [J kg^{-1} $°C^{-1}$] is the heat capacity of the fluid and λ [J m^{-1} $°C^{-1}$] is the thermal conductivity of the formation. The time-dependence is embedded in the dimensionless time function f(t) [1] describing transient heat transfer, given as (Kutun, Tureyen, and

Satman, 2014):

$$f(t) = ln\left(1 + 1.7\sqrt{t_D}\right) \tag{2.15}$$

Where t_D is dimensionless time:

$$t_D = \frac{\kappa t}{r_w^2} \tag{2.16}$$

Where κ is the thermal diffusivity of the formation [$m^2\ s^{-1}$] and r_w [m] is the well radius. The temperature profile depends on the thermal gradient, and fluid and well input properties given in Table 2.4.

TABLE 2.4: Well and fluid input parameters to estimate the temperature at a depth of 5 [km] via Eq. 2.13

Temperature at the surface, T_{surf}	20 °C
Injection Temperature, T_{inj}	40 °C
Geothermal gradient, α	$0.04\ °C\ m^{-1}$
Depth, z	5000 m
Discharge rate, Q	$40\ kg\ s^{-1}$
Specific heat capacity of the fluid, C_f	$3160\ J\ kg^{-1}\ °C^{-1}$
Mean thermal conductivity of the formation, λ	$2.6\ J\ m^{-1}\ s^{-1}\ °C^{-1}$
Radius of the well, r_w	0.1 m
Mean thermal diffusivity of the formation, κ	$1.1e\text{-}6\ m^2\ s^{-1}$

This step allows for a more accurate Temperature boundary condition at the inlet of the studied region. Fluid circulates in the system and will later be extracted at the extraction end of this geothermal doublet.

2.8 Transient porosity and permeability in the matrix

We perform our study with two distinct porosity reduction models among a suite of published porosity reduction models (Walder and Nur, 1984; Canals and Meunier, 1995; Koponen, Kataja, and Timonen, 1997; Steefel and Lichtner, 1998; Civan, 2001; Steefel, DePaolo, and Lichtner, 2005; Scott and Driesner, 2018). Note that the purpose here is not to study the reliability of the models, rather to test how different porosity reduction rates can influence the response of the system.

Porosity reduction models

1. The first concentration-based model estimates porosity variations in the system as proportional to the mass of precipitated quartz.The rate of porosity reduction in the medium is written as

(Steefel, DePaolo, and Lichtner, 2005):

$$\frac{\partial \phi}{\partial t} = V_m R_s \tag{2.17}$$

Where V_m is the molar volume of SiO_2 taken as 28.10^{-6} [m^3 mol^{-1}] and R_s is the volume-normalized mineral reaction rate [mol m^{-3} s^{-1}] given by (Scott and Driesner, 2018):

$$R_s = \phi . \frac{\Delta m_{rock}^{SiO_2}}{\Delta t} . \frac{10^3}{M_{quartz}} \tag{2.18}$$

Where M$_{quartz}$ is the molar mass of SiO_2 (0.06008 [kg mol^{-1}]).

2. The second model we use is the analytical formulation based on precipitation in pore bodies and pore throats in a representative elementary volume (REV) (Civan, 2001). Transport processes depend on rock porosity and permeability, and both are affected by precipitation because of pore volume and pore surface area changes (Civan, 2001). This model estimates the precipitation-induced porosity based on the initial porosity of the matrix, the lumped silica precipitation rate coefficient k$_\phi$ [s^{-1}], and a lumped parameter r [1] under saturation conditions. The model compared well with empirical data measured on several cores of gypsum and quartz. Assuming a constant saturation ratio ($C_{inj} > C_0$) and k_ϕ=K_m, porosity reduction is written as: (Civan, 2001):

$$\phi^{-r} = \phi_0^{-r} + k_\phi t \tag{2.19}$$

   where r=0.81, k_ϕ=10^{-6} [s^{-1}], ϕ_0 is the reference porosity and t is time [s]. Note that r and k_ϕ depend on the initial porosity in the system. The presented simplification is for numerical purposes and to visualize the behavior of the system for a higher porosity reduction rate.

Permeability estimation

The permeability variation depends on the precipitation-induced porosity (Civan, 2001), and empirically found as (Weir and White, 1996; Scott and Driesner, 2018):

$$k = k_0 \left\{ 1 - \left[1 - \left(\frac{\phi - \phi_c}{\phi_0 - \phi_c} \right)^{1.58} \right] \right\}^{0.46} \tag{2.20}$$

Where ϕ_c is the critical porosity defined as half of the initial porosity, ϕ_0 is the initial porosity and k_0 is the initial permeability [m^2]. The stability of the solution requires that the transient porosity does not go lower than the critical porosity.

2.9 Results and Discussions

We solve the coupled partial differential equations (PDEs) describing the system using COMSOL multiphysics equation-based module. We introduce the porosity as a variable via model 1 for three sets of initial porosities; 5%, 10% and 20% and via model 2 for two sets of initial porosities 5% and 10% (because we ignore values of r and k_ϕ for ϕ_0=0.2). The simulation begins by comparing the porosity reduction rates between the two suggested models (Eq.2.17 and Eq.2.20), shown in Figure 2.5. We choose a simulation length of 1 year because silica scaling removal is standard practice in the field and therefore our boundary conditions of C_{inj} may not be further applicable.

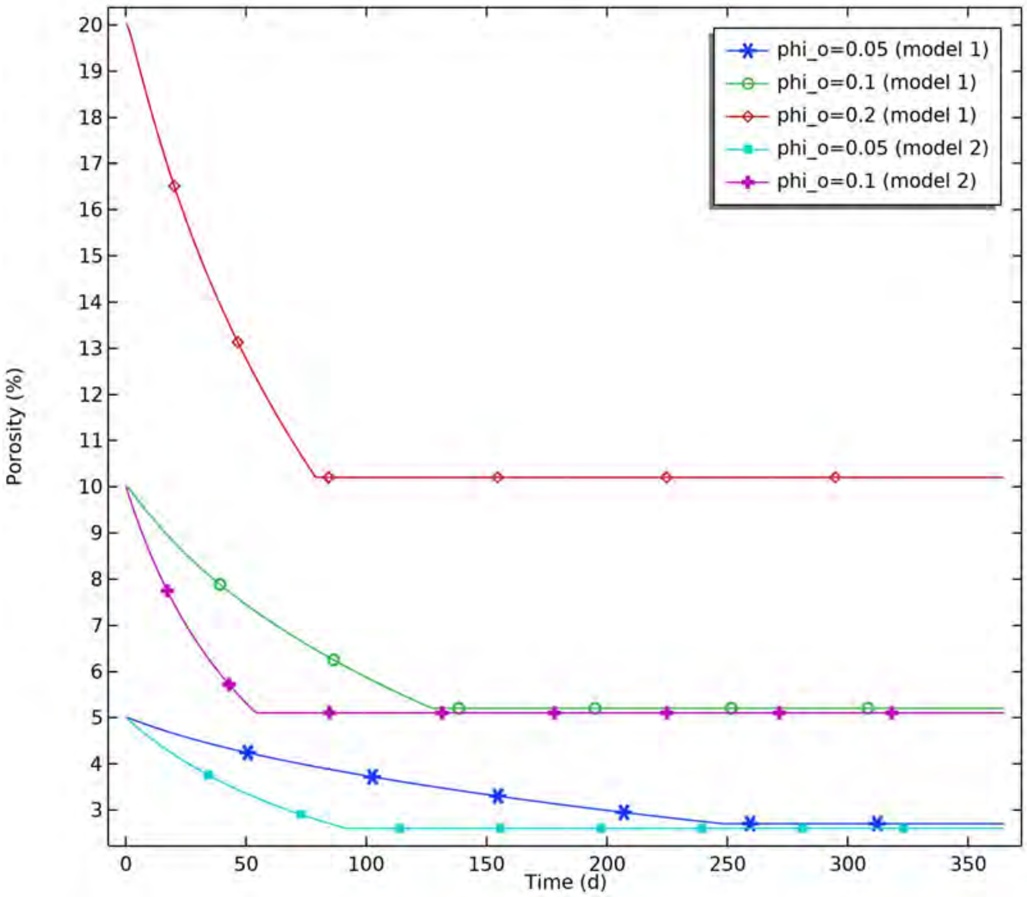

FIGURE 2.5: Comparison between the two different porosity reduction models for three different initial values of porosity: 5%, 10% and 20% (model 1) and two initial porosity: 5%, 10% (model 2).

Figure 2.5 shows that, for either models, porosity reduction rate is faster for higher initial values of porosity (ϕ_o=0.1). However, model 2 estimates a significantly faster porosity reduction rate. According to model 1, porosity is reduced by half after 80 days of injection for an initial porosity of 20%, and after 130 days of injection for an initial porosity of 10%, and after 250 days of injection for an initial porosity of 5%. For a faster porosity reduction rate (model 2), porosity is reduced by half after 55 days of injection for an initial porosity of 10%, and after 90 days of injection for an initial porosity of 5%. We present the results of each porosity reduction model to highlight the difference in porosity reduction rates. Porosity reduction rate is the first predictor of a potential overpressure in the system and hence lower injectivity. From Figure 2.5 we can confidently deduce that model 2 will present higher overpressure (in excess of hydrostatic) than model 1 because of the higher porosity reduction rate.

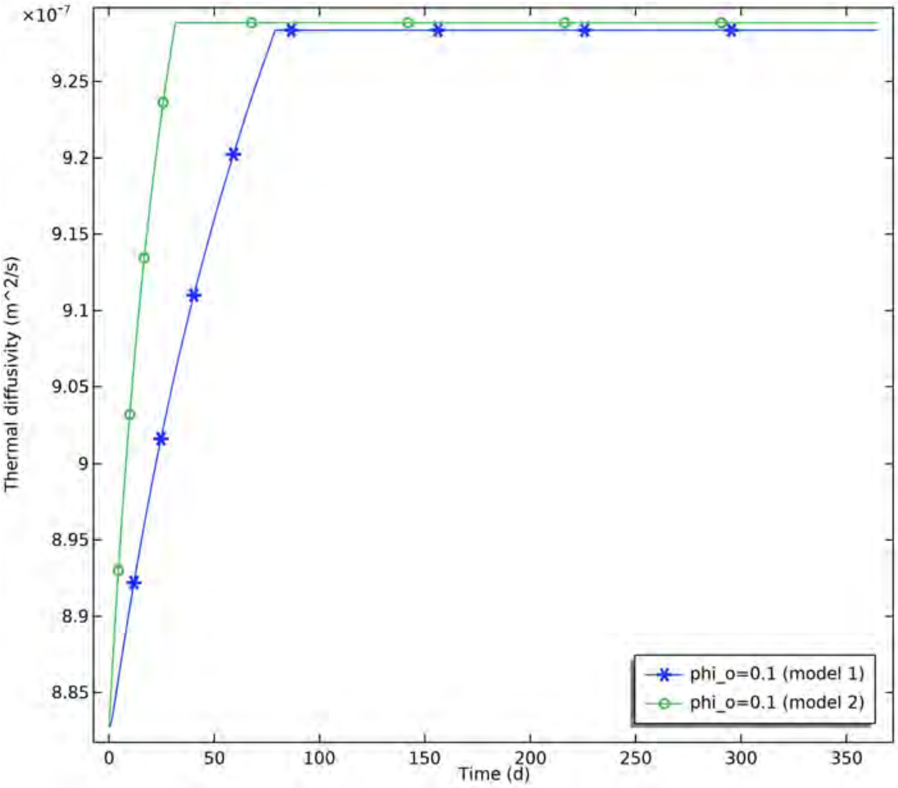

FIGURE 2.6: Comparison of the thermal diffusivity [m^2 s^{-1}] between the two different porosity reduction models for initial porosity 10%.

Next, we study the evolution of the thermal diffusivity because it is inversely proportional to the decreasing porosity. The evolution of the thermal diffusivity may, among other factors, affect the temperature evolution in the system. We show the common case for ϕ_o=0.1 for models 1 and 2. As predicted, Figure 2.6 shows an increase in thermal diffusivity [m^2 s^{-1}] in the system for both models (assuming initial porosity 10%). The effect is present but almost negligible with almost 4.6% increase (for both models) from the initial diffusivity at time t= 0[d].

2.9.1 1D THC simulation near a silica-rich cooling injection source: model 1

We compare pressure, concentration and temperature results between two scenarios, one with constant porosity and one with transient porosity (model 1), and each evaluated for initial porosity 5%, 10% and 20%. Because porosity and permeability are decreasing in the system, the source term in Eq.2.3 increases and results in overpressure.

Figure 2.6[a] shows the fluid pressure diffusion in the system p at 1[m] from the source over 1 year of injection. Overpressure starts within the first 6 days after injection for all porosities, with the earliest occuring for ϕ_o=0.05. Figure 2.6(a) also shows the maximum overpressure in the system 11.5[MPa] for ϕ_o=0.2 after 60 days of simulation, and 10.32[MPa] for ϕ_o=0.1 after 80 days of injection and of 10.08[Mpa] for ϕ_o=0.05 after 100 days of injection. Then, the rate of overpressure steadily decreases with time and is more detectable for the higher porosity reduction rate (initial porosity 20%). When porosity decreases due to silica deposition, the potential to accommodate deposited silica decreases. That is, the effective concentration of deposited silica decreases (Eq.2.7), as observed in Figure 2.6[b]. Figure 2.6[b] shows that the effective silica concentration [ppm] at 1[m] from the source is smaller for the transient porosity scenario (model 1). The difference in effective silica concentration depends on both the initial porosity and the porosity reduction rate, and is the highest for the initial porosity of 5%. After 365 days of injection, the decreasing porosity reduces the effective concentration of deposited silica by 32% for ϕ_o=0.2, 42% for ϕ_o=0.1 and by 48% for initial porosity of ϕ_o=0.05. However, the effective concentration line graph reaches equilibrium faster for ϕ_o=0.2.

Figure 2.6[c] shows transient temperature is cooler for the transient porosity scenario (model 1), with the largest difference occurring for ϕ_o=0.2 due to the higher porosity reduction rate. A possible reason for this decrease in both the concentration and temperature rests in the overpressure: a reverse Darcy flow takes place and fluid transports heat and silica from the matrix to the source boundary. Note that the negative advection term is accounted for in our model. Finally for model 1, we show simulated values of pressure [MPa], effective silica concentration [ppm] and temperature [°C] along the distance L=10[m] (Figure 2.6) with the initial and boundary conditions (Figure 2.3).

Figure 2.6[a] shows the overpressure in the system 11.2[MPa] for ϕ_o=0.2 after 1 year of simulation, and 10.2[MPa] for ϕ_o=0.1 and of 10.02[Mpa] for ϕ_o=0.05, calculated at the distance of 10[m].

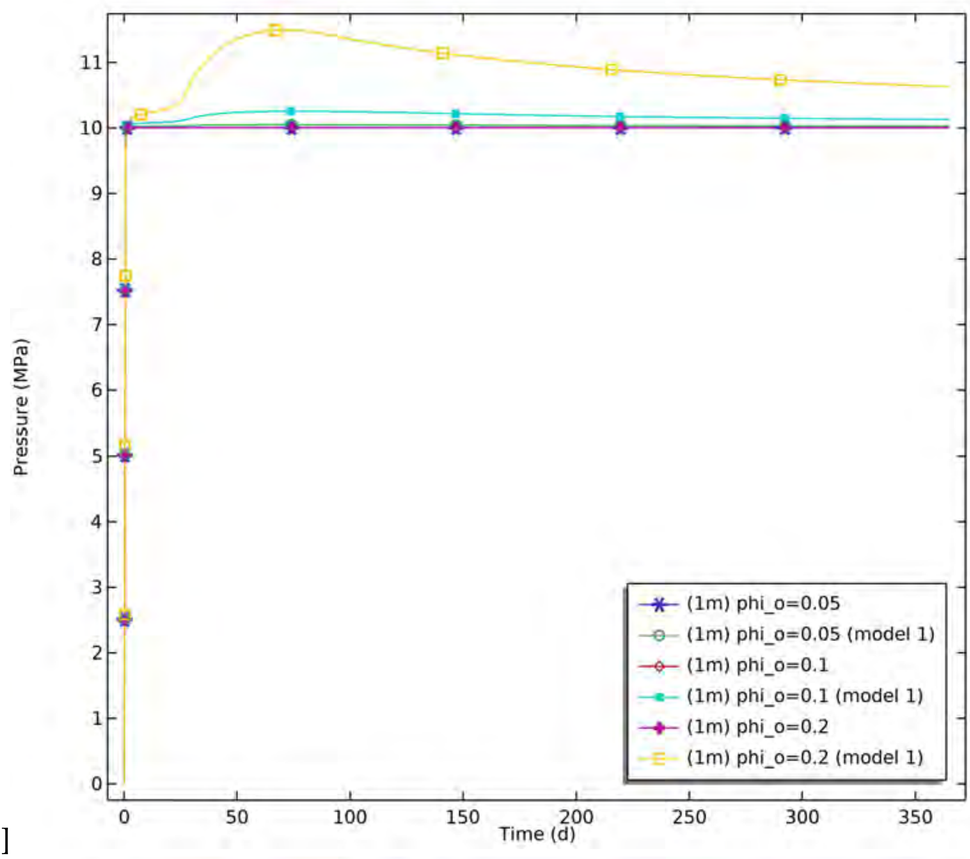
Pressure (MPa)
Time (d)
0
1
2
3
4
5
6
7
8
9
10
11
0
50
100
150
200
250
300
350
(1m) phi_o=0.05
(1m) phi_o=0.05 (model 1)
(1m) phi_o=0.1
(1m) phi_o=0.1 (model 1)
(1m) phi_o=0.2
(1m) phi_o=0.2 (model 1)

[a]

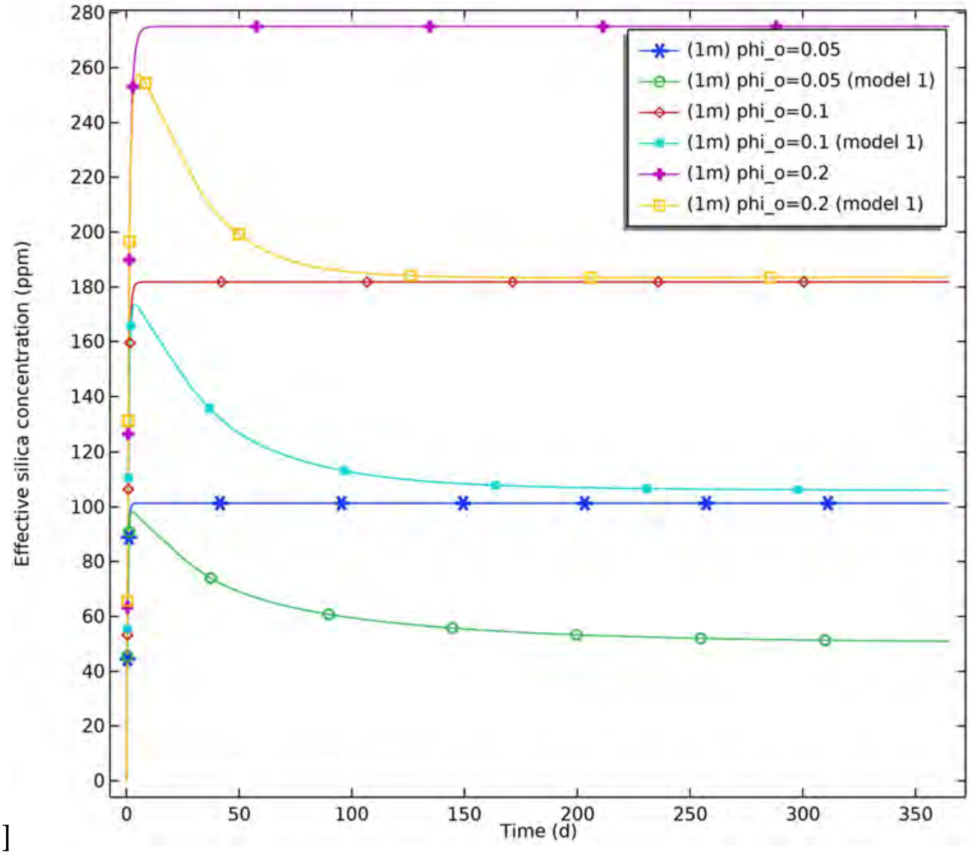
Effective silica concentration (ppm)
Time (d)
0
20
40
60
80
100
120
140
160
180
200
220
240
260
280
0
50
100
150
200
250
300
350
(1m) phi_o=0.05
(1m) phi_o=0.05 (model 1)
(1m) phi_o=0.1
(1m) phi_o=0.1 (model 1)
(1m) phi_o=0.2
(1m) phi_o=0.2 (model 1)

[b]

[c]

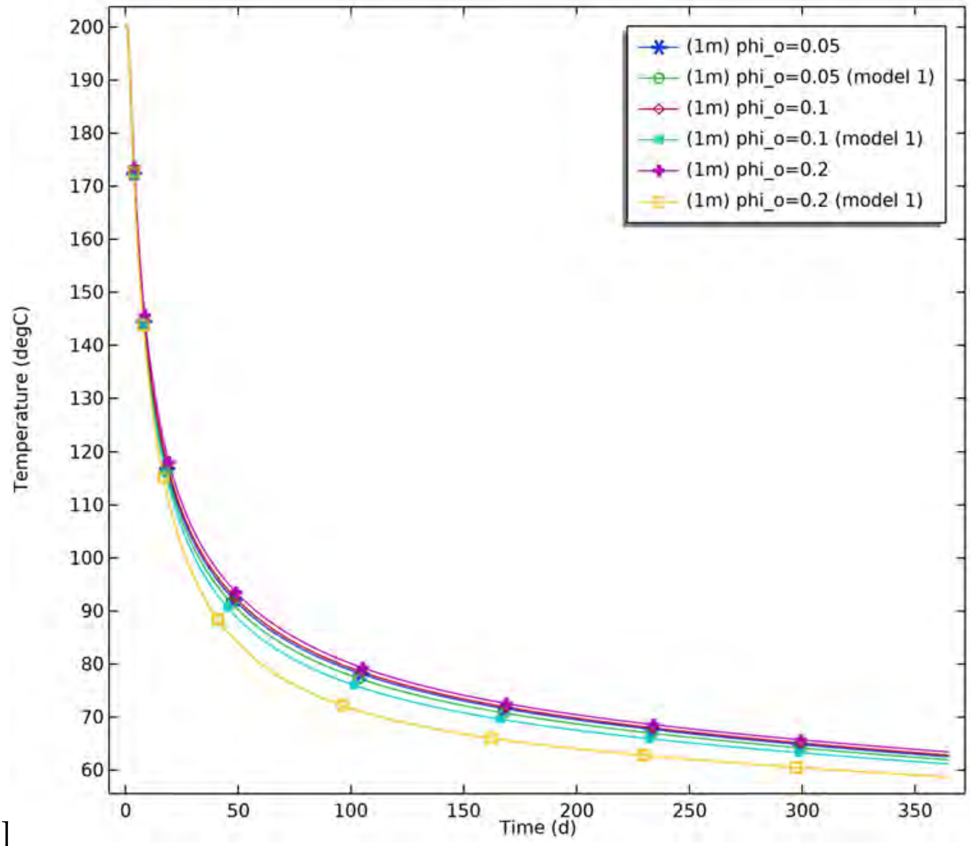

FIGURE 2.6: Comparison of [a] pressure [MPa], [b] effective silica concentration [ppm] and [c] temperature [°C] between constant and transient porosity (model 1) scenarios, each evaluated for two values of initial porosity 5%, 10% and 20%. The values occur at 1[m] from the source under 365 days of injection.

Although this change is slight, rocks in a critical state of stress could respond to such changes. Effective silica concentration goes to 0 at 6.2[m] for ϕ_o=0.2 at 4.2[m] for ϕ_o=0.1 and at 3[m] for ϕ_o=0.05 (Figure 2.6[b]). Consequently, the porosity does not vary beyond this distance. Finally, Figure 2.6[c] shows, although negligible, that the temperature calculated with transient porosity is slightly lower than the one calculated assuming a constant porosity. In Figure 2.6[c], we can distinguish two zones. The highest concentration occurs in the first zone, [0,2][m] and consequently, the highest change in porosity, highest change in thermal diffusivity and highest effect of enthalpy, thus negating the effects of overpressure. The largest difference in temperature lies in zone [2,10][m] because the dominant effect is the increasing overpressure (Figure 2.6[a]). Finally, the difference in temperature is the highest for ϕ_o=0.2 and is negligible for ϕ_o=0.05 because of the absence of significant overpressure (Figure 2.6[a]).

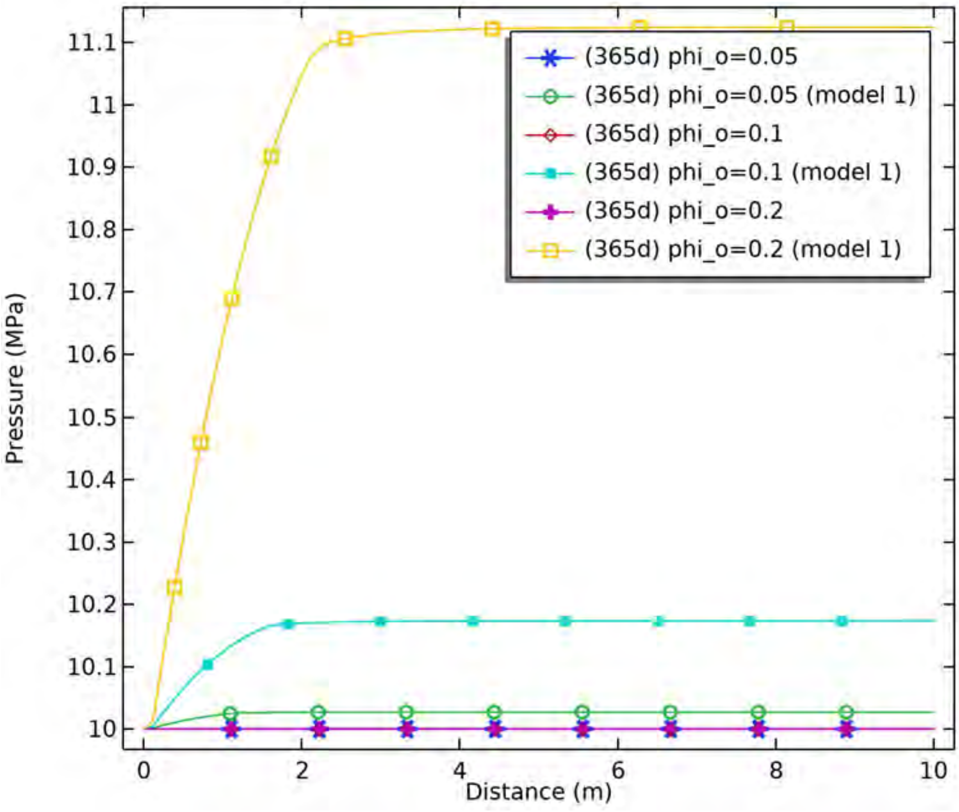
Pressure (MPa)
11.1
11
10.9
10.8
10.7
10.6
10.5
10.4
10.3
10.2
10.1
10
0
2
4
6
8
10
Distance (m)
(365d) phi_o=0.05
(365d) phi_o=0.05 (model 1)
(365d) phi_o=0.1
(365d) phi_o=0.1 (model 1)
(365d) phi_o=0.2
(365d) phi_o=0.2 (model 1)

[a]

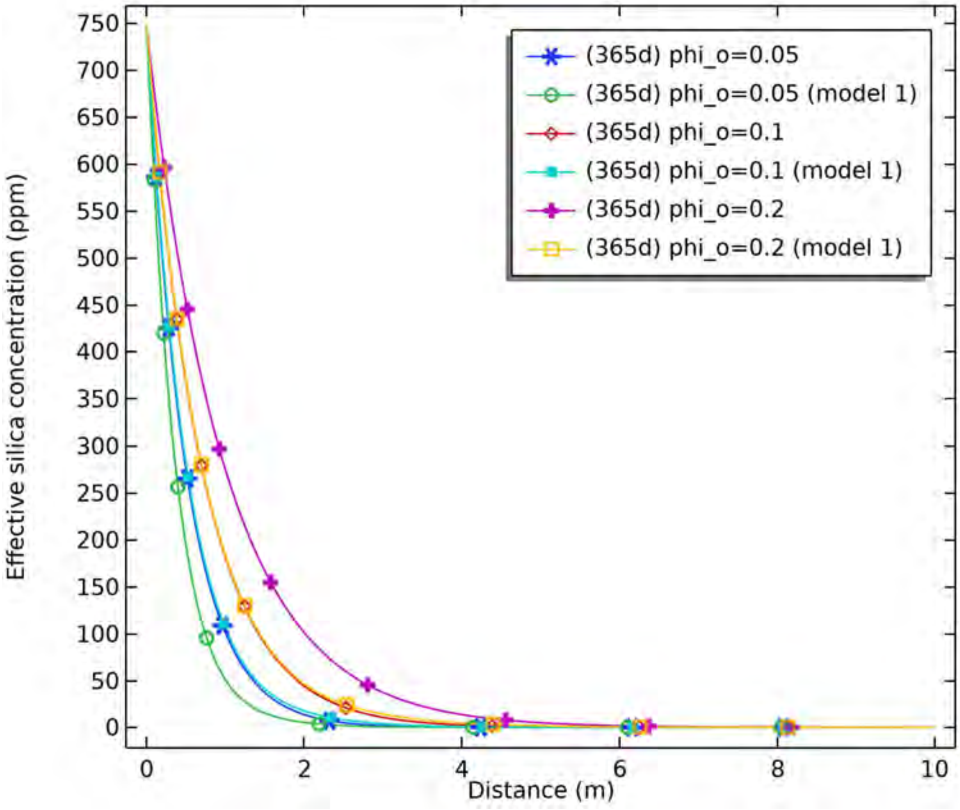
Effective silica concentration (ppm)
750
700
650
600
550
500
450
400
350
300
250
200
150
100
50
0
0
2
4
6
8
10
Distance (m)
(365d) phi_o=0.05
(365d) phi_o=0.05 (model 1)
(365d) phi_o=0.1
(365d) phi_o=0.1 (model 1)
(365d) phi_o=0.2
(365d) phi_o=0.2 (model 1)

[b]

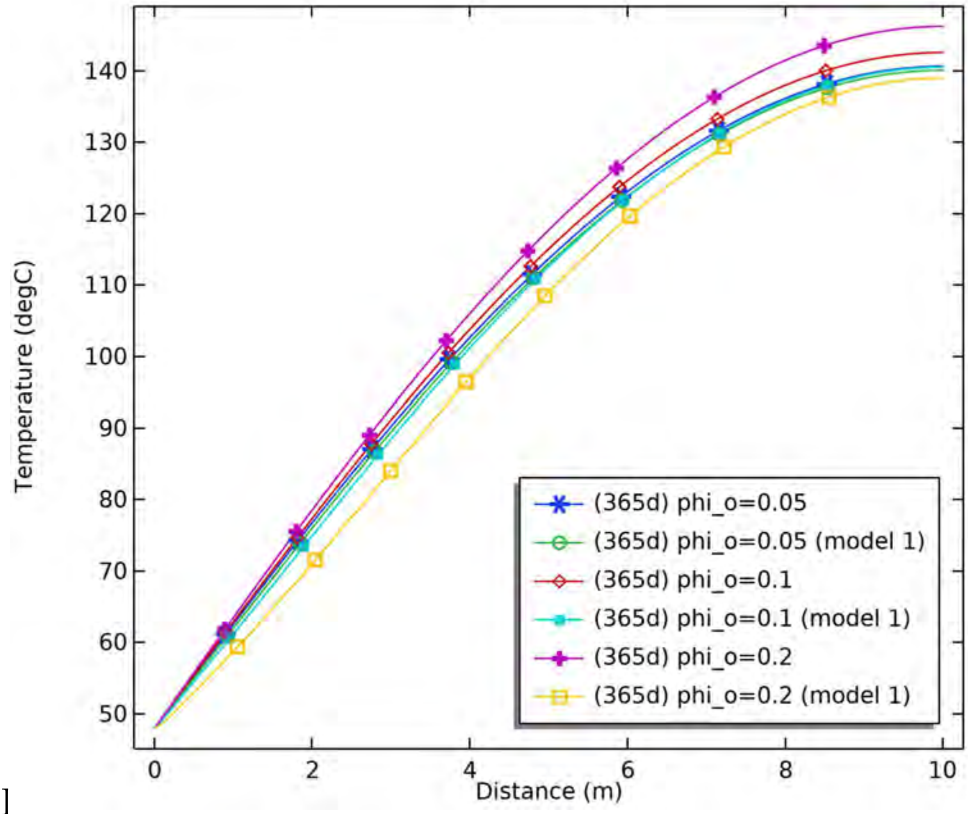

[c]

FIGURE 2.6: Comparison of [a] pressure [MPa], [b] effective silica concentration [ppm] and [c] temperature [°C] between two scenarios, one with constant porosity and one with transient porosity (model 1), and each evaluated for initial porosity 5%, 10% and 20%. Results are shown along a 10[m] distance and at t=365 days of simulation with the model setup portrayed in Figure 2.3.

2.9.2 1D THC simulation near a silica-rich cooling injection source: model 2

Similar to model 1, we compare pressure, concentration and temperature results between two scenarios, one with constant porosity and one with transient porosity, and each evaluated for initial porosity values of 5% and 10%.

We constrain porosity reduction for [0,3][m] because silica deposition is most pronounced in this region from the source. The overpressure is detectable (Figure 2.6[a]) at 1[m] from the source, where pore pressure reaches a maximum 18[MPa] for ϕ_o=0.1 after 60 days of injection, and 11.5[MPa] for ϕ_o=0.05 after 90 days of injection. Then, the overpressure steadily declines to reach 11.2[MPa] for ϕ_o=0.1 and 10.03[MPa] for ϕ_o=0.05 after 1 year of injection.

As explained in model 1, porosity decrease reflects less space to accommodate the deposited silica. Furthermore, the overpressure means fluid will flow from the reservoir to the matrix, hence transporting silica that ends up clogging the walls of the well. Figure 2.6[b] shows that the effective

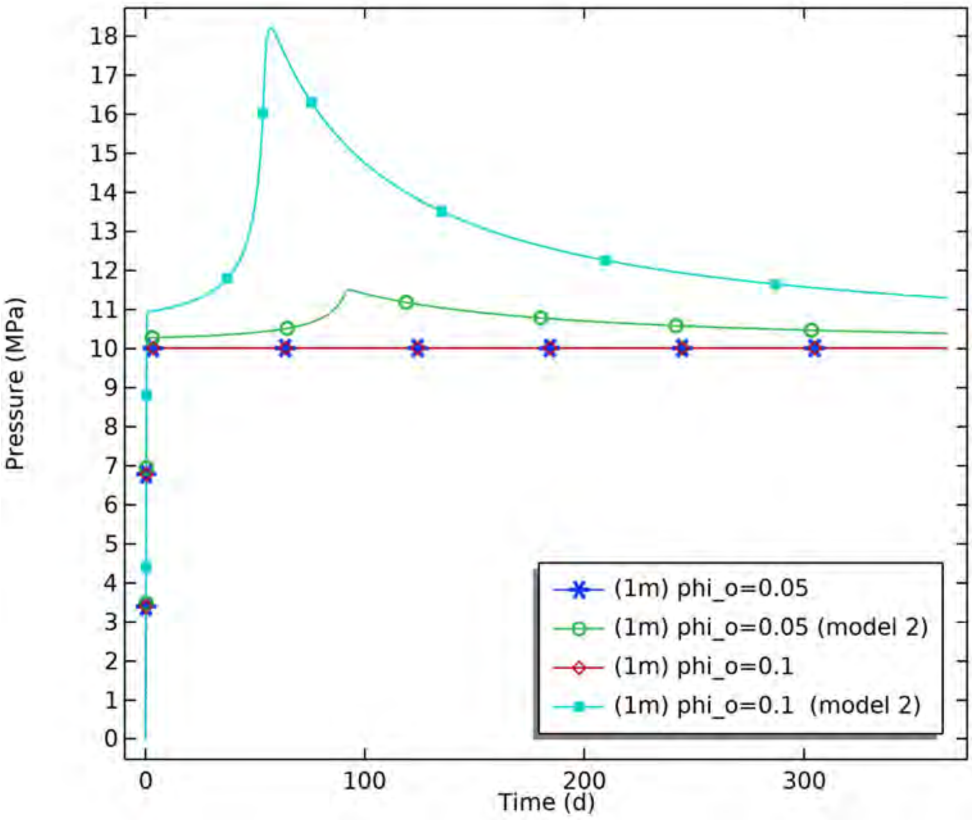
Pressure (MPa)
0
1
2
3
4
5
6
7
8
9
10
11
12
13
14
15
16
17
18
Time (d)
0
100
200
300
(1m) phi_o=0.05
(1m) phi_o=0.05 (model 2)
(1m) phi_o=0.1
(1m) phi_o=0.1 (model 2)

[a]

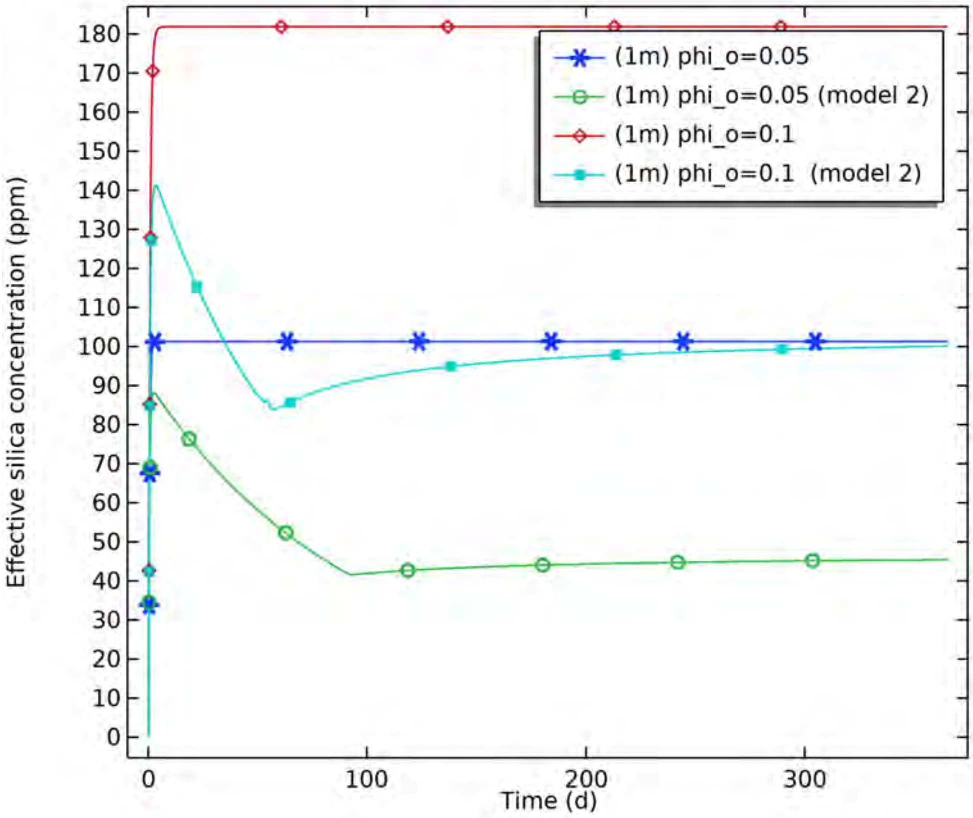
Effective silica concentration (ppm)
0
10
20
30
40
50
60
70
80
90
100
110
120
130
140
150
160
170
180
Time (d)
0
100
200
300
(1m) phi_o=0.05
(1m) phi_o=0.05 (model 2)
(1m) phi_o=0.1
(1m) phi_o=0.1 (model 2)

[b]

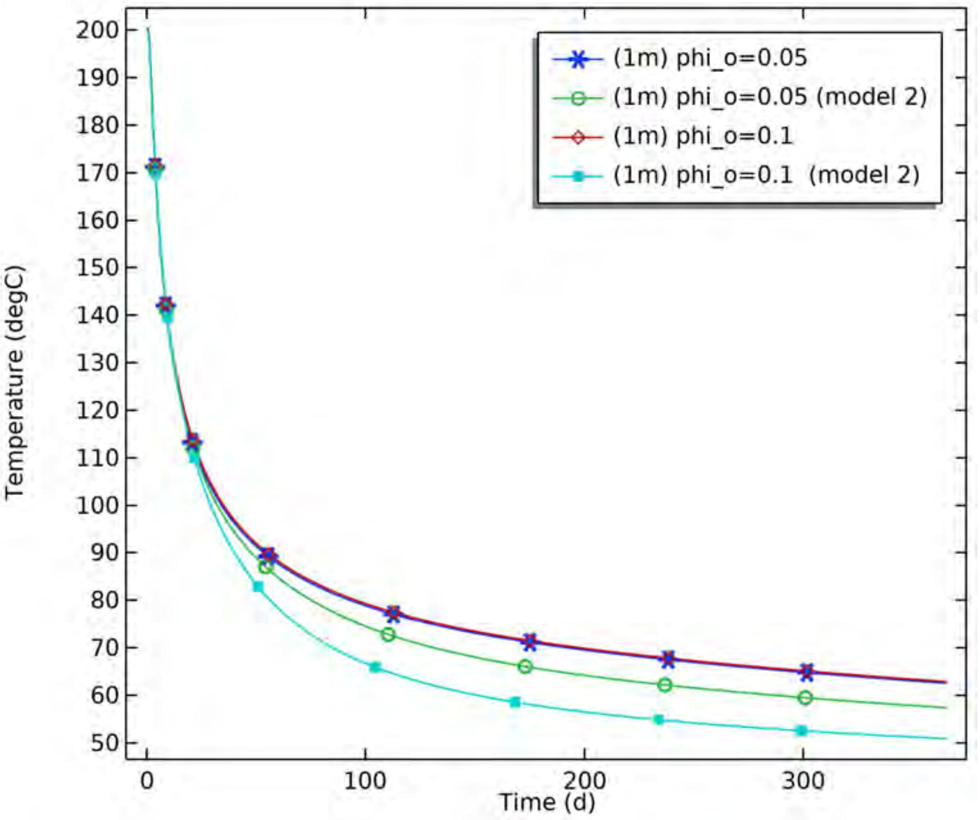

[c]

FIGURE 2.6: Comparison of [a] pressure [MPa], [b] effective silica concentration [ppm] and [c] temperature [°C] between constant and transient porosity (model 2) scenarios, each evaluated for two values of initial porosity 5% and 10%. The pressure values are reached at 1 [m] from the source over 365 days of injection.

silica concentration reaches a minimum after 70 days for ϕ_o=0.1 and after 90 days for ϕ_o=0.05, measured at 1[m] from the well. Then, this concentration starts to increase again because of the reverse Darcy flow: silica is transported from the reservoir to closer to the well. Nevertheless, the transient porosity reduces the concentration of deposited silica by 45% for ϕ_o=0.1 and by 55% for ϕ_o=0.05 after 1 year of injection.

In addition, the calculated temperature is lower for the case of transient porosity, which is more noticeable for ϕ_o=0.1 with a decrease of 21% after 1 year. This, however, on closer inspection near the boundary, Figure [c] shows a temperature decrease by almost 43% for ϕ_o=0.1 and 21% for ϕ_o=0.05 at the boundary x=10 [m].

The reason for this is the significant overpressure at x=10 [m] as shown in Figure 2.6[a]. The rate of overpressure development depends significantly on the rate of porosity reduction. In this case, the abrupt drop in porosity instigates this surge in pore pressure. Consequently, a reverse Darcy velocity develops (Figures 2.6[b-c]) in the system and fluid transports heat and silica from the reservoir to the boundary of the well, thus causing both temperature and concentration to decrease. A noticeable

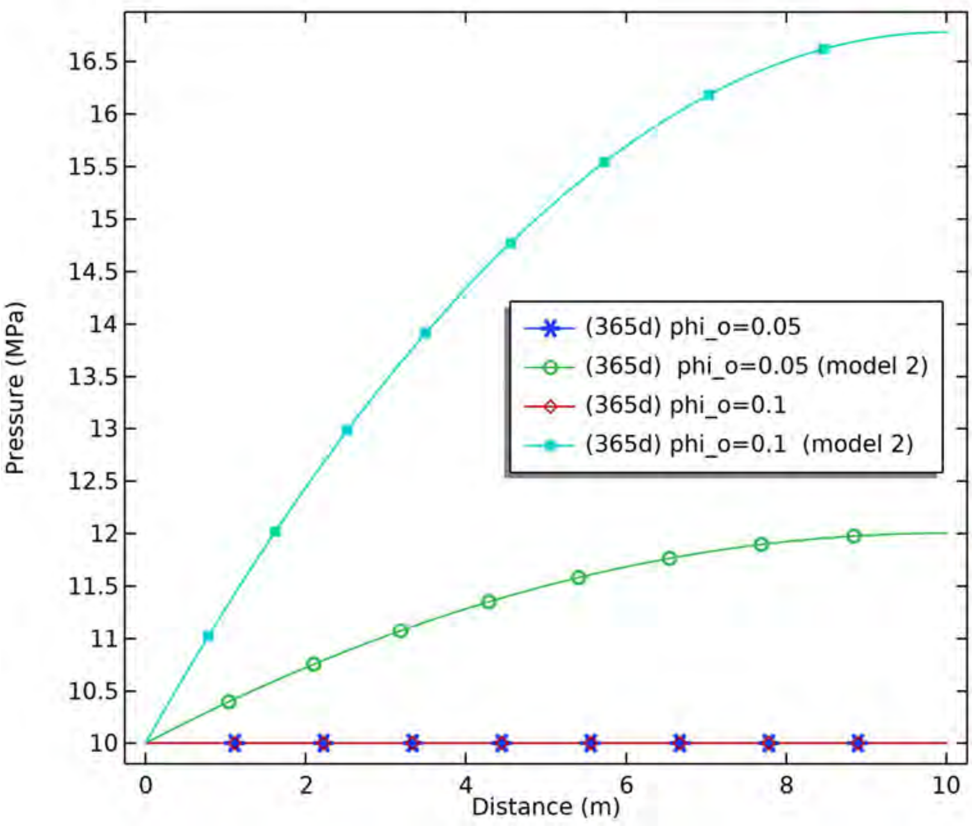

[a]

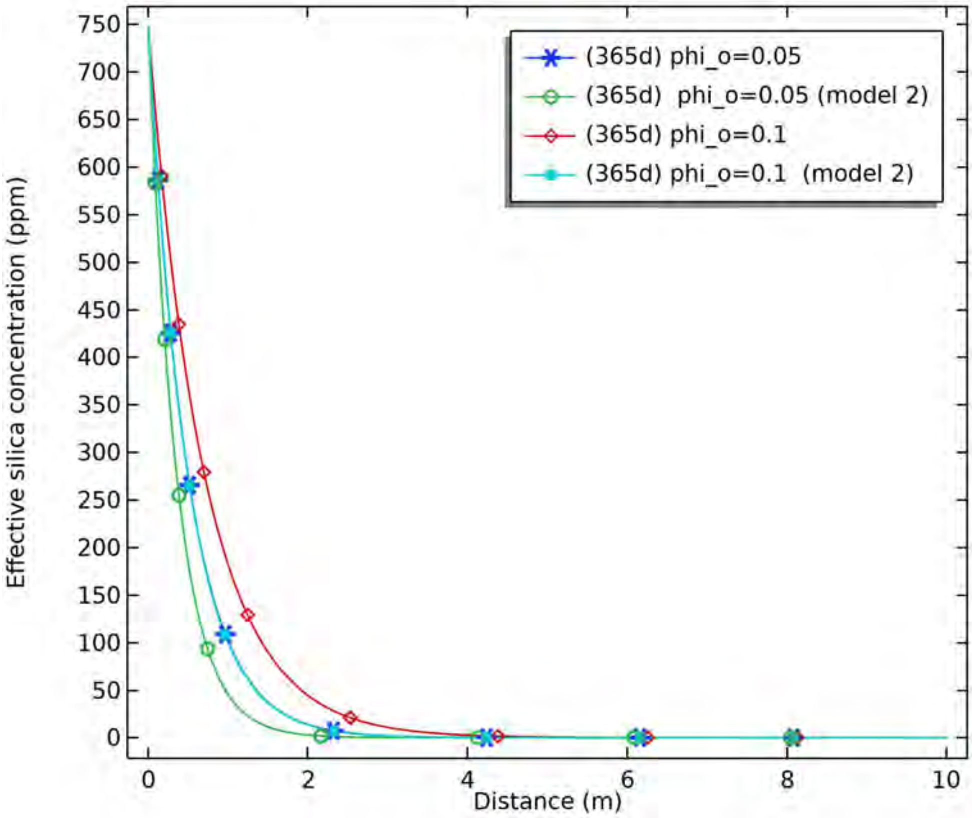

[b]

drop in temperature does not occur in the first 2[m] because silica deposits heavily in that zone, thus the effects of enthalpy and thermal diffusivity changes the effects of the smaller overpressure. Figure

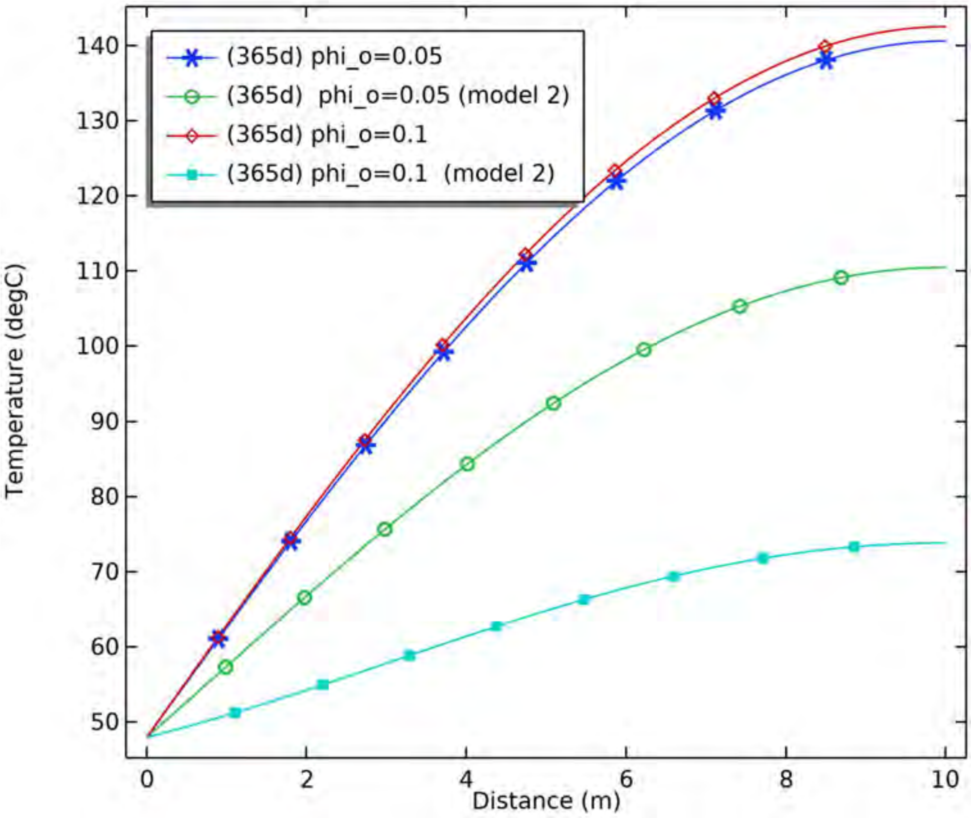

[c]

FIGURE 2.6: Comparison of [a] fluid pressure [MPa] [b] effective silica concentration [ppm] and [c] Temperature [C] between two scenarios, one with constant porosity and one with transient porosity (model 2), and each evaluated for initial porosity 5% and 10%. Results are shown along a 10[m] distance and at t=365 days of simulation with the model setup portrayed in Figure 2.3.

10b also shows that the effective silica concentration is lower for the case of ϕ_o=0.1 because of the combined effects of abrupt porosity reduction and overpressure. Therefore, one must account for the substantial overpressure due to rapid porosity reduction rate and the consequent accelerated cooling front when investigating effective stresses. Model 2 represents an end-member case, where pore pressure peaks to 17[MPa] (Figure 2.6[a]) at the location x=10[m] because of the rapid obstruction of porosity and permeability (Figure 2.5).

2.9.3 Implications of porosity reduction on the effective stresses

In this section, we apply the fully coupled THC model with transient porosity (via model 2) on a vertical injection well surrounded by an isotropic porous medium (Figure 2.7). We investigate the effects of porosity evolution due to quartz precipitation on the effective stresses and radial displacement in the vicinity of the injection well (Figure 2.7). Figures 2.8[a-b] show the radial fluid velocity and energy flux, respectively. Arrow direction confirms that part of the flow and heat transport develops from the reservoir to the well while another part flows towards the boundary.

The radial and tangential effective stresses in cylindrical coordinates with reference pressure of zero can be written as: (Zoback, 2010):

$$\begin{aligned}\sigma_{rr} = \frac{1}{2}\left(S_{Hmax} + S_{hmin}\right)\left(1 - \frac{R^2}{r^2}\right) + \frac{1}{2}\left(S_{Hmax} - S_{hmin}\right)\left(1 - 4\frac{R^2}{r^2} + 3\frac{R^4}{r^4}\right) \\ cos(2\theta) + \left(P_{inj}\frac{R^2}{r^2}\right) - \alpha P_p - \beta_s \Delta T\end{aligned} \tag{2.21}$$

$$\begin{aligned}\sigma_{\theta\theta} = \frac{1}{2}\left(S_{Hmax} + S_{hmin}\right)\left(1 + \frac{R^2}{r^2}\right) - \frac{1}{2}\left(S_{Hmax} - S_{hmin}\right)\left(1 + 3\frac{R^4}{r^4}\right) cos(2\theta) \\ - \left(P_{inj}\frac{R^2}{r^2}\right) - \alpha P_p - \beta_s \Delta T\end{aligned} \tag{2.22}$$

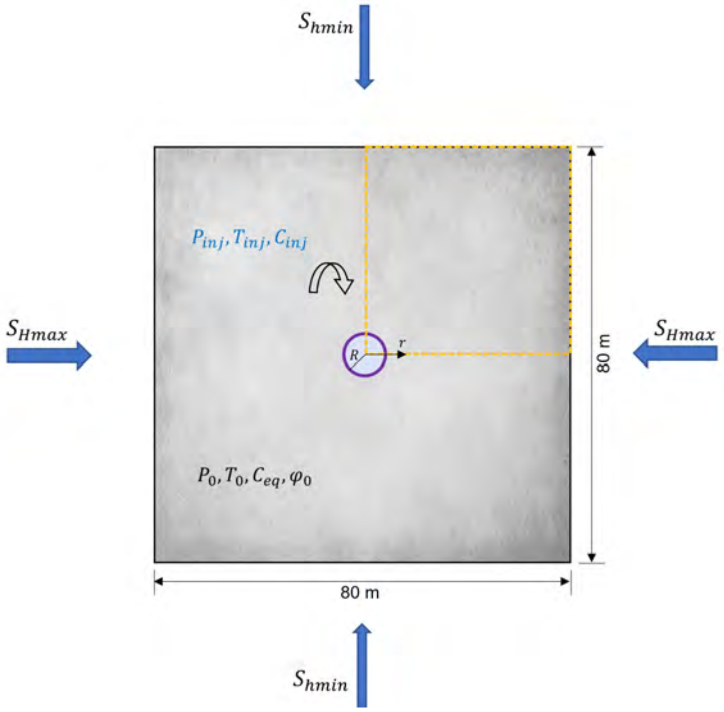

FIGURE 2.7: Top view (Figure 2.1) of the vertical injection well surrounded by isotropic porous medium in 2D. Because of the symmetry, we limit our study to the highlighted quadrant (yellow dashed box). Boundary at x= 40 [m] has a fix constrain of p=0 [MPa] and $T=T_0$[°C]. R is the radius, and r is the distance from the center of the well located at [0,0].

Where S_{Hmax} is the maximum horizontal stress [MPa], S_{hmin} is the minimum horizontal stress [MPa], R is the radius of the well [m], r is the radial distance from the center of well located at [0,0] [m], θ is the angle measured from the azimuth of S_{Hmax}, α is Biot's coefficient assumed 1 [1], Δp is the change in pore pressure [MPa], β_s is the thermal parameter that depends on the thermal expansion of the rock and its compressibility assumed $1.45e^5$ [Pa K^{-1}], and ΔT is the change in temperature

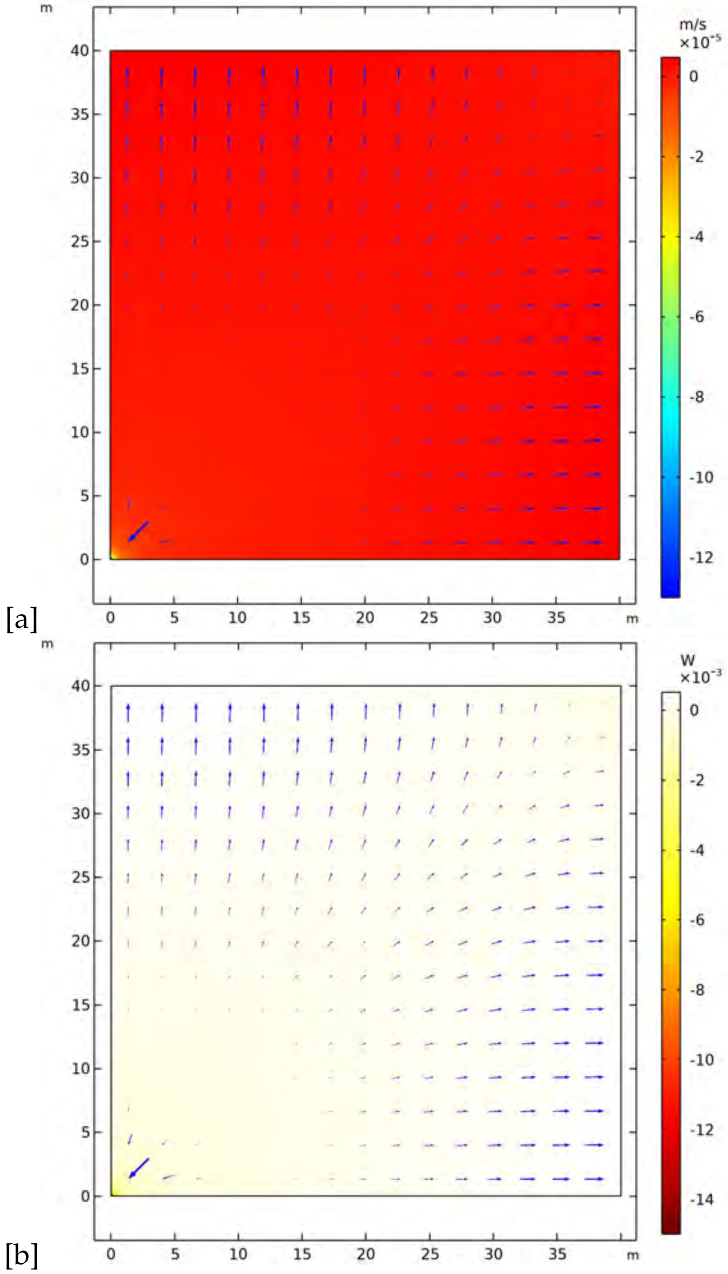

FIGURE 2.8: [a] Fluid velocity [b] Energy flux around the well with its center located at [0,0]. The arrows show the direction of the heat velocity and the energy flux and confirm that part of the fluid and heat are transported from the reservoir to the well and the other part flows towards the boundary.

[°C]. For simplification, we study a 1D geometry at angle θ =0 (horizontal line) in a hydrostatic state of stress (S_{Hmax}=S_{hmin}) assumed 30[MPa], and we compare scenarios of constant porosity and of transient porosity (model 2) with an initial porosity ϕ_o=0.1 and the injection pressure P_{inj} is given as 10 [MPa].

Figure 2.9 shows radial and tangential stresses (with initial porosity of ϕ_o=0.1) for three different scenarios subjected to 30 days of injection; 1) the elastic case that is the Kirsch solution, 2) an effective

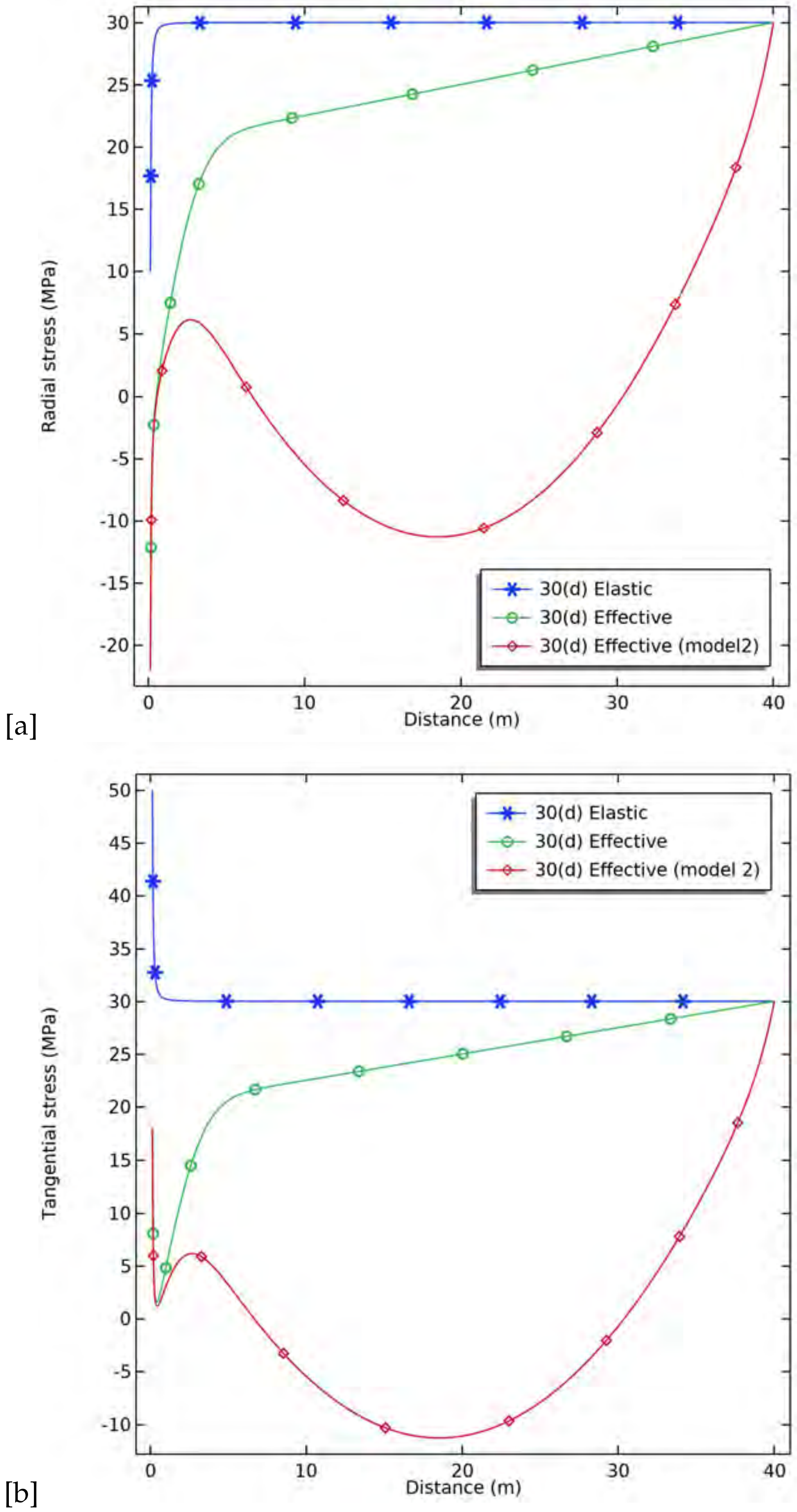

FIGURE 2.9: [a] Radial stress and [b] Tangential stress in the hydrostatic system (S_{Hmax}=S_{hmin}) assumed 30 [MPa] at the angle $\theta = 0$ after 30 days of injection. Each plot compares three scenarios: 1) the elastic case that is the Kirsch solution, 2) an effective stress case that assumes a constant porosity, and 3) an effective stress case that assumes the transient porosity reduction Model 2, with initial porosity ϕ_o=0.1.

stress case that assumes a constant porosity, and 3) an effective stress case that assumes the transient porosity reduction Model 2. Figure 2.9[a] show that the transient porosity decreases the stresses by almost 36[MPa] after 30 days of injection. In addition, the tensile strength of silicate rocks is on the order of [10-12][MPa], and Figure 2.9[b] shows that the tangential stresses approaches this value after 30 days of injection at 18[m] from the well. Therefore, an abrupt drop in porosity increases the likelihood of tensile failure. For both the radial and tangential stresses, the calculated stress goes to S_{Hmax}, where Δ p and Δ T are zero.

In this plane strain problem the poroelastic radial displacements u_r are (Jaeger, Cook, and Zimmerman, 2009, Zoback, 2010):

$$\frac{\partial}{\partial r}\left(\frac{1}{r}\frac{\partial(ru_r)}{\partial r}\right) = \frac{1-2\nu}{(1-\nu)2G}\left(\alpha\frac{\partial P_f}{\partial r} + \beta_s\frac{\partial T}{\partial r}\right) \tag{2.23}$$

Where u_r is the displacement [mm], ν is Poisson's ratio taken as 0.219[1] and G is the taken as 27500[MPa].

For the elastic hydrostatic in-situ stress case, Eq. 2.24 is rendered to zero. The displacement can be re-written, in the presence of mud weight P_{inj}, as follows (compression positive):

$$2Gu_r = \sigma\left((1-2\nu) + \frac{R^2}{r^2}\right)r - P_{inj}\frac{R^2}{r} \tag{2.24}$$

Figure 2.10 shows the radial displacement (with initial porosity of 0.1.) for three different scenarios subjected to 30 days of injection; 1) the elastic case that is the Kirsch solution, 2) an effective stress case that assumes a constant porosity, and 3) an effective stress case that assumes the transient porosity reduction Model 2. It is clear that a significant porosity reduction may generate a tensile displacement larger than the constant porosity scenario by as much as 10[mm].

This simplified study encourages further investigation of the effects of a sudden and significant drop in porosity due to silica precipitation on the mechanical response of the reservoir. Undoubtedly, porosity reduction must be considered for a more secure design and improved reservoir management.

2.10 Conclusions

Although this work is theoretical, it relies on well-documented models for porosity evolution and on the well-established governing equations for fluid, heat and reactive transport. Porosity reduction

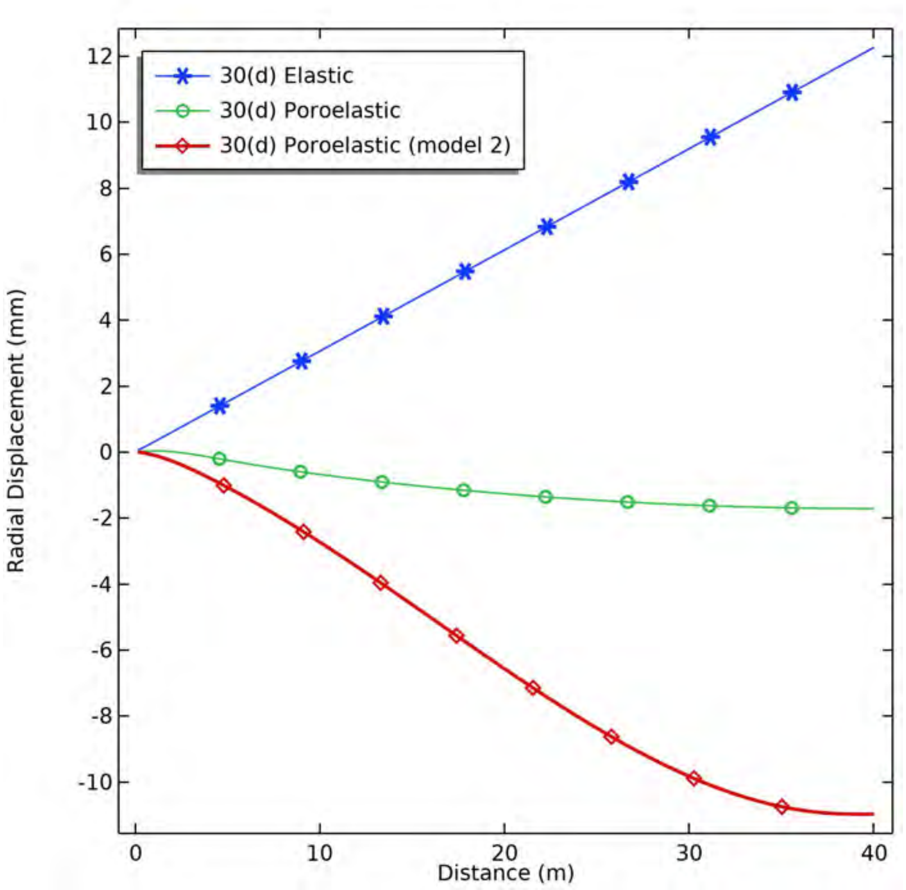

FIGURE 2.10: Comparison of radial displacement 30 days after injection between three scenarios: 1) the elastic case that is the Kirsch solution, 2) an effective stress case that assumes a constant porosity, and 3) an effective stress case that assumes the transient porosity reduction Model 2. Compression positive. Tensile displacement is almost 10[mm] larger when accounting for transient porosity.

introduces a source term to the pore pressure equation, which most models opt to neglect for the sake of simplification. Here, we calculate the fluid pressure, temperature and concentration components coupled with the transient porosity and the enthalpy using finite elements methods. Both porosity reduction models show a significant decrease in porosity but regardless of the model used to estimate the porosity reduction, the response of the system ultimately depends on the rate of porosity reduction. The faster the rate, the more abrupt is the effect on the system, as it cannot handle to sudden surge in pore pressure. In contrast, when the porosity reduction is slower, the system is continuously adapting to this steady increment in pore pressure and the effects are less compelling.

We ran two main numerical experiments, one for a moderate porosity reduction rate and one for a faster porosity reduction rate and results include: 1) the decrease in porosity is faster for higher initial porosity in the system, and 2) the pore pressure in the rock may exceed the pressure in the well/source, resulting in a reverse Darcy flow. Consequently, fluid transports temperature and silica from the reservoir to the source, thus accelerating the cooling front and clogging the wellbore walls. This may explain why some geothermal doublets suffer a decrease in injectivity and consequently underperform.

Furthermore, transient silica concentration is primarily governed by the porosity reduction rate. A comparison with a model that assumes a constant porosity shows that the system can accommodate less silica with time, thus the decrease in effective silica concentration. Since enthalpy is multiplicative with concentration, the effect of enthalpy is only present in the first meters from the well, because there lies the highest concentration of silica. Finally, we showed that the tensile failure is driven by two main mechanisms, namely the decrease in porosity and the observed reversed flow. The increase in pore pressure and thermal stresses results in a range of effective stresses that causes tensile failure and jeopardizes the integrity of the well.

In addition, the estimated dynamic porosity (and thus permeability) may be of interest to the geothermal industry because it may help quantify the thickness of clogging induced by heat extraction. Finally, we show that the effective stresses with silica deposition should be considered in reservoir management and productivity. The interesting results of the presented numerical experiments encourage more work in a laboratory setting to establish a relation between porosity reduction rate, and fluid and heat behavior. We will expand on this study in future work to include other mineral depositions such as calcite.

Chapter 3

Incorporating porosity reduction as a source term in the coupled thermo-hydro-chemical analysis: Application to silica deposition in fractured geothermal reservoirs

3.1 Abstract

Porosity reduction due to silica deposition produces elevated pore pressures in fractured geothermal systems, resulting in a reversed Darcy flow that disturbs the pressure and temperature front and ultimately, the effective stresses. A decrease in effective stress renders fractures unstable and jeopardizes the integrity of the enhanced geothermal system. In this paper, we present a numerical model that couples the thermo-hydro-chemical processes in a fractured geothermal reservoir subjected to porosity reduction and fracture aperture evolution due to silica deposition. The 2D model includes the pore pressure in excess of hydrostatic as a source term and accounts for non-isothermal fluid flow, advection, and considers the linear kinetics of quartz dissolution/ precipitation, all of which is modeled using COMSOL Multiphysics. The model highlights the important role of porosity reduction on matrix/fracture permeability evolution and explains why some geothermal reservoirs have underpreforming doublets and/or restricted flow. Results show that the decrease in porosity induces a pore pressure in excess of hydrostatic, forcing Darcy flow to reverse direction and causing supplementary thermoelastic effects on fracture aperture. A larger porosity reduction rate results in larger

thermoelastic effects and thus larger fracture apertures. A lower initial fracture aperture increases the excess pore pressure and contributes to larger thermoelastic effects. Finally, the conjugation of the overpressure and the faster cooling front induces fracture instability.

3.2 Introduction

Geothermal energy production is a promising renewable energy source that consists of injecting a fluid into the reservoir and allowing it to circulate through natural or artificial fractures, leading to complex rock-fluid interaction. That is, an exchange of heat between the fluid and the rock alters the state of stress in the reservoir and eventually controls the evolution of fracture apertures. However, a large percentage of geothermal reservoir rocks are composed of granite and contain crystalline rocks, in particular quartz, thus increasing the complexity of the problem. Quartz can exhibit different behaviors depending on pressure and temperature conditions, making it difficult to predict the response of the hot rock. Quartz tends to precipitate as amorphous silica near the injection well, where pressure is high and temperature is low, and tends to dissolve at the extraction well, where pressure is lower and temperature is higher. However, inside the fracture, silica deposition is controlled by quartz solubility (Rawal and Ghassemi, 2014) and not amorphous silica. Silica deposition in geothermal reservoirs leads to clogging of the pores and the fractures, resulting over time in restricted flow and under-performing doublets. In this paper, we expand the study to simulate (using the COMSOL multiphysics platform) the pressure, temperature and concentration in a fractured geothermal reservoir under different settings, while accounting for the effects of porosity reduction and fracture aperture evolution. The abundant research in the topic contributes to our present understanding of coupled heat and fluid behavior and their effects on the evolution of the fracture width, and the long term productivity of the system. To cite a few, we begin with (Ghassemi, Nygren, and Cheng, 2008) who studied fracture aperture evolution due to cold-water injection in enhanced geothermal reservoirs using numerical models, and derived analytical solutions for special cases of injection rate and leak-off. Their results show that poroelasticity causes the fracture width to decrease, specifically at the injection point (where pressure is high) and becomes minimal near the extraction point, and that rock stiffness and fluid diffusivity control the transient behavior of fracture evolution. Results also display the dominant effects of thermoelasticity in the presence of temperature gradient, causing fracture aperture to increase and consequently pressure to drop in the reservoir. Furthermore, Abousleiman, Hoang, and Liu (2014) studied a one-dimensional porothermoelastic problem based on the consolidation theory and derived analytical solutions for fracture aperture evolution with an application to shale reservoirs, concluding that one can obtain a 70% larger fracture width in the presence of a significant thermal gradient at the fracture-rock interface. This would not be the case in the absence of a thermal gradient, where the fracture starts to close shortly after pumping. In a recent publication, Gisler (2021) studied the effects of spatial variability of rock/fluid properties and performed an uncertainty quantification for a hydraulic fracture geometry in the presence of temperature gradient using Monte-Carlo simulations. The properties are ranked by order of influence as such: Young's Modulus, thermal expansion coefficient of the rock, thermal conductivity, and mobility ratio (k/μ). Results also reveal the transient nature of the sensitivity ranking, clearly showing that fracture width is initially controlled by the elastic Young's modulus, and as fluid pressure and temperature propagate inside the formation, fracture width depends predominantly on the thermal expansion coefficient of the rock. On an experimental level, tracer tests were conducted by Kittilä et al. (2020) to study the behavior of fracture width under different temperatures of injected fluid by measuring the loss of fluid at the outlet. Experimental results prove a loss of fluid when injecting hotter fluids because the rock expands, thus decreasing the fracture width. Fracture width evolution is also studied by Lima et al. (2019), who model the thermally induced fracture aperture evolution with application to natural fractures in granite rocks. Furthermore, Jansen and Miller (2017) studied the role of thermal stresses on fracture aperture and shear failure and performed a simplified sensitivity analysis to understand the influence of initial fracture/matrix permeability and fracture orientation on thermal stress, and failure potential. Their results encourage introducing the transient thermoelastic stress in the long-term fluid injection models. From a computational standpoint, Galvan and Miller (2013) shows the potential of GPU powered models to better simulate coupled thermo-hydro-mechanical processes and improve calculation times. Laboratory tests performed by Yanaze et al. (2019) measure fluid flow rate from columns with circulating raw brine from the Geothermal power plant at Sumikawa, Japan. Their results show impressive decreases of fluid flow rates by 25% after 10 days of injection as a result of geochemical clogging of the pores due to deposited silica (aluminum and amorphous scales). They propose PH reduction of the brine to reduce the extent of permeability reduction. The unfortunate fact that silica deposition is a production problem has led to the subsequent research in the area, to cite a few (Steefel and Lichtner, 1998; Ghassemi and Kumar, 2007; Kumar and Ghassemi, 2005; Robinson and Pendergrass, 1989; Steefel, DePaolo, and Lichtner, 2005; Pandey and Chaudhuri, 2017; Pandey et al., 2014; Pandey et al., 2015; Rawal and Ghassemi, 2014). The system is therefore subjected to coupled thermo-hydro-chemical-mechanical processes, making it more difficult to accurately model or predict the performance of the geothermal reservoir. Fracture width and porosity reduction can dramatically decrease the injectivity of the well and in Ghassemi and Kumar (2007), the authors study the changes in fluid pressure and in fracture aperture due to the combined thermoelastic effects and silica deposition using linear reaction kinetics. Their results show that for narrower fracture width, the increase in aperture and drop in pressure at the inlet are mostly due to thermoelastic effects, while the increase in width at the production point is primarily due to silica dissolution. However, for wider initial fracture width, the effects of silica deposition are minimal and thermoelastic effects prevail causing an increase in fracture width. A numerical model developed by Kumar and Ghassemi (2005) studies the non-isothermal quartz dissolution/precipitation in a fractured geothermal reservoir, which includes solute dispersion and thermal conduction-dispersion. They perform a sensitivity analysis proving the important roles played by reservoir thermal conductivity, reservoir porosity, reservoir effective diffusion coefficient, water velocity in the fracture, and the initial fracture aperture. In Rawal and Ghassemi (2014), the authors present a 3D coupled poro-thermo-chemo-mechanical model to study the effects of injection and production on fracture permeability. The proposed numerical model uses the Boundary Element Method (BEM) to simulate the mechanical response and the finite element method (FEM) to study fluid, heat and solute transport in the fractured reservoir. Their numerical example studies the response of the system subjected to silica deposition and dissolution and finds that when the injected fluid is undersaturated with respect to silica, dissolution occurs and spreads within the fracture. Further, results show that thermoelastic effects dominate the poroelastic ones at larger times and highlight the importance of fracture stiffness heterogeneity on flow path and silica reactivity. The poro-thermoelastic effects, which cause the fracture width to increase, diminish in the presence of higher joint normal stiffness and higher aperture expansion due to silica dissolution. A numerical thermo-hydro-chemical model is proposed by Pandey et al. (2015), in which they present simulation for silicic reservoirs for long term injectivity (20 years). Their results show the importance of the temperature dependent reaction rate and how supersaturated fluids cause precipitation to occur in bands and therefore confining flow into smaller areas. In contrast, silica dissolution causes fracture permeability to increase far from the injection well, thus creating longer flow paths and insuring longer and better geothermal productivity. A 3D thermo-hydrodynamic model with reactive flow that accounts for porosity and permeability evolution, powered by GPU clusters, is introduced by Sohrabi, Omlin, and Miller (2019). The suggested computational method highly improves the resolution of modeled coupled transient heat, fluid and reactive transport processes, in a 3D computational domain.

Although there exists an extensive literature in the topic of coupled thermo-hydro-chemical processes (THC) within complex settings, most neglect the porosity reduction source term in the pore pressure diffusion equation, which in our view must be considered (Walder and Nur, 1984). A recent publication by Gisler and Miller (2021) shows the importance of the porosity reduction source term and its consequences on the effective radial and tangential stresses around a well. When the effective stress exceeds the minimum horizontal stress, cracks appear, thus jeopardising the integrity of both the well and the reservoir. In this paper, we run a suite of numerical experiments and perform a sensitivity analysis to determine how the solution behaves for different porosity reduction rates and initial fracture apertures. We also conclude with simplified study of failure potential using the Mohr-Coulomb criterion. For brevity, we refer to our code as SPARROW, which is an acronym for, **S**imulator for **P**orosity reduction and fracture **A**perture evolution in a geothermal **R**eservoir with **R**eactive fl**OW**. Our model is based on well- established governing equations and well documented studies of the effects of porosity reduction due to mineral precipitation, notably silica (as quartz). This proposed model can be adapted to any mineral(s) while considering its kinetics under different pressure and temperature conditions.

Results reveal the important influence of the porosity reduction rate, and the subsequent overpressure, on the thermoelastic fracture aperture evolution and the stability of the matrix/fracture system in a geothermal reservoir.

3.3 Materials and methods

3.3.1 Conceptual model

We study the influence of porosity reduction on the behavior and stability of a fractured geothermal system. Figure 3.1 illustrates a simplified fractured geothermal reservoir model with an injection well and a main fracture surrounded (at the top and bottom) by low-permeability rock layers. The injection pressure, temperature and concentration (of silica) are assumed constant and the rock matrix is subjected to porosity reduction due to mineral precipitation, whereas fracture aperture evolution is governed by the combined effects of temperature loss and silica deposition.

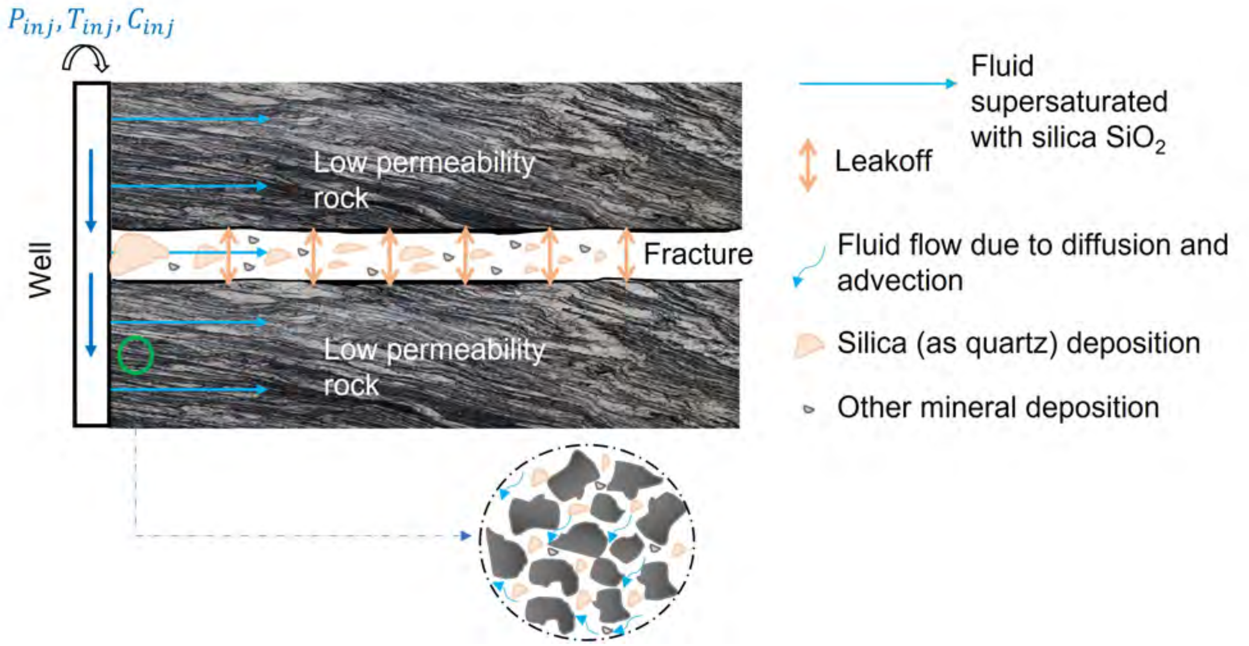

FIGURE 3.1: Simplified representation of silica deposition (as quartz) in a well-matrix-fracture geothermal system. P_{inj}, T_{inj}, and C_{inj} are the injection pressure, temperature and concentration, respectively. Leakoff and advection inside the system are considered in addition to porosity reduction. The fracture is surrounded (top and bottom) by low permeability rock layers. Zooming into the matrix shows our simplified assumption of precipitation occurring inside the matrix. Other minerals precipitate in geothermal systems, such as Calcite and Illite but are not covered in this paper.

3.3.2 Kinetics of silica deposition

Enhanced geothermal reservoirs typically target granite bedrock rich in quartz, and the reversible silica precipitation-dissolution reaction is:

$$H4SiO4_{(aq)} <=> SiO2_{(s)} + 2H2O \tag{3.1}$$

Although amorphous silica precipitates near the injection well, silica deposition inside the fracture is controlled by quartz solubility (Rawal and Ghassemi, 2014). Therefore, more porosity and fracture aperture reduction is to be expected because quartz solubility is extremely low (6-14[mg/L]), in comparison to that of amorphous silica (100-140[mg/L]) (Yariv and Cross, 1979; Rawal and Ghassemi, 2014) at 20°C. Furthermore, the low solubility of silica (as quartz) justifies the assumption that solubility is independent from the pressure in the system. Equilibrium concentration represents the temperature-dependent solubility of quartz in the pore fluid, and is given by (Rimstidt and Barnes, 1980); (Robinson and Pendergrass, 1989):

$$C_{eq} = 6 \times 10^4 \times 10^{\left(1.881 - 2.028 \times 10^{-3} T - 1560/T\right)} \tag{3.2}$$

where, C$_{eq}$ is the equilibrium silica concentration [ppm] and T is the initial temperature in the matrix [K].

3.3.3 Governing equations

Flow in the matrix

Assuming a single-phase fluid, mass conservation in a porous media is:

$$\phi_m \beta \frac{\partial p_m}{\partial t} = \frac{k_m}{\mu} \nabla^2 p_m + \Psi \tag{3.3}$$

Where p_m is the excess pore pressure in the matrix [Pa], k_m is the matrix permeability [m^2], μ is fluid viscosity [Pa s], ϕ_m is the porosity of the matrix [1], β is the bulk compressibility modulus [Pa^{-1}] and the subscript m is for matrix. Ψ is the source term given by (Walder and Nur, 1984):

$$\Psi = -\frac{\partial \phi_m}{\partial t} \tag{3.4}$$

Where Ψ is the porosity reduction factor [s^{-1}], assumed positive when porosity is decreasing. Darcy velocity (u) in the matrix, neglecting the gravity term, is:

$$\mathbf{u} = -\frac{k_m}{\phi_m \mu} \nabla p_m \tag{3.5}$$

Flow in the fracture

The fracture is considered as a more permeable zone within the low permeability matrix with a constant local porosity of one. The rate of fracture porosity reduction due to silica deposition is insignificant in comparison to that of the low permeability matrix, and is therefore neglected in the pore pressure diffusion calculation via (Eq.3.6). Only fracture aperture is assume to evolve in the system due to the combined effects of silica deposition and thermal gradient. Therefore, pressure in the fracture can be calculated using Eq.(3.2) with a null source term:

$$\beta \frac{\partial p_f}{\partial t} = \frac{k_f}{\mu} \nabla^2 p_f \tag{3.6}$$

Where p_f is the excess pore pressure in the fracture [Pa], μ is fluid viscosity [Pa s] and β is the bulk compressibility modulus [Pa^{-1}]. k_f is the fracture permeability [m^2], formulated as:

$$k_f = b^2/12 \tag{3.7}$$

where b is the fracture width [m].

Solute transport in the matrix

Advection-diffusion of the solute mass is given by (Steefel, DePaolo, and Lichtner, 2005):

$$\frac{\partial \left(\phi_m C_j^m\right)}{\partial t} = \nabla . \left(\phi_m D_m \nabla C_j^m\right) - \nabla . \left(\phi_m u C_j^m\right) - \sum_{s=1}^{N_s} \nu_{js} r_s \tag{3.8}$$

Where ϕ_m is matrix porosity [1], D_m is the effective solute diffusion coefficient in the rock matrix [m^2 s^{-1}], **u** is Darcy velocity vector [m s^{-1}], C_j^m is the concentration of chemical specie j in the matrix m [ppm], ν_{js} is a stoichiometric reaction coefficient [1], and r_s is the reaction rate of mineral s [kg m^{-3} s^{-1}]. While $\Psi \neq 0$ and assuming linear reaction kinetics, (Eq. 6) is rewritten as (Steefel and Lichtner, 1998):

$$\frac{\partial \left(\phi_m C_m^{'}\right)}{\partial t} = \nabla \cdot \left(\phi_m D_m \nabla C_m^{'}\right) - \nabla \cdot \left(\phi_m u C_m^{'}\right) - K_m C_m^{'} \tag{3.9}$$

Where K_m is the silica reaction rate [s^{-1}], and $C_m^{'}$ is the effective concentration of the chemical species in the matrix [ppm] and is given by:

$$C_m^{'} = C_m - C_m^{eq} \tag{3.10}$$

Where C_m^{eq} is the equilibrium concentration [ppm] in the matrix (calculated via Eq.2).

Solute transport in the fracture

Assuming linear reaction kinetics and a unit porosity in the fracture, the transport equation for the fracture is given by (Steefel and Lichtner, 1998):

$$\frac{\partial C_f^{'}}{\partial t} = -\nu \frac{\partial C_f^{'}}{\partial x} - k_f C_f^{'} + \frac{\phi_m D_m}{\delta} \frac{\partial C_m^{'}}{\partial y}|_{y=\delta} \tag{3.11}$$

Where $C_f^{'}$ is the effective silica concentration in the fracture [ppm], ν is the fluid velocity in the fracture [m s^{-1}] given by:

$$\nu = -\frac{b^2}{12\mu} \nabla p_f \tag{3.12}$$

k_f is the reaction rate constant [s^{-1}] in the fracture considered the same as (Steefel and Lichtner, 1998), and δ is the half-fracture width [m].

Heat in the matrix

Assuming low enthalpy as shown in (Gisler and Miller, 2021), the complete form of conservation of energy is given by (Steefel, DePaolo, and Lichtner, 2005):

$$\left[(1-\phi_m){C_p}^m \rho_m + \phi_m {C_p}^w \rho_w\right] \frac{\partial T}{\partial t} = \nabla . \left(\lambda_m \nabla T\right) - \nabla . \left(\rho_w C_p^w \phi_m u T\right) \tag{3.13}$$

Where λ_m is the thermal conductivity [W m^{-1} K^{-1}], C_p is the specific heat [J kg^{-1} K^{-1}], ρ is the density [kg m^{-3}] and subscripts m and w are for the matrix and fluid respectively.

Heat in the fracture

Heat transport in the fracture is given by (Kumar and Ghassemi, 2005):

$$\frac{\partial T_f}{\partial t} = -\nu \frac{\partial T_f}{\partial x} + (D_f + D_T) \frac{\partial^2 T_f}{\partial x^2} + \frac{1}{{C_p}^w \rho_w \delta} \left(\lambda_m \frac{\partial T_m}{\partial y}\right)|_{y=\delta} \tag{3.14}$$

Where T_f and T_m are the temperatures in the fracture and matrix, respectively, δ is the half-fracture width [m]. D_f is the thermal conduction coefficient of the fluid in the fracture given as $\lambda_w / (\rho_w c_w)$ [m^2 s^{-1}], D_T is the longitudinal thermal dispersion coefficient in the fracture given by V_0 β_T [m^2 s^{-1}], where β_T is the thermal dispersivity [m] (De Marsily, 1986), λ_m and λ_w are the thermal conductivity of the rock matrix and the fluid in the fracture, respectively [W m^{-1} K^{-1}].

Porosity reduction and permeability evolution in the matrix

We assume a dual-porosity, dual-permeability system, composed of the matrix and the fracture. The porosity variation in the matrix system is proportional to the mass of precipitated silica (as quartz). We assume that the minimum rate of porosity reduction in the medium is the one suggested by (Steefel, DePaolo, and Lichtner, 2005):

$$\frac{\partial \phi_m}{\partial t} = V_s R_s \tag{3.15}$$

Where V_s is the molar volume of SiO_2 taken as 28.10^{-6} [m^3 mol^{-1}] and R_s is the volume-normalized mineral reaction rate [mol m^{-3} s^{-1}] given by ((Scott and Driesner, 2018):

$$R_s = \phi . \frac{\Delta m_{rock}^{SiO_2}}{\Delta t} . \frac{10^3}{M_{quartz}} \tag{3.16}$$

Where M_{quartz} is the molar mass of SiO_2 (0.06008 [kg mol^{-1}]). Note that we perform a sensitivity analysis using three different values of porosity reduction, where the minimum is the one calculated via Equation 3.15 and the maximum porosity reduction rate is the based on the experimental results obtained by (Yanaze et al., 2019). The purpose of this paper is not to prove the reliability of the porosity reduction equations, rather to visualize the influence of porosity reduction rate on the pressure, temperature and concentration variables in a fractured geothermal reservoirs. The permeability variation depends on the precipitation-induced porosity (Civan, 2001), and empirically can be expressed as (Weir and White, 1996) and (Scott and Driesner, 2018):

$$k = k_0 \left\{ 1 - \left[1 - \left(\frac{\phi - \phi_c}{\phi_0 - \phi_c} \right)^{1.58} \right] \right\}^{0.46} \tag{3.17}$$

Where ϕ_c is the critical porosity defined as half of the initial porosity, ϕ_0 is the initial porosity and k_0 is the initial permeability [m^2]. The stability of the solution requires that the transient porosity does not go lower than the critical porosity.

Fracture aperture evolution

We consider the evolution of fracture width due to the combined effects of thermoelasticity and deposition of silica (as quartz). The evolution of fracture width due to thermoelastic effects is given by (Ghassemi and Kumar, 2007), assuming one-directional thermal stress and in the absence of shear or horizontal stress as:

$$\frac{\partial \delta}{\partial t}|thermoelastic = \frac{(1+\nu)}{(1-\nu)}\frac{\alpha_T \lambda_m}{\rho_m C_m}\delta T \delta y|_{y=\delta} \tag{3.18}$$

The evolution of fracture width due to silica deposition is given by (Steefel, DePaolo, and Lichtner, 2005):

$$\frac{\partial \delta}{\partial t}|chemical = -\delta V_s R_s \tag{3.19}$$

Where α_T is the solid thermal expansion coefficient [K^{-1}] and δ is the half-fracture width [m]. The evolution of fracture aperture due to the combined thermoelastic and chemical effects is the sum of Eq. 3.18 and Eq. 3.19.

3.3.4 Numerical simulation

We use COMSOL multiphysics to solve the coupled partial differential equations (PDEs) describing the system. Using an explicit formulation of the finite element method, we define the porosity as a time-dependent variable. Note that the system is characterized by non-isothermal and single-phase incompressible fluid flow. Tables 3.1 and 3.2 show the rock and fluid input properties, and Table 3.3 shows the silica (as quartz) kinetics related data.

TABLE 3.1: Rock and fracture properties for the THC model. Subscript m, matrix (rock) and f, fracture.

Initial porosity of the rock, ϕ_o	0.1
Reaction rate constant in the rock matrix, K_m	10^{-6} s^{-1}
Initial matrix permeability, k_o	10^{-16} m^2
Density of the rock, ρ_m	2600 kg m^{-3}
Compressibility of the rock, β_m	1.10^{-10} Pa^{-1}
Effective solute diffusion coefficient, D_m	5.10^{-6} m^2 s^{-1}
Heat capacity of the solid, C_p^m	1000 J kg^{-1} K^{-1}
Solid heat conductivity, λ	2.6 W m^{-1} K^{-1}
Solid thermal expansion coefficient, α_T	1.8×10^{-5} K^{-1}
Poisson's ratio, ν	0.219
Half-fracture aperture, δ	2×10^{-4}-2×10^{-2} m
Reaction rate constant in the fracture, κ_f	10^{-8} s^{-1}
Thermal dispersivity, β_T	0.05 m
Initial reservoir temperature, T_o	250 °C

3.3.5 Model geometry and setup

We investigate two scenarios, with the first one represented in Figure 3.2, where we assume an injection fluid supersaturated with respect to silica flowing through the fracture and matrix system.

TABLE 3.2: Fluid properties for the THC model. Subscript w, fluid.

Fluid pressure difference, ($P_{inj} - P_o$)	1 MPa
Compressibility of the fluid, β_w	5.10^{-10} Pa^{-1}
Fluid heat capacity, C_p^w	4000 J kg^{-1} K^{-1}
Fluid density at reference temperature (at 20°C), ρ_0	1000 kg m^{-3}
Temperature of the injected fluid, T_{inj}	27 °C

TABLE 3.3: Quartz related data chosen for the THC model. Subscript q, quartz, and m, matrix.

Concentration of oversaturated injection fluid, C_{inj}	800 ppm
Density of quartz, ρ_q	2700 kg m^{-3}

The injection fluid maintains constant pressure, temperature and concentration of silica throughout the simulation. The second scenario, represented in Figure 3.3, assumes injection at the center of the fracture and porosity reduction occurring at the vicinity of the fracture. The injected fluid is also characterized by a constant pressure, temperature and concentration. The fluid is supersaturated with respect to silica. That is, the concentration in silica (as quartz) exceeds the equilibrium concentration. The porosity of the matrix varies according to Eq. 3.15 and the fracture permeability is re-calculated with respect to the change in fracture width calculated via Eq. 3.18 and 3.19.

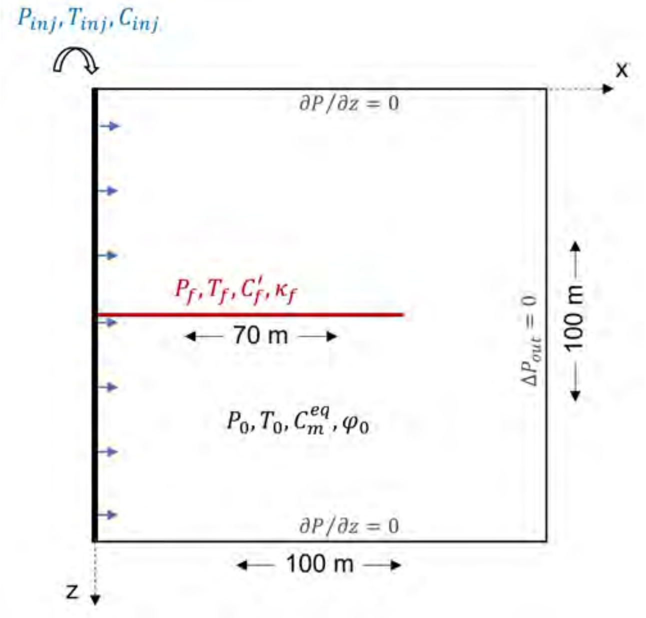

FIGURE 3.2: Simplified geometry of scenario 1, where P_{inj}, T_{inj}, C_{inj} are the injection pressure (in excess of hydrostatic), temperature and concentration in silica, respectively. $P_{m/f}$, $T_{m/f}$, $C_{m/f}$ are the pressure, temperature and concentration in silica in the matrix (m), and the fracture (f), respectively. We assume a 70 m long fracture with no flow boundary conditions at the top, bottom and right side and a constant injection fluid at the well (left).

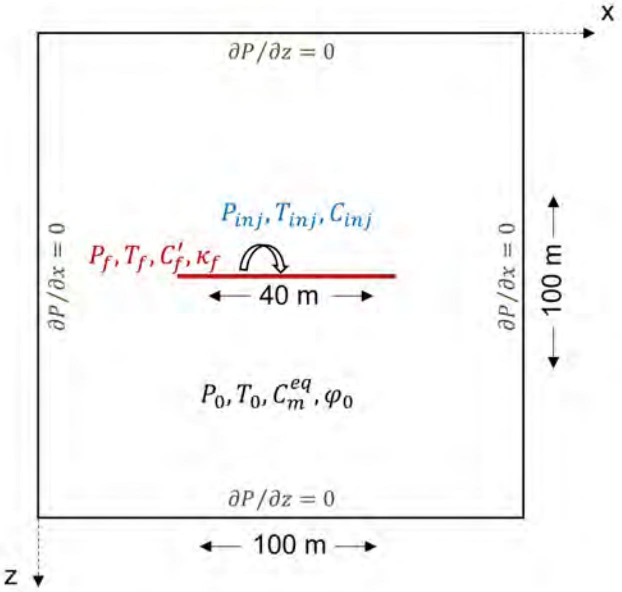

FIGURE 3.3: Simplified geometry of scenario 2, where P_{inj}, T_{inj}, C_{inj} are the injection pressure (in excess of hydrostatic), temperature and concentration in silica, respectively. $P_{m/f}$, $T_{m/f}$, $C'_{m/f}$ are the pressure, temperature and effective concentration of silica in the matrix (m), and the fracture (f), respectively. We assume a 40 m long fracture with no flow boundary conditions on all sides and a constant injection fluid at the center of the fracture.

3.4 Results and discussion

3.4.1 Injection well with fracture stimulation

We investigate the behavior of the well-fracture system in Figure 3.2 using SPARROW. Assuming a constant pressure, temperature and silica concentration in the well, we model the pressure, temperature and concentration within the fracture-matrix system undergoing changes in porosity and permeability. We perform a sensitivity analysis by assuming three increasing porosity reduction rates (Ψ_{min}, Ψ_{med}, Ψ_{max}), and infer the corresponding permeability. where Ψ_{min} is the porosity reduction rate calculated via Eq.3.4, and Ψ_{max} is the maximum porosity reduction rate found experimentally in Yanaze et al. (2019).

Figure 3.4 shows the results of (a) k/k$_0$ [1], (b) $d\phi/dt$ [s^{-1}], (c) porosity [1] and (d) Pressure [MPa] measured at 1[m] from the well an above the fracture, over a year period, assuming the three studied porosity reduction rates (Ψ_{min}, Ψ_{med} and Ψ_{max}). Figure 3.4(a) shows that the ratio of the new permeability to the initial permeability (K/K_o) reaches 55% after a year of injection in the case of the Ψ_{min} in comparison to less than 10 days in the case of Ψ_{max}. In a similar manner, the new porosity reduces to almost 7% after 1 year of injection in the case of the Ψ_{min}, in comparison to less than 10 days in the case of Ψ_{max} (Figure 3.4(c)). Figure 3.4(b) highlights the transient nature of the

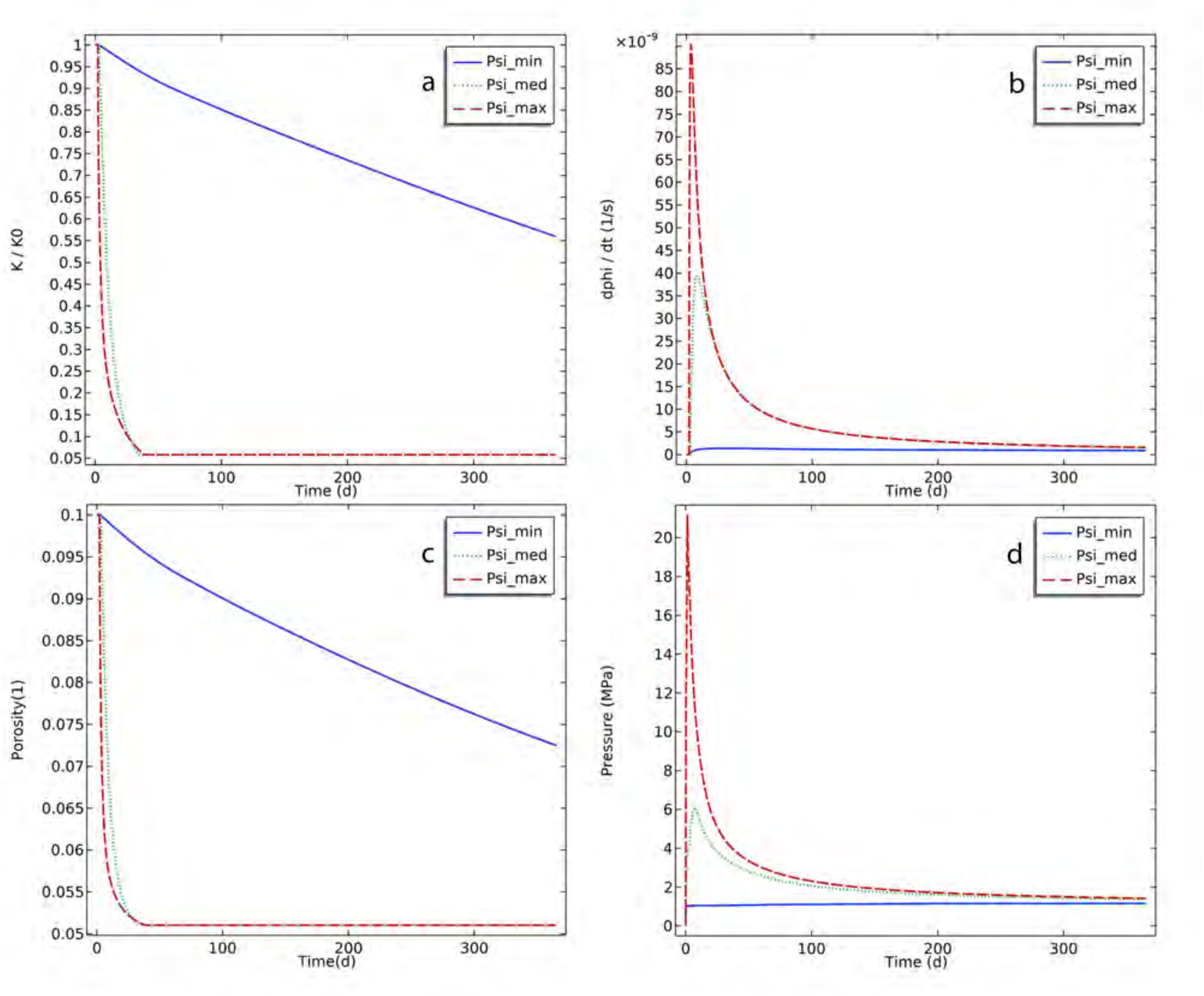

FIGURE 3.4: Comparison of (a) k/k$_0$, (b) $d\phi/dt$ [s^{-1}], (c) porosity and (d) Pressure [MPa] (measured at 1[m] from the well, over a year period) between three studied porosity reduction rates Ψ_{min}, Ψ_{med} and Ψ_{max}.

porosity reduction rate, which implicitly depends on the effective concentration of deposited silica, as seen in Eq.3.15. In the case of Ψ_{max}, the $d\phi/dt$ curve increases fast initially (due to increasing silica deposition) and peaks at $90 * 10^{-9}$[1/s] after almost 10 days of injection, then later decreases and stabilizes at $2 * 10^{-9}$[1/s] after a year of injection, while the porosity reaches its critical value almost 40 days after injection (Figure 3.4(c)). In comparison, in the case of Ψ_{min}, the $d\phi/dt$ curve reaches its steady value of $2 * 10^{-9}$[1/s] after 10 days of injection, remaining constant even after a year of injection. The calculated pore pressure, as seen in Figure 3.4(d), displays a behavior similar to that of the porosity reduction rate curve in Figure 3.4(b), peaking and decreasing at identical times. The pore pressure is more sensitive to the porosity reduction rate than the porosity value, which is to be expected because of the mass conservation equation Eq.3.3. Figure 3.4(d) shows that the peak value of pore pressure (in excess of hydrostatic), reaches an impressive 22[MPa] in the case of Ψ_{max}, 6[MPa] in the case of Ψ_{med}, and 1.2[MPa] after 10 days of injection. That is, an abrupt loss in porosity leads to a surge in pore pressure, as seen for Ψ_{max}, whereas a smaller porosity reduction rate Ψ_{min} has a negligible effect on the systems pore pressure increase, despite a noticeable drop in porosity, about 30% after a year.

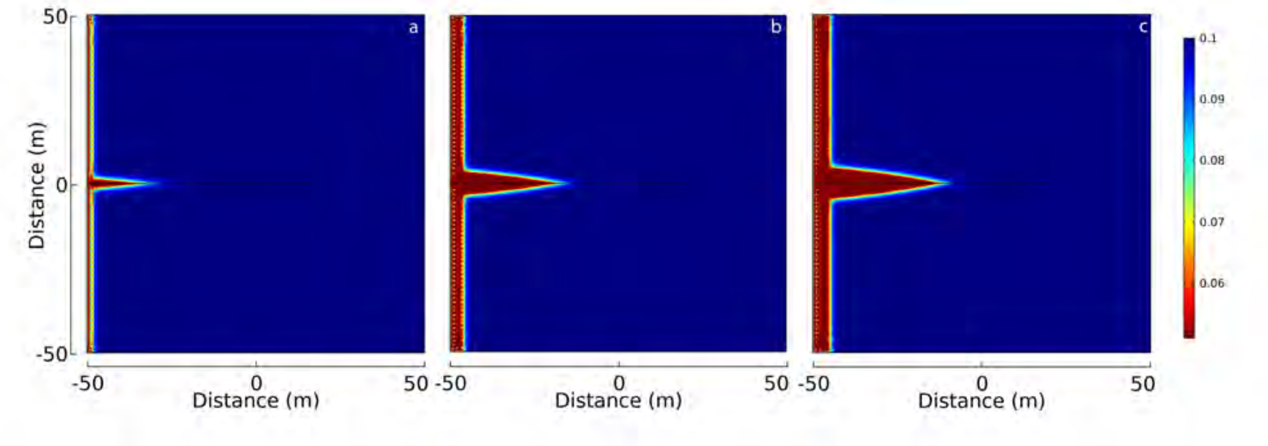

FIGURE 3.5: Comparison of porosity between (a) Ψ_{min} and (b) Ψ_{max} after one year of injection.

Figure 3.5 shows porosity assuming (a) Ψ_{min}, (b) Ψ_{med} and (c) Ψ_{max}, calculated 365 days after injection. Results show that porosity reduction is substantial at the vicinity of the vertical well because of the imposed boundary condition, where the injection fluid is supersaturated with respect to silica leading to deposition as the fluid travels inside the medium. In addition, results indicate that porosity reduction is more prominent and travels faster at the vicinity of the fracture. There are two main reasons for this. First, the effective concentration of deposited silica is larger and occurs faster inside the fracture, leading to a larger concentration gradient at the fracture/matrix interface, and consequently a larger porosity reduction rate Ψ. The second reason is the presence of the leakoff from the fracture to the matrix and hence the presence of an advection causing larger silica deposition at the fracture-matrix interface.

Figure 3.6 compares fluid pressure between (1) constant porosity (cp), (2) Ψ_{min}, (3) Ψ_{med}, and (4) Ψ_{max}, calculated (a) 5 days, (b) 10 days and (c) 30 days after injection. The injection fluid is assumed to be 1[MPa] above hydrostatic and results show that pore pressure builds up inside the medium to exceed that of the injection pressure in the presence of porosity reduction. Figure 3.6 shows that pore pressure builds up to become 1.2[MPa] above hydrostatic after 30 days in the case of Ψ_{min} (Figure 3.6(2.c)), 12[MPa] above hydrostatic after 10 days of injection in the case of Ψ_{med} (Figure 3.6(3.b)), and

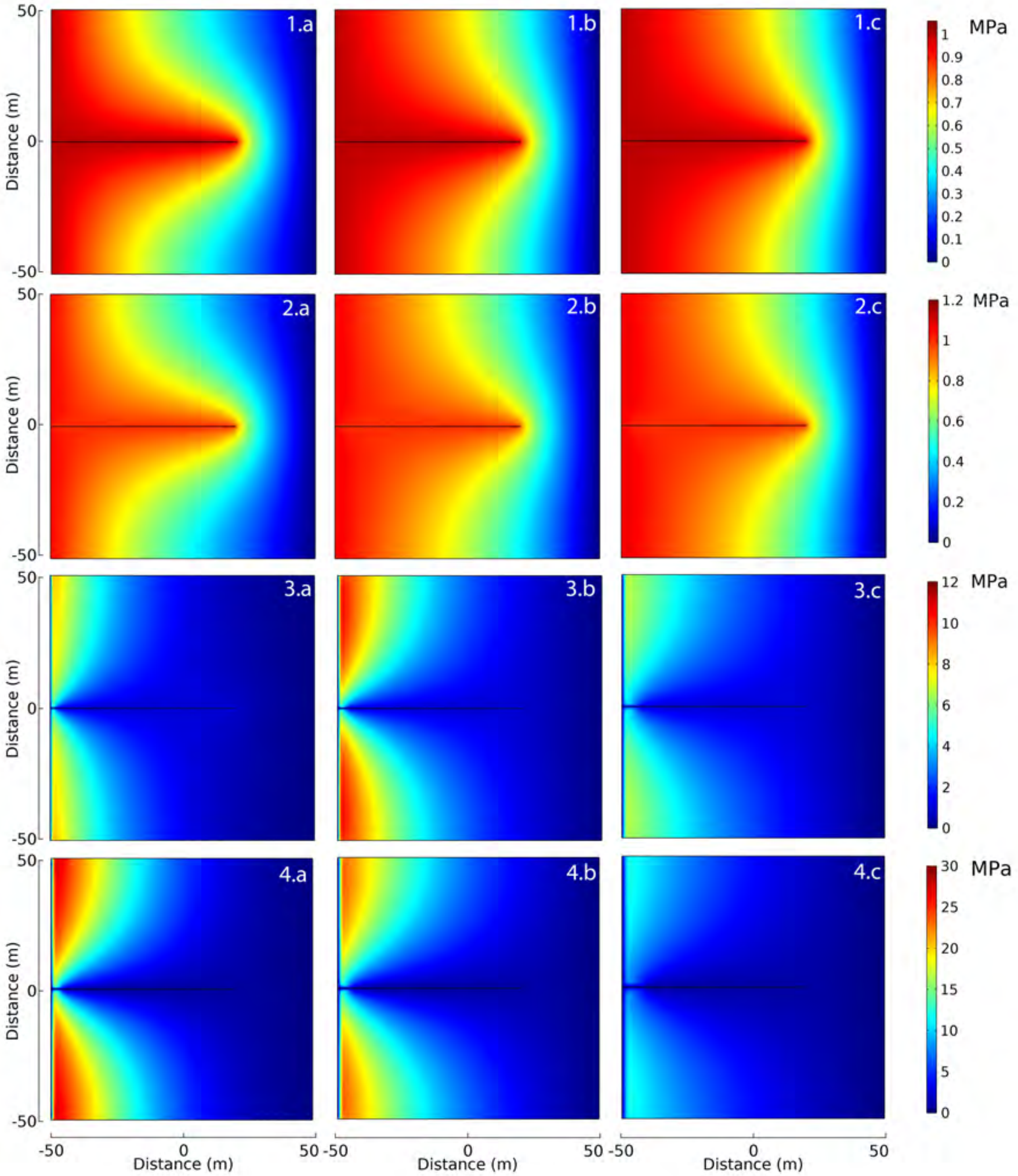

FIGURE 3.6: Comparison of pore pressure in excess of hydrostatic, between (1) constant porosity (cp), (2) Ψ_{min}, (3) Ψ_{med}, and (4) Ψ_{max}, calculated (a) 5 days, (b) 10 days and (c) 30 days after injection.

30[MPa] above hydrostatic after 5 days of injection in the case of Ψ_{max} (Figure 3.6(4.a)). Results clearly show that overpressure (pressure above hydrostatic) depends on the initial porosity reduction rate and not the newly found porosity, because although the matrix porosity in Figures 3.6(3-4) reaches the critical value, the pore pressure is higher for the fastest porosity reduction rate. An more abrupt loss of porosity, such is the case of Ψ_{max} (Figure 3.6(4.a)), forces the system to accommodate a pore pressure buildup, leading to overpressure. That is, the fluid pressure in the fractured system exceeds that of the injection well, thus generating a reversed Darcy flow. For clarity, a reversed Darcy flow is the Darcy flow in reversed direction, contrary to what is to be expected at an injection well. Figure 3.7 shows pore pressure 365 days after injection, assuming (a) Ψ_{min}, (b) Ψ_{med} and (c) Ψ_{max}. Note that porosity reduction rate decreases and stabilizes at this point, and the porosity reaches the critical value for the cases Figure 3.7(b-c). Results clearly show that overpressure is still present in the system after a year of injection. The encountered reversed Darcy flow affects the advection term, hence affecting temperature and concentration evolution in the system and consequently, the evolution of fracture width. In this example, we consider the fracture has a constant porosity of one [1] but undergoes fracture aperture, therefore permeability, variation with an initial width b=2x10^{-4}[m].

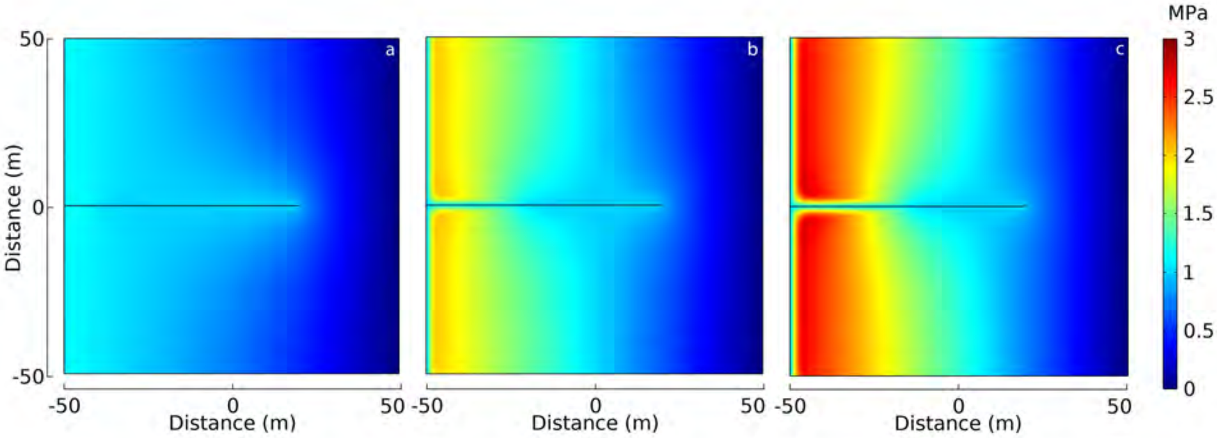

FIGURE 3.7: Pore pressure assuming a maximum porosity reduction rate Ψ_{max}, (a) 100 days and (b) 365 days after injection.

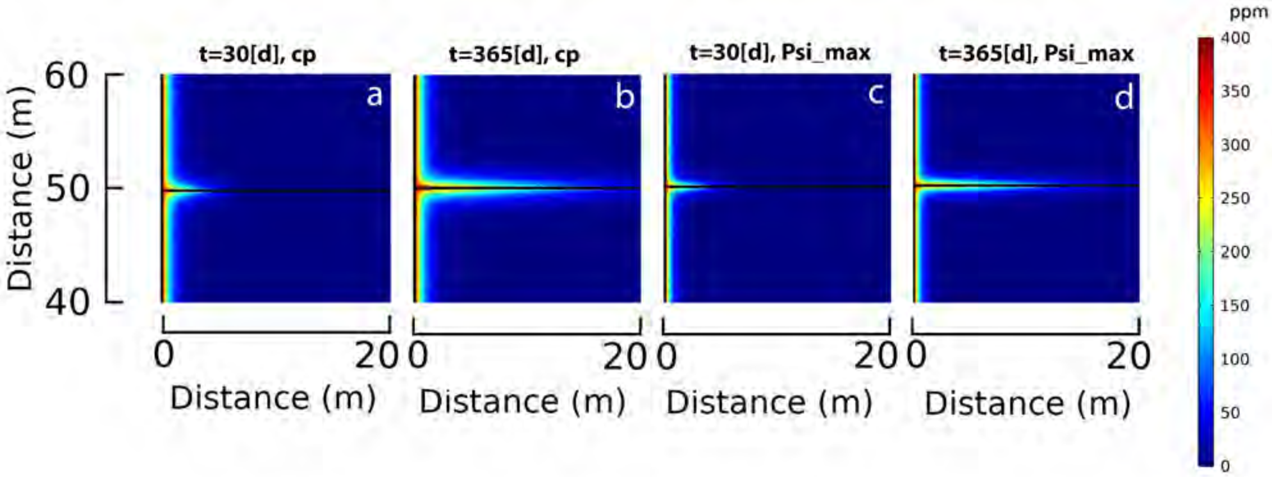

FIGURE 3.8: Concentration of silica (as quartz) 30 days after injection, assuming (a) constant porosity (cp) and (b) Ψ_{max}, and a year after injection, assuming (c) constant porosity (cp) and (d) Ψ_{max}.

Figure 3.8 shows the effective silica (as quartz) concentration assuming constant porosity (cp), (a)

30 days after injection and (b) a year after injection, and assuming Ψ_{max}, (c) 30 days after injection and (d) a year after injection. Results indicate a decrease in effective silica concentration in the presence of a porosity reduction rate, by comparing Figures 3.8(a-c), 30 days after injection, and Figures 3.8(b-d), after 1 year of injection. The reduction is observable at the fracture-matrix interface and the vicinity of the well due to the decrease in the pore space that can accommodate more depositing silica. Furthermore, a reversed Darcy flow also means that silica may be transported backwards towards the well, inducing lower injectivity. Note that we consider the advection term for both the matrix and the fracture.

We proceed to examine the temperature, assuming constant porosity 30 days Figure 3.9(a) and 365 days Figure 3.9(b) after injection, and assuming Ψ_{max} presented 30 days Figure 3.9(c) and 365 days Figure 3.9(d) after injection.

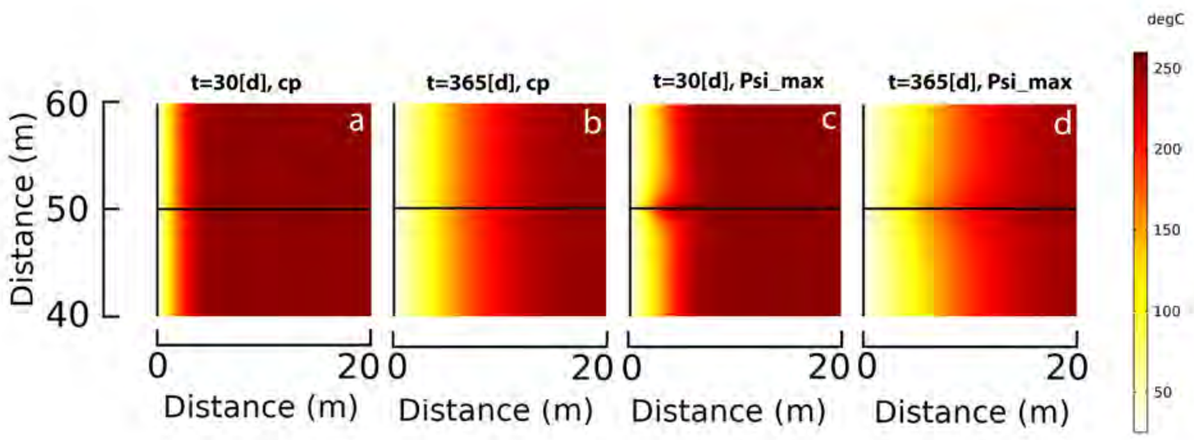

FIGURE 3.9: Temperature calculated after 30 days of injection assuming (a)constant porosity and (c)Ψ_{max}, and 365 days after injection, assuming 30 days (b)constant porosity (d)Ψ_{max}.

Results in Figure 3.9 show the effects of the reversed Darcy flow, induced by fast porosity reduction rates, on the temperature front. We observe that at similar times, the cooling front propagates farther in the case of Ψ_{max} Figure 3.9(c-d) than in the case of constant porosity Figure 3.9(a-b) because of the reversed Darcy flow; temperature flows from the matrix to the well. Furthermore, a larger cooling front extends further along the fracture-matrix interface in the case of Ψ_{max} because of the leakoff, where the shape of the temperature front along the fracture-matrix interface clearly takes a '<' shape, indicating a reversed Darcy flow. As the porosity reduction rate stabilizes and pore pressure slowly reaches steady state, the effects of the reversed Darcy flow should slowly diminish after a year of injection in the case of Ψ_{max}.

Figure 3.10 shows fracture width evolution for different porosity reduction rates, assuming an initial fracture aperture of (a) 0.02[m] and (b) 0.005[m]. We fix the boundary condition of the fracture aperture as variable at the injection point and equal to the initial fracture width at the tip located at 70[m]. Fracture width evolution is not affected by porosity reduction rates at early times, as calculated 30 days after injection, but varies 100 days and 365 days after injection. After 365 days of injection, fracture width is largest for the highest porosity reduction rate Ψ_{max}, highlighting the thermoelastic effects due to silica deposition. After a year of injection and comparing between constant porosity and Ψ_{max}, fracture width is 1[mm] larger for w_0=0.005[m] (Figure 3.10(a)), and 2.5[mm] larger for w_0=0.02[m] (Figure 3.10(b)), measured at 20[m] from the tip of the fracture. This observation is due to the loss of heat as the fluid flows from the hot reservoir back to the injection well caused by the reversed Darcy flow, in the presence of Ψ_{max}. In consequence, an increased displacement of the fracture takes place, thus increasing its likelihood of failure. Furthermore, a larger initial fracture aperture results in a larger fracture width increase due to higher thermoelastic effects.

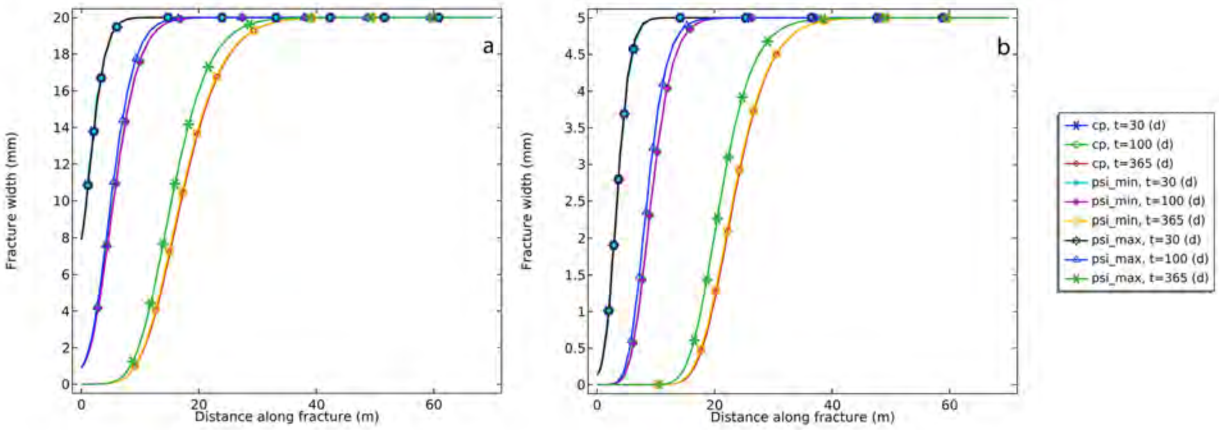

FIGURE 3.10: Evolution of the fracture width 30 days, 100 days and 365 days after injection, assuming (a) w_0=0.005 [m] and (b) w_0=0.02 [m].

Figure 3.11 shows (a) pressure and (b) temperature along the fracture 365 days after injection, assuming the three studied porosity reduction rates and the two initial fracture width w_0=0.005[m] and w_0=0.02[m]. Figure 3.11(a) shows that the pressure in excess of hydrostatic peaks higher when assuming maximum porosity reduction rate, 5.5[MPa] when Ψ_{max} in comparison to 3.7[MPa] when Ψ_{min}. The effects of this larger reversed Darcy flow can be seen in Figure 3.11(b), where temperature is smallest assuming Ψ_{max} and w_0=0.005[m].

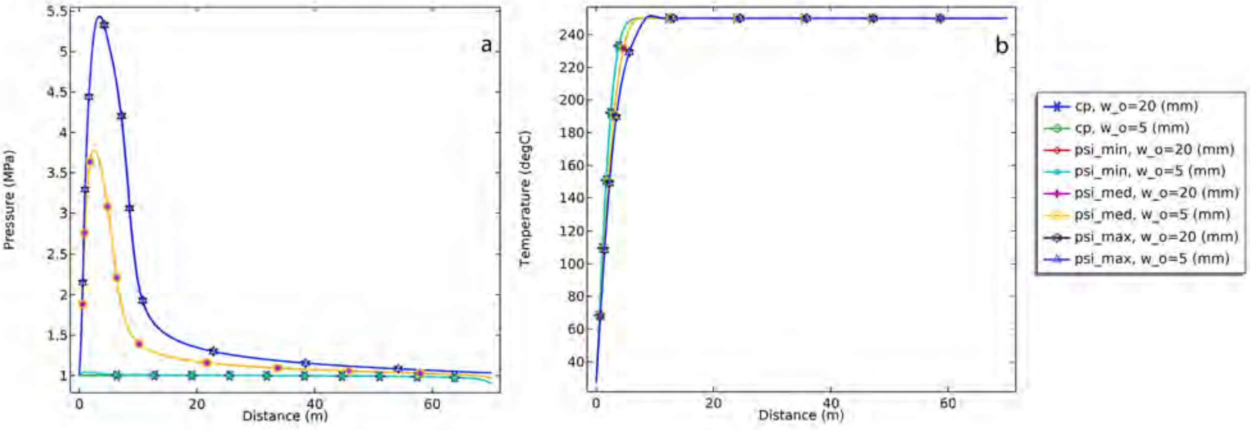

FIGURE 3.11: Evolution of the (a) pressure and (b) temperature along the fracture 365 days after injection, assuming different porosity reduction rates and for two values of initial fracture width w_0=0.005[m] and w_0=0.02[m].

3.4.2 Matrix with pre-existing fracture

In this section, we investigate the effects of silica deposition in a pre-existing fracture and source at its center, as shown in Figure 3.3, using SPARROW. Assuming a constant pressure, temperature and silica concentration at the fracture center, we model the pressure, temperature and concentration components in the fracture-matrix system undergoing porosity and permeability changes. Figures 3.12 shows fluid pressure assuming a porosity reduction rate of (a) Ψ_{min} , (b) Ψ_{med}, and (c) Ψ_{max}, calculated at (1) 10 days, (2) 30 days and (3) 365 days after injection.

Overpressure (pressure in excess of hydrostatic) occurs in all three scenarios of porosity reduction and is 2[MPa] assuming Ψ_{min} (Figure 3.12(1.a)), 4[MPa] assuming Ψ_{med} (Figure 3.12(1.b)), and 10[MPa] assuming Ψ_{max} (Figure 3.12(1.c)), calculated 10 days after injection. The pore pressure buildup is governed by the porosity reduction rate and not the newly calculated porosity, as can be seen in Figure 3.13, where the porosity at the vicinity of the fracture reaches the critical porosity of 0.05 in all three cases of porosity reduction rates. After 365 days, fluid pressure is 1.2[MPa] assuming Ψ_{min} (Figure 3.12(3.a)), 1.8[MPa] assuming Ψ_{med} (Figure 3.12(3.b)), and 3.5[MPa] assuming Ψ_{max} (Figure 3.12(3.c)). The surge in pore pressure is clustered at the vicinity of the injection point because of the larger silica deposition and hence porosity reduction. Results show that the excess pore pressure dissipates from the fracture for all cases, and reaches the boundaries, mostly due to the no flow condition, specifically for the Ψ_{med} (10%) and Ψ_{max} (16%) case, shown in Figure 3.13(b-c),respectively. The resulting overpressure (Figures 3.14 and 3.15) affects the advection term, the concentration of silica, and the temperature evolution.

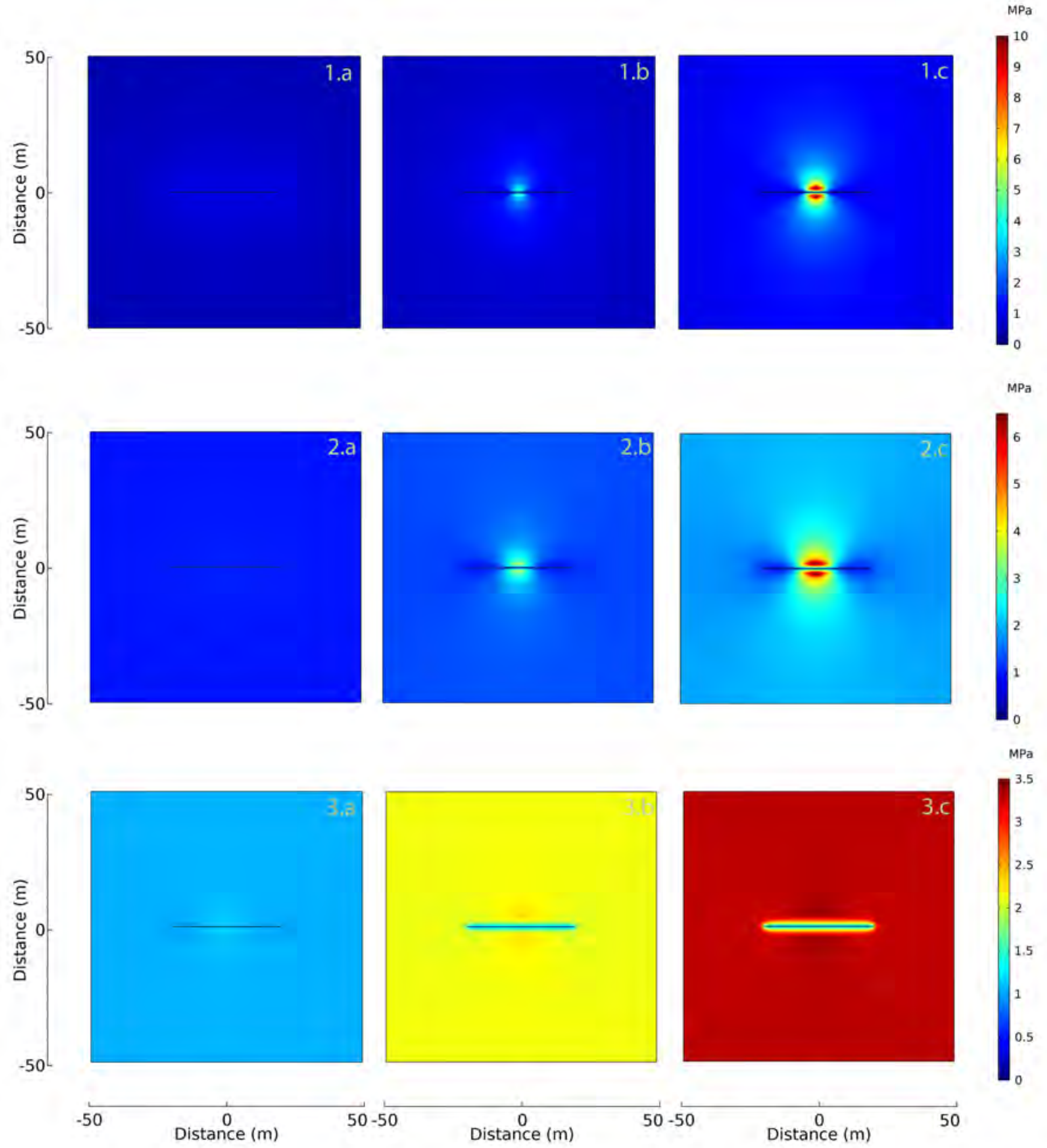

FIGURE 3.12: Pore pressure after [1] 10 days, [2] 30 days, and [3] 365 days of injection, assuming (a) Ψ_{min}, (b) Ψ_{med}, and (C) Ψ_{max}.

Figure 3.13 shows the calculated porosity a year after injection at the vicinity of the fracture, assuming a porosity reduction rate of (a) Ψ_{min}, (b) Ψ_{med}, and (c) Ψ_{max}. The porosity at the vicinity of the fracture reaches critical porosity for all three cases, with the largest region of reduced pororsity in the case of Ψ_{max}.

Figure 3.14 shows the silica concentration 30 days and 365 days of injection, assuming constant porosity (cp), and Ψ_{max}. For the same time step, one clearly sees the decrease in the concentration of deposited silica at the center of the fracture due to the decrease of the pore space in that region. Although not shown, once the system reaches the critical porosity and the porosity reduction rate

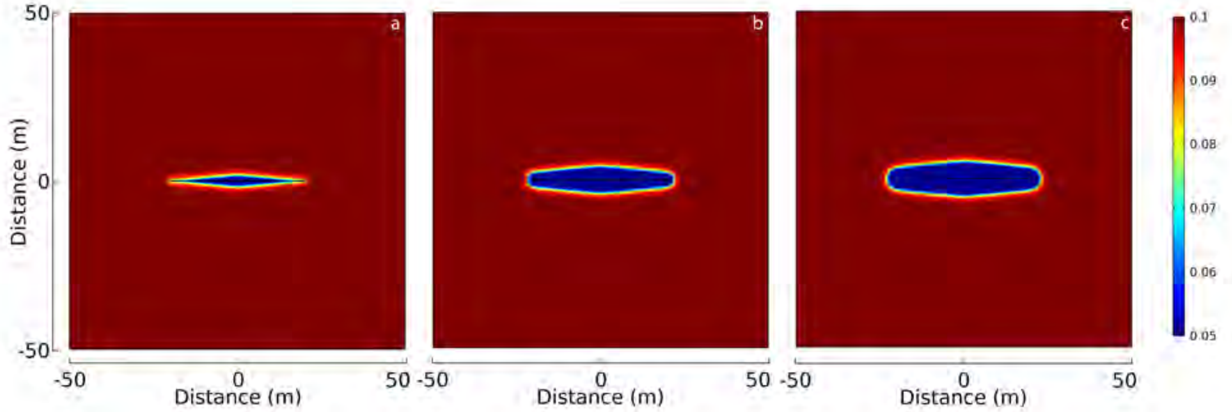

FIGURE 3.13: Porosity after 365 days, assuming (a) Ψ_{min}, (b) Ψ_{med}, and (C) Ψ_{max}.

nears zero, the concentration of deposited silica reaches a plateau and does not vary; for example between 100 days and 365 days.

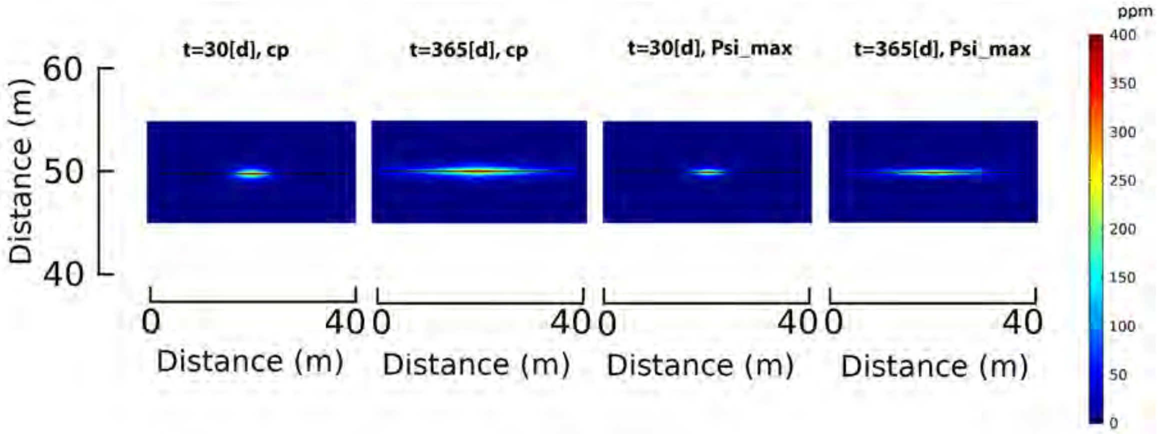

FIGURE 3.14: Effective silica concentration after [1] 30 days and [2] 365 days of injection, assuming (a) constant porosity (cp), and (b) Ψ_{max}.

Finally, Figure 3.15 shows temperature evolution after [1] 10 days, [2] 30 days, and [3] 365 days of injection, assuming (a) constant porosity, (b) Ψ_{med}, and (c) Ψ_{max}. We do not show the temperature assuming Ψ_{min} because it is the same as the temperature at constant porosity. Results show that the thermal cooling front due to the cold fluid injection becomes more pronounced in the presence of abrupt loss in porosity, as seen at all times for the cases of Ψ_{max} Figure 3.15(1.c-2.c-3.c). This is due to the negative pressure gradient, that transports the temperature from the surrounding rock towards the injection source, leading to a larger zone of decreased temperature around the fracture. These results are important because they show that porosity reduction affects the value and propagation radius of the thermal stresses acting along the fracture-matrix interface.

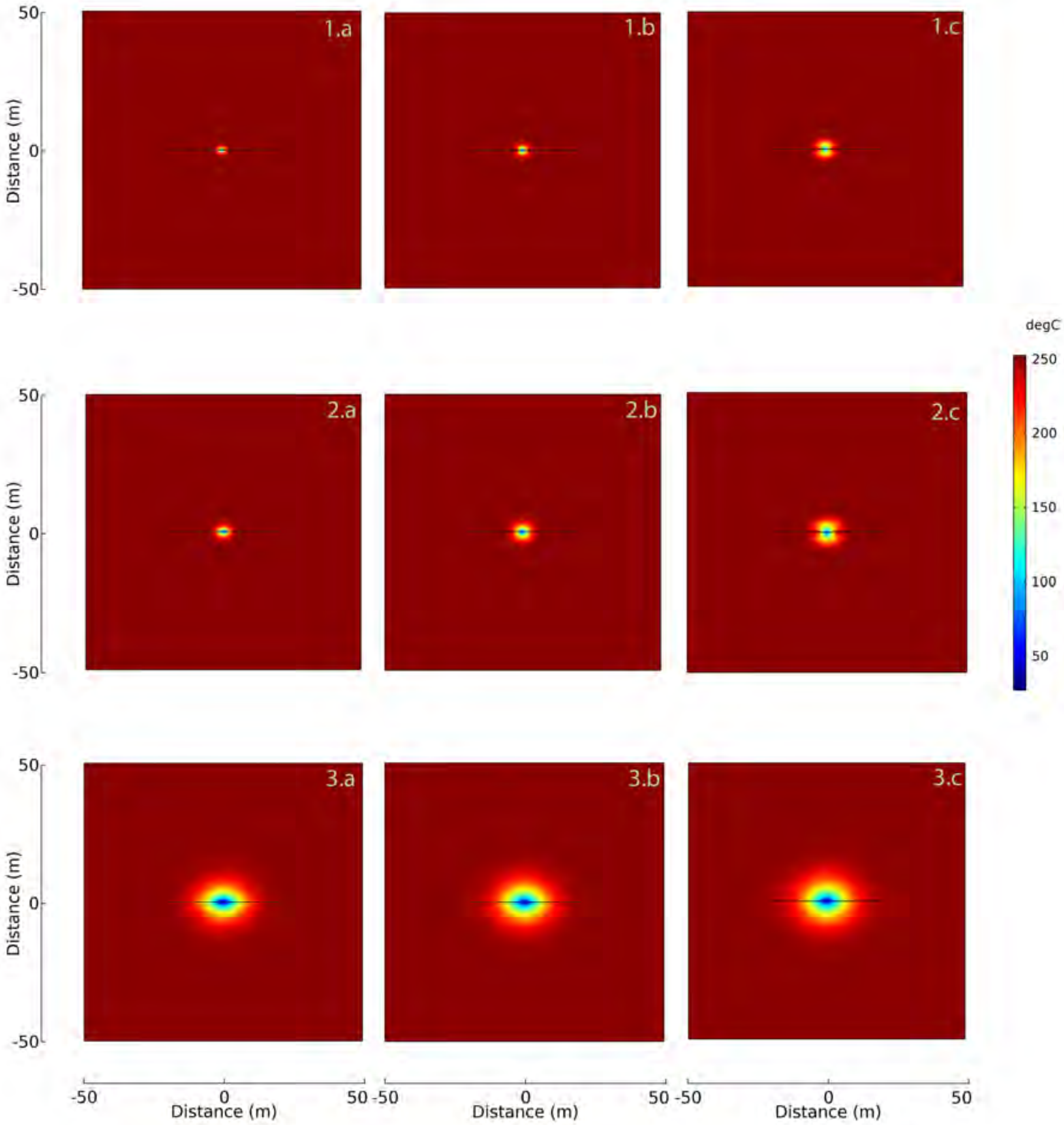

FIGURE 3.15: Temperature evolution after [1] 10 days, [2] 30 days, and [3] 365 days of injection, assuming (a) constant porosity, (b) Ψ_{med}, and (c) Ψ_{max}.

3.4.3 Implications on rock-fracture stability

We evaluate in this section the failure potential of a rock due to silica rich-pore clogging injection fluid. We assume a combination of SPARROW and the simple Mohr-Coulomb (MC) failure condition for a point in a cohesionless and frictional rock with a friction failure slope μ of 0.6. We assume that the rock fails when $\tau - \mu\sigma_n^{'} > 0$, where τ is the shear stress [MPa], and $\sigma_n^{'}$ is the effective normal stress [MPa]. We consider a maximum horizontal stress σ_1 of 45[MPa] and σ_3 of 20[MPa], respectively. Figure 3.16 shows the Mohr-Coulomb failure criterion for constant porosity, Ψ_{med}, and Ψ_{max} calculated 5 days after injection.

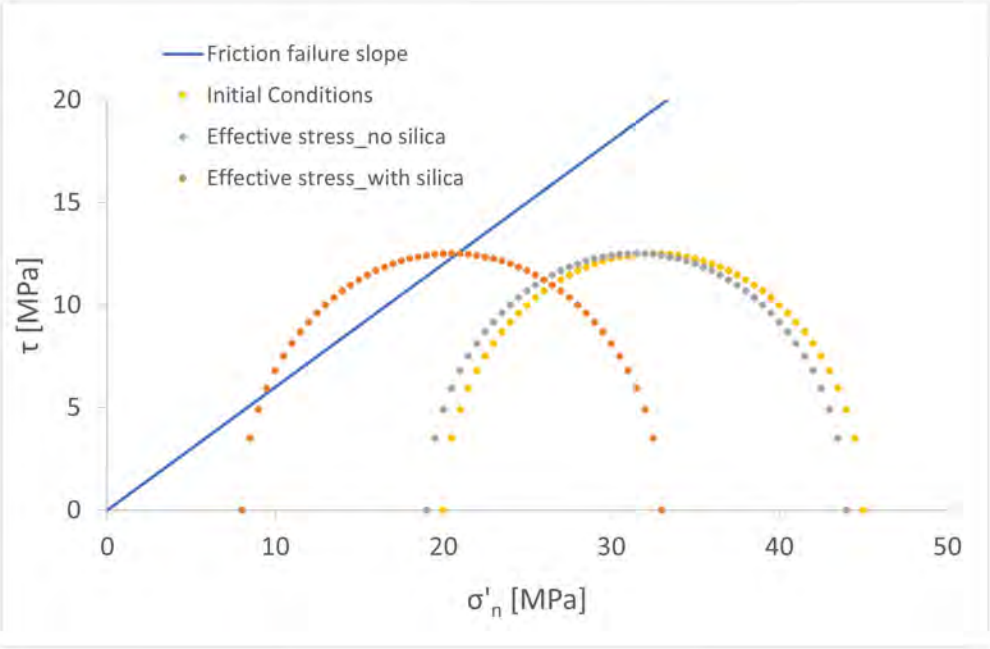

FIGURE 3.16: Mohr's circle assuming a cohesionless frictional rock with a friction failure slope μ of 0.6. We presume a maximum horizontal stress σ_1 of 45[MPa] and σ_3 of 20[MPa] respectively, each acting in the far field. We present the effective normal and shear stresses acting on the rock assuming the initial conditions, constant porosity and a porosity reduction rate of Ψ_{max}, calculated 5 days after injection.

Assuming isotropic, homogeneous formation, the effective normal stress acting on the fracture (when neglecting thermal stresses) is defined as:

$$\sigma_n^{'} = \frac{\sigma_1 + \sigma_3 - 2p_f}{2} + \frac{\sigma_1 - \sigma_3}{2} cos(2\theta) \tag{3.20}$$

$$\tau = \frac{\sigma_1 - \sigma_3}{2} sin(2\theta) \tag{3.21}$$

where θ is the angle between the maximum horizontal stress and the fracture segment measured from the normal to the σ_1 plane. Figure 3.16 shows that the Mohr's circle for initial stress state shifts to the right when introducing effective stresses, and intersects with the failure slope.

To further detail the results, Figure 3.17 shows that assuming pore pressure at constant porosity reduction, fractures with an inclination range of 35°-85°are stable.

However, inclination angles 55°and 65°fulfill the failure requirement when introducing the medium porosity reduction rate. The excess pore pressure, e.g. in excess of hydrostatic, allows inclinations of 45°-85°to slip in the end case scenario of Ψ_{max}. Figure 3.18 displays the values of effective normal stress on a fracture with an inclination of 65°, assuming (a) constant porosity, (b)

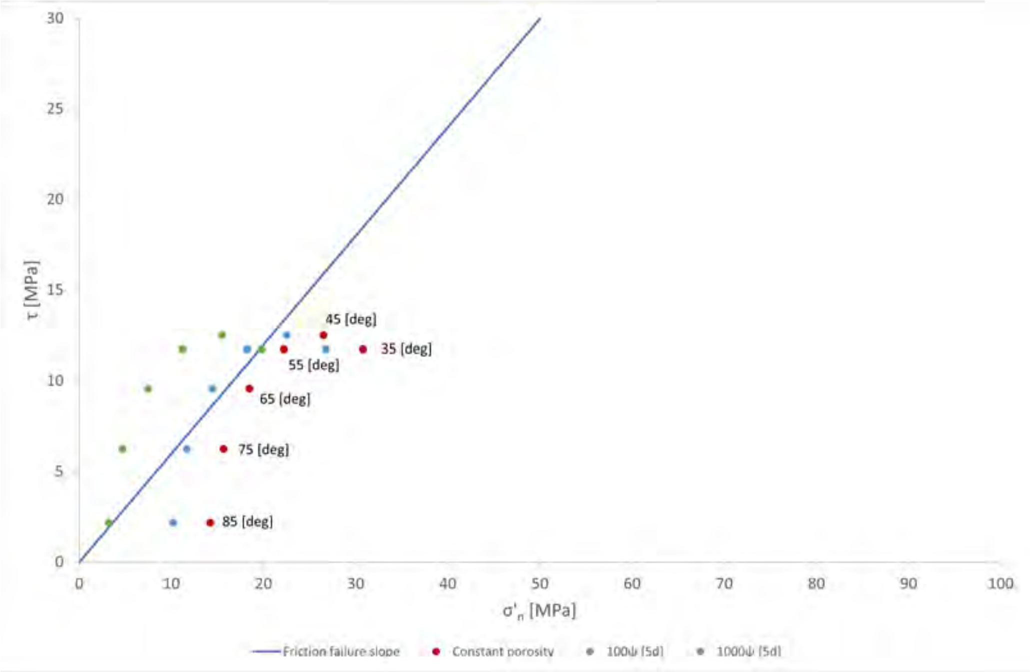

FIGURE 3.17: Failure study of a fracture for angle ranges (35,85) (notation above red dots), assuming a cohesionless rock with a friction failure slope μ of 0.6. We presume a maximum horizontal stress σ_1 of 45[MPa] and σ_3 of 20[MPa] respectively, each acting in the far field. The plot displays effective normal and shear stresses acting on the rock, assuming constant porosity and porosity reduction rates of Ψ_{med} and Ψ_{max}.

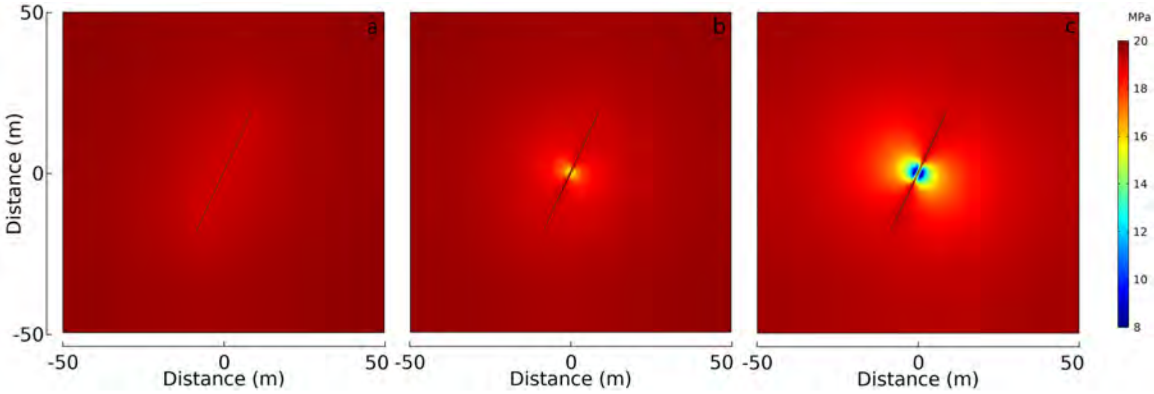

FIGURE 3.18: Effective normal stress after 5 days of injection, assuming a 65°inclination angle of the fracture, and (a) constant porosity, (b) Ψ_{med}, (c) Ψ_{max}

Ψ_{med}, and (c) Ψ_{max}. The effective stress at the center of the fracture (Figure 3.18 (c)) assuming Ψ_{max} is 8[MPa], more than half of the one calculated assuming constant porosity 18[MPa] (Figure 3.18(c)).

3.4.4 Sensitivity analysis

We perform a sensitivity analysis to understand the weight of two variables: pressure injection rate, and concentration of silica in the injection fluid, assuming input values given by Rawal and Ghassemi, 2014. Tables 3.4, 3.5 and 3.6 present the values used to study the behavior of the pressure, temperature, concentration and fracture aperture profiles assuming larger injection fluid pressure and silica concentration.

TABLE 3.4: Rock and fracture properties for the THC model. Subscript m, matrix (rock) and f, fracture.

Initial porosity of the rock, ϕ_o	0.1
Reaction rate constant in the rock matrix, K_m	10^{-6} s^{-1}
Initial matrix permeability, k_o	10^{-16} m^2
Density of the rock, ρ_m	2600 kg m^{-3}
Compressibility of the rock, β_m	1.10^{-10} Pa^{-1}
Effective solute diffusion coefficient, D_m	5.10^{-6} m^2 s^{-1}
Heat capacity of the solid, C_p^m	1000 J kg^{-1} K^{-1}
Solid heat conductivity, λ	2.6 W m^{-1} K^{-1}
Solid thermal expansion coefficient, α_T	1.8x10^{-5} K^{-1}
Poisson's ratio, ν	0.219
Half-fracture aperture, δ	2x10^{-4}-2x10^{-2} m
Reaction rate constant in the fracture, κ_f	10^{-8} s^{-1}
Thermal dispersivity, β_T	0.05 m

TABLE 3.5: Fluid properties for the THC model. Subscript w, fluid.

Injection fluid pressure, P_{inj}	10 MPa
Compressibility of the fluid, β_w	5.10^{-10} Pa^{-1}
Fluid heat capacity, C_p^w	4000 J kg^{-1} K^{-1}
Fluid density at reference temperature (at 20°C), ρ_0	1000 kg m^{-3}
Temperature of the injected fluid, T_{inj}	40 °C

TABLE 3.6: Quartz related data chosen for the THC model. Subscript q, quartz, and m, matrix.

Concentration of oversaturated injection fluid, C_{inj}	1000 ppm
Density of quartz, ρ_q	2700 kg m^{-3}

Similar to the previously presented results, we investigate the behavior of the well-fracture system in Figure 3.2 using SPARROW. Assuming a constant pressure, temperature and silica concentration at the injection well, we model the pressure, temperature and concentration within the fracture-matrix system undergoing porosity and permeability changes. We also study three increasing porosity reduction rates (Ψ_{min} Ψ_{med}, Ψ_{max}), and infer the corresponding permeability.

Figure 3.19 shows the results of (a) k/k$_0$ [1], (b) $d\phi/dt$ [s^{-1}], (c) porosity [1] and (d) Pressure [MPa] measured at 1[m] from the well, over a year period, assuming the three studied porosity reduction rates. In Figure 3.19(a), the ratio of the new permeability to the initial permeability is 25% after 10 days, and the new porosity is 6% (Figure 3.19(c)) assuming Ψ_{max}, and 85% after a year, and the new porosity is 8% (Figure 3.19(c)) assuming Ψ_{min}. Results highlight the transient nature of the porosity

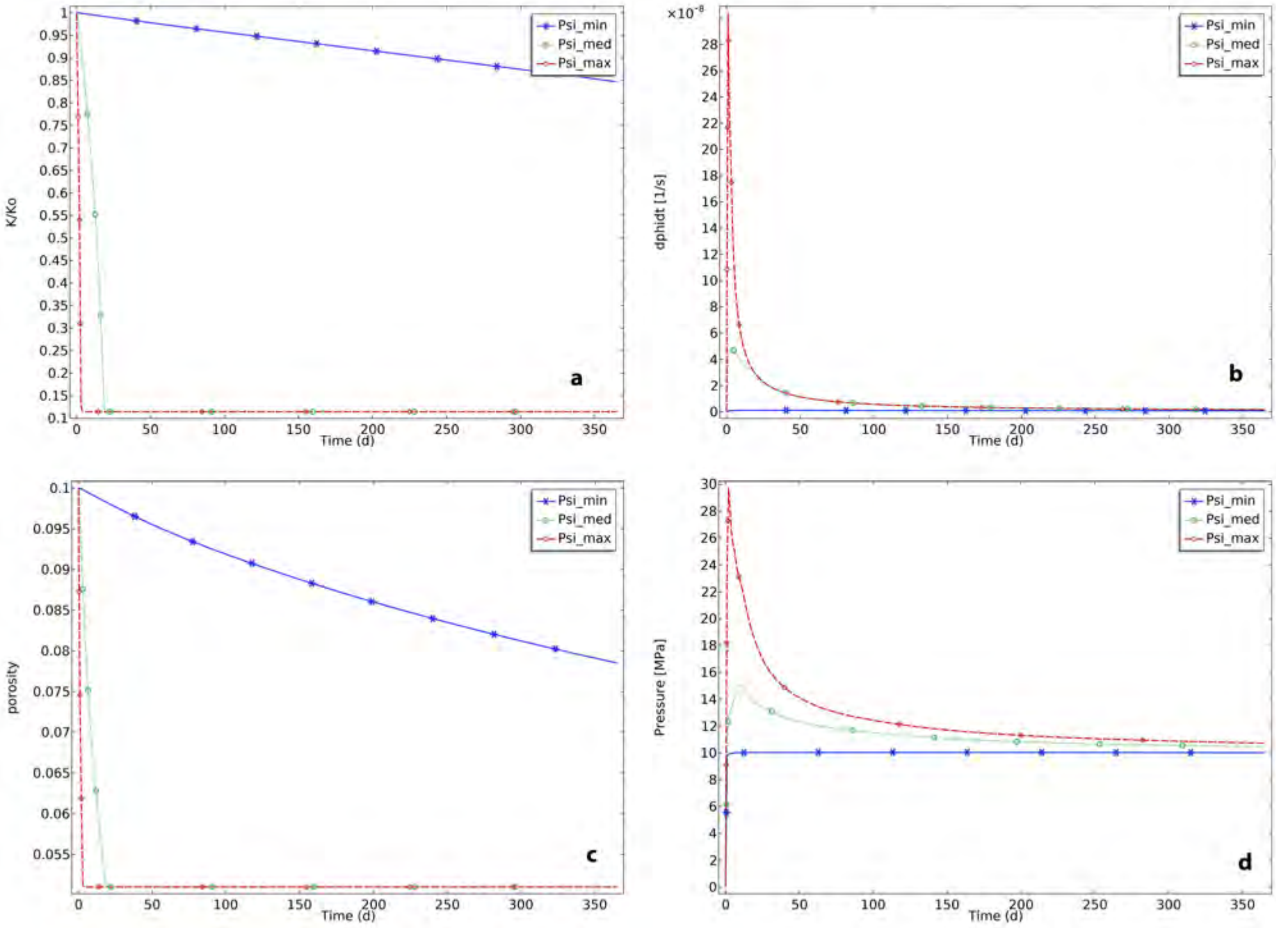

FIGURE 3.19: Comparison of (a) k/k$_0$, (b) $d\phi/dt$ [s^{-1}], (c) porosity and (d) Pressure [MPa] (measured at 1 m] from the well, over a year period) between three studied porosity reduction rates (a) Ψ_{min}, (c) Ψ_{med} and (e) Ψ_{max}.

reduction rate (Figure 3.19(b)), which is initially fast (due to increasing silica deposition) and later stabilizes as the system reaches the critical porosity (Figure 3.19(c)). Figure 3.19(c) indicates that the porosity reaches the critical value after 10 days assuming Ψ_{max}, and after 25 days assuming Ψ_{med} and over a year assuming Ψ_{min}. Figure 3.19(d) shows that the pore pressure depends more on the initial porosity reduction rate rather than the porosity value. An abrupt loss in porosity leads to a surge in pore pressure, seen for Ψ_{max}, whereas a smaller porosity reduction rate, such as Ψ_{min} has negligible effect on the system despite a noticeable drop in porosity, about 20% after a year.

Figure 3.20 shows porosity reduction rates, assuming (a) Ψ_{min}, (b) Ψ_{max} and the corresponding porosity Figure 3.20(c) and 3.20(d), respectively, calculated 365 days after injection. Results indicate that porosity reduction is more prominent and travels faster at the vicinity of the fracture. There are two main reasons for this. First, the concentration of silica is larger and occurs faster inside the fracture, leading to a larger concentration gradient at he fracture/matrix interface, and consequently a larger Ψ. The second reason is the presence of the leakoff from the fracture to the matrix and hence the presence of an advection causing larger silica deposition at the fracture-matrix interface. Furthermore, porosity reduction is important at the vicinity of the vertical well because there deposits high concentrations of silica.

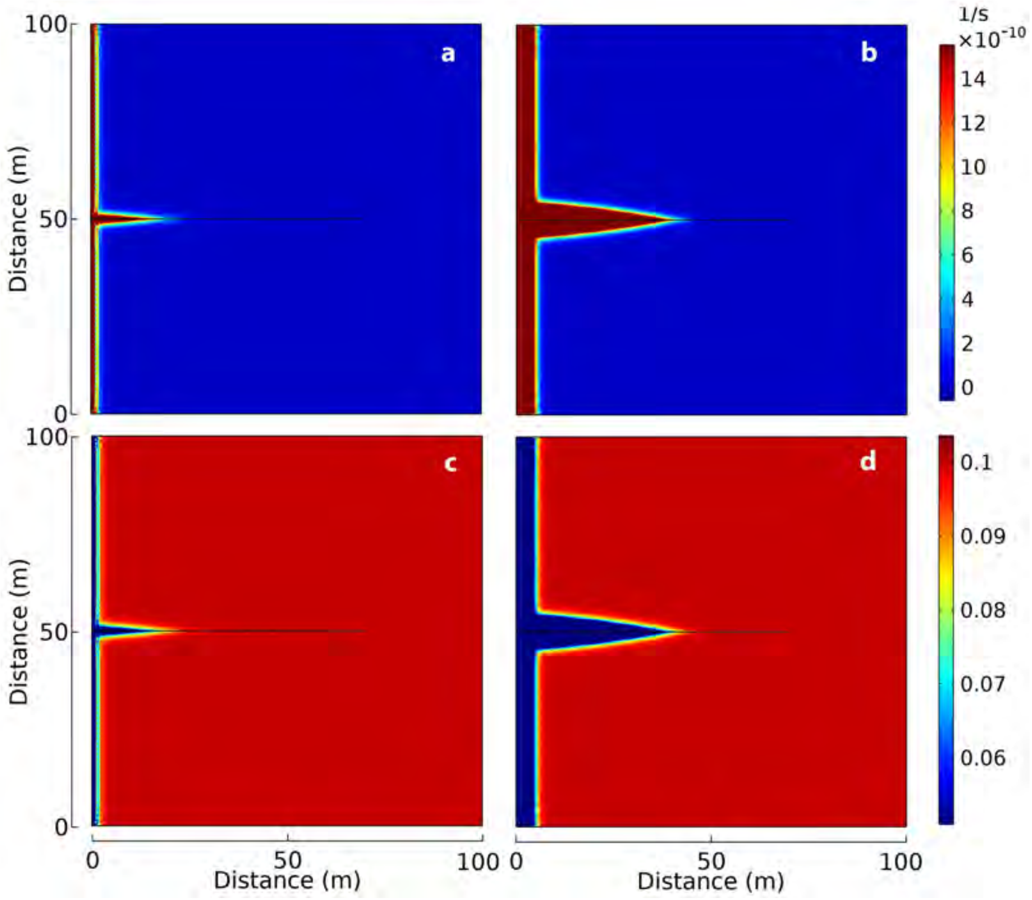

FIGURE 3.20: Comparison of porosity reduction rates between (a) Ψ_{min} and (b) Ψ_{max}, and their corresponding porosity at (c) and (d) respectively, after one year of injection.

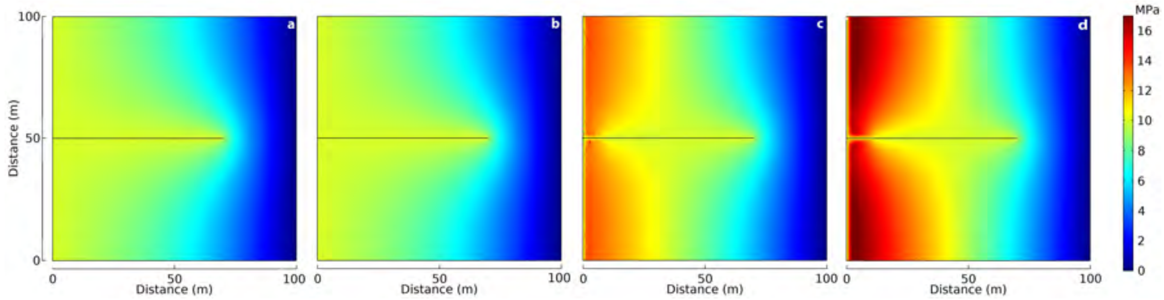

FIGURE 3.21: Comparison of pore pressure, 30 days after injection, between (a) constant porosity (cp), (b) Ψ_{min}, (c) Ψ_{med}, and (d) Ψ_{max}.

Figure 3.21 compares fluid pressure between (a) constant porosity (cp), (b) Ψ_{min}, (c) Ψ_{med}, and (d) Ψ_{max}, calculated 30 days after injection. Results show that the pore pressure exceeds the injection pressure for a porosity reduction rate of (c) Ψ_{med} and (d) Ψ_{max}. Furthermore, results clearly show that overpressure depends on the initial porosity reduction rate and not the newly found porosity, because although the matrix porosity in Figures 3.20(c-d) reaches the critical value, the pore pressure is higher for the fastest porosity reduction rate. An abrupt loss of porosity forces the system to accommodate a pore pressure buildup, leading overtime to overpressure. That is, the fluid pressure in the fractured system exceeds that of the injection well, thus generating a reversed Darcy flow and a faster loss of temperature. For clarity, a reversed Darcy flow is the Darcy flow in reversed direction, contrary to what is to be expected at an injection well. Consequently, one must investigate the repercussions on the evolution of fracture width due to these additional thermoelastic effects. We consider the fracture has a constant porosity of one [1] but undergoes fracture aperture, therefore permeability, variation with an initial width b=2x10^{-4}[m].

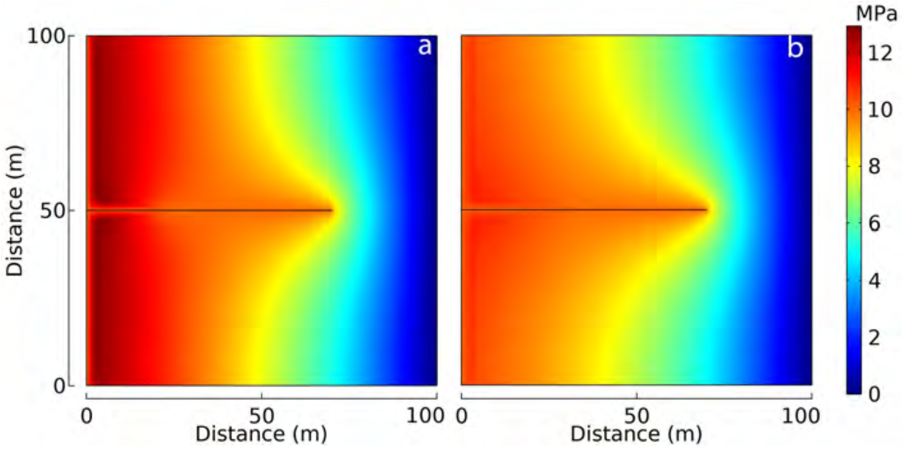

FIGURE 3.22: Pore pressure assuming a maximum porosity reduction rate Ψ_{max}, (a) 100 days and (b) 365 days after injection.

Figure 3.22 shows an end-case scenario of pore pressure, assuming Ψ_{max}, (a) 100 days and (b) 365 days after injection. Note that porosity reduction rate decreases and stabilizes at this point, and the porosity reaches the critical value. Results clearly show that overpressure is still present in the system after a year of injection.

Figure 3.23 shows the effective silica (as quartz) concentration assuming constant porosity (cp), (a) 30 days after injection and (c) a year after injection, and assuming Ψ_{max}, (b) 30 days after injection and (d) a year after injection. Results indicate a decrease in effective silica concentration in the presence of a porosity reduction rate, by comparing Figures 3.23(a-b), 30 days after injection, and Figures 3.23(c-d), after 1 year of injection. The reduction is observable at the fracture-matrix interface and the vicinity of the well due to the decrease in the pore space that can accommodate more depositing silica. Furthermore, a reversed Darcy flow also means that silica may be transported backwards towards the well, inducing lower injectivity. Note that we consider the advection term for both the matrix and the fracture.

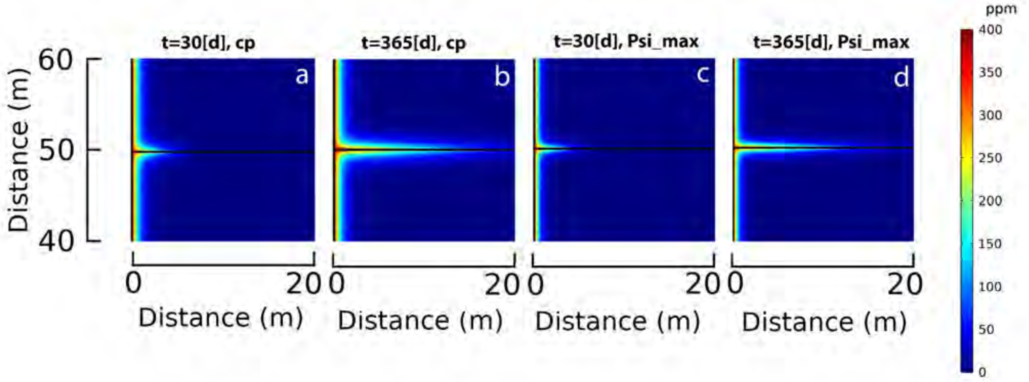

FIGURE 3.23: Concentration of silica (as quartz) 30 days after injection, assuming (a) constant porosity (cp) and (b) Ψ_{max}, and a year after injection, assuming (c) constant porosity (cp) and (d) Ψ_{max}.

We proceed to examine the temperature, shown in Figure 3.24, assuming (a-b-c-d) constant porosity, and Ψ_{max} (e-f-g-h), presented consecutively for 10 days, 30 days, 100 days and 365 days after injection.

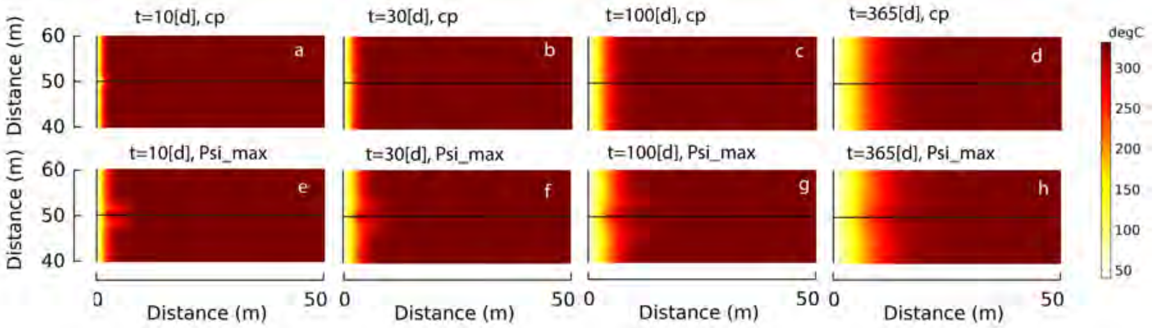

FIGURE 3.24: Temperature 10, 30, 100, and 365 days after injection, assuming (a-b-c-d) constant porosity, and (e-f-g-h) Ψ_{max}.

Results in Figure 3.24(e-f-g-h), clearly show the effects of the reversed Darcy flow induced by fast porosity reduction rates on the temperature front. First, a larger cooling front propagates at the vicinity of the well, because of the reversed Darcy flow; temperature flows from the matrix to the well. Second, a larger cooling front extends further along the fracture-matrix interface because of the leakoff. Results are pronounced at the fracture-matrix interface and at the vicinity of the well, where the shape of the temperature front along the fracture-matrix interface clearly takes a '<' shape, indicating a reverse flow. As the porosity reduction rate stabilizes and pore pressure slowly reaches steady state, the effects of the reversed Darcy flow should slowly diminish.

Figure 3.25 shows fracture width evolution for different porosity reduction rates, assuming an initial fracture aperture of (a) 0.02[m] and (b) 0.005[m]. Figure 3.25(a) shows that fracture width decreases faster for higher porosity reduction rate, specifically at early times 10 days and 30 days, showing the dominant effect of silica deposition. However, after 365 days the fracture width is largest for the highest porosity reduction rate Ψ_{max} due to the effects of the reversed Darcy flow and the subsequent faster cooling front. After a year of injection and considering Ψ_{max}, fracture is 0.4[mm] (8%) larger for w_0=0.005[m] (Figure 3.25(a)), and 2.2[mm] (11%) larger for w_0=0.02 [m] (Figure 3.25(b)), measured at 20[m]. This observation is due to the loss of heat as the fluid flows from the hot reservoir back to the injection well caused by the reversed Darcy flow, in the presence of Ψ_{max}. That is, an increased displacement of the fracture takes place, thus increasing its likelihood of failure. Furthermore, a larger initial fracture aperture results in a larger fracture width increase due to higher thermoelastic effects.

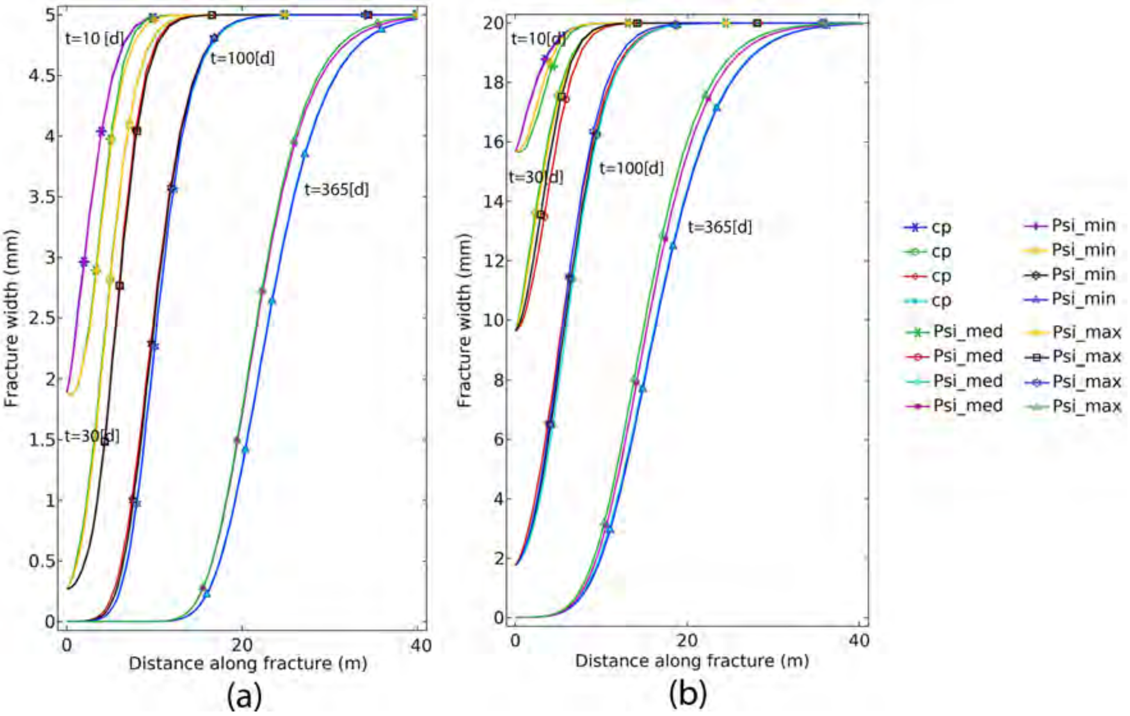

(a) (b)

FIGURE 3.25: Evolution of the fracture width after 10 days, 30 days, 100 days and 365 days of injection, assuming (a) w_0=0.005 [m] and (b) w_0=0.02 [m].

Figure 3.26 shows (a) pressure and (b) temperature along the fracture 10 days after injection, assuming different porosity reduction rates and for two values of initial fracture width w_0=0.005[m] and w_0=0.02[m]. Figure 3.26(a) shows that the overpressure due to maximum porosity reduction rate is larger for smaller initial fracture aperture, 22[MPa] for w_0=0.005[m] in comparison to 21[MPa] for w_0=0.02[m], hence the system displays a larger reversed Darcy flow in the presence of a smaller initial fracture width. The effects of this larger reversed Darcy flow can be seen in Figure 3.26(b), where temperature is smallest assuming Ψ_{max} and w_0=0.005[m].

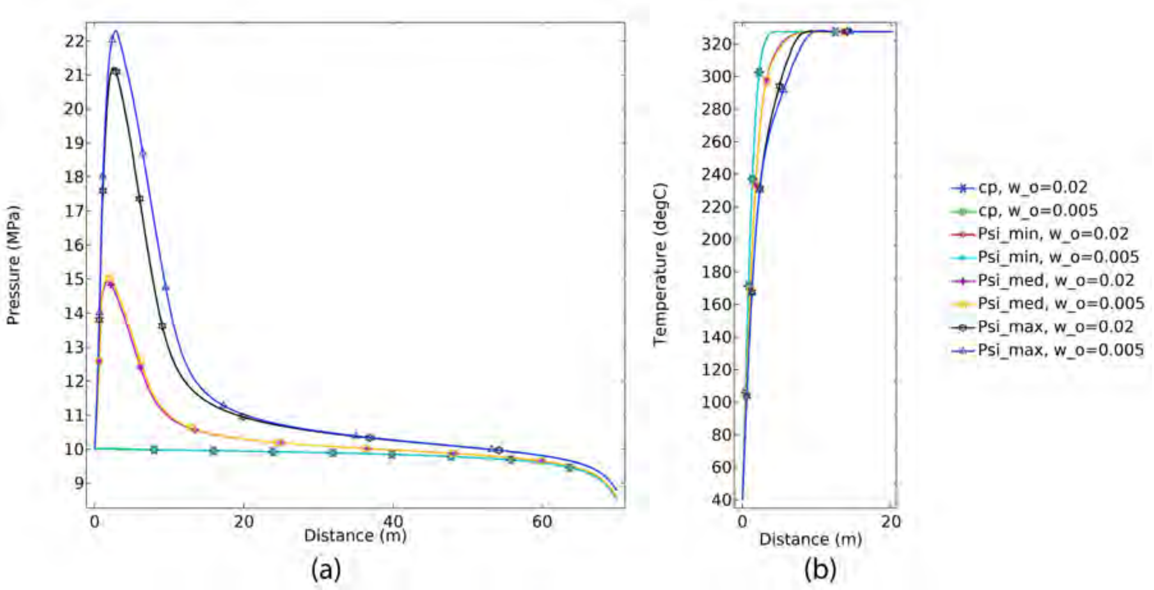

FIGURE 3.26: Evolution of the (a) pressure and (b) temperature along the fracture 10 days after injection, assuming different porosity reduction rates and for two values of initial fracture width w_0=0.005 [m] and w_0=0.02 [m].

Next, we investigate the effects of silica deposition in a pre-existing fracture and source at its center, as shown in Figure 3.3, using SPARROW. Assuming a constant pressure, temperature and silica concentration at the fracture center, we model the pressure, temperature and concentration components in the fracture-matrix system undergoing porosity and permeability changes. Figure 3.27 shows fluid pressure after 5 days, 30 days and 100 days of injection,respectively, assuming a porosity reduction rate of (a) Ψ_{min} , (b) Ψ_{med}, and (c) Ψ_{max}.

Overpressure occurs in all three scenarios of porosity reduction, and is 20% assuming Ψ_{med} (Figure 3.27 [1](b)) and 80% assuming Ψ_{max} (Figure 3.27[1](c)). This sudden pore pressure jump is governed by the porosity reduction rate and not the newly calculated porosity, as can be seen in Figure 3.28, where for the same critical porosity of 0.05, overpressure is 11% assuming Ψ_{med} (Figure 3.27[2](b)) and 40% assuming Ψ_{max} (Figure 3.27[2](c)). While the overpressure slowly reaches 0% for the case of Ψ_{min} (Figure 3.27[3](a)), it is still present after a year of injection, for the cases of Ψ_{med} (10%) and Ψ_{max} (13%) as seen in Figures 3.27[3](b) and [3](c), respectively. Furthermore, this surge in pore pressure is clustered at the vicinity of the injection point because of the largest silica deposition and hence porosity reduction.

Figure 3.28 shows the calculated [1] porosity and the corresponding [2] pore pressure a year after

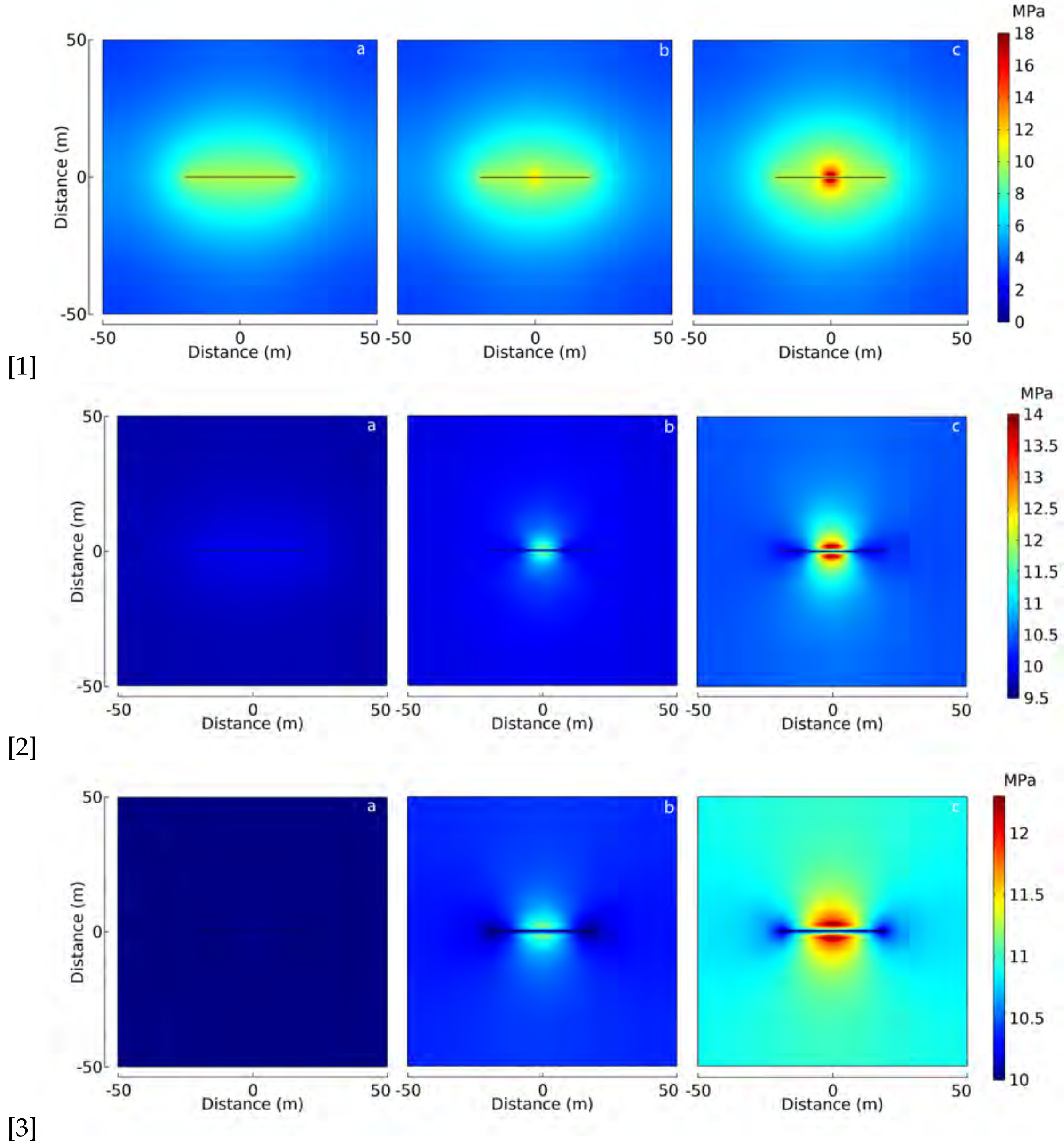

FIGURE 3.27: Pore pressure after [1] 5 days, [2] 30 days, and [3] 100 days of injection, assuming (a) Ψ_{min}, (b) Ψ_{med}, and (C) Ψ_{max}.

injection at the vicinity of the fracture, assuming a porosity reduction rate of (a) Ψ_{min}, (a) Ψ_{med}, and (c) Ψ_{max}. Results show that the excess pore pressure dissipates from the fracture for all cases, and reaches the boundaries, mostly due to the no flow condition, specifically for the Ψ_{med} (10%) and Ψ_{max} (16%) case, shown in Figure 3.28[2] (b), and (c),respectively. The resulting overpressure affects the advection term, the concentration of silica (Figure 3.29), and the temperature evolution (Figure 3.30). Figure 3.29 shows the silica concentration [1] 30 days and [2] 365 days of injection with (a) constant porosity, and (b) Ψ_{max}.

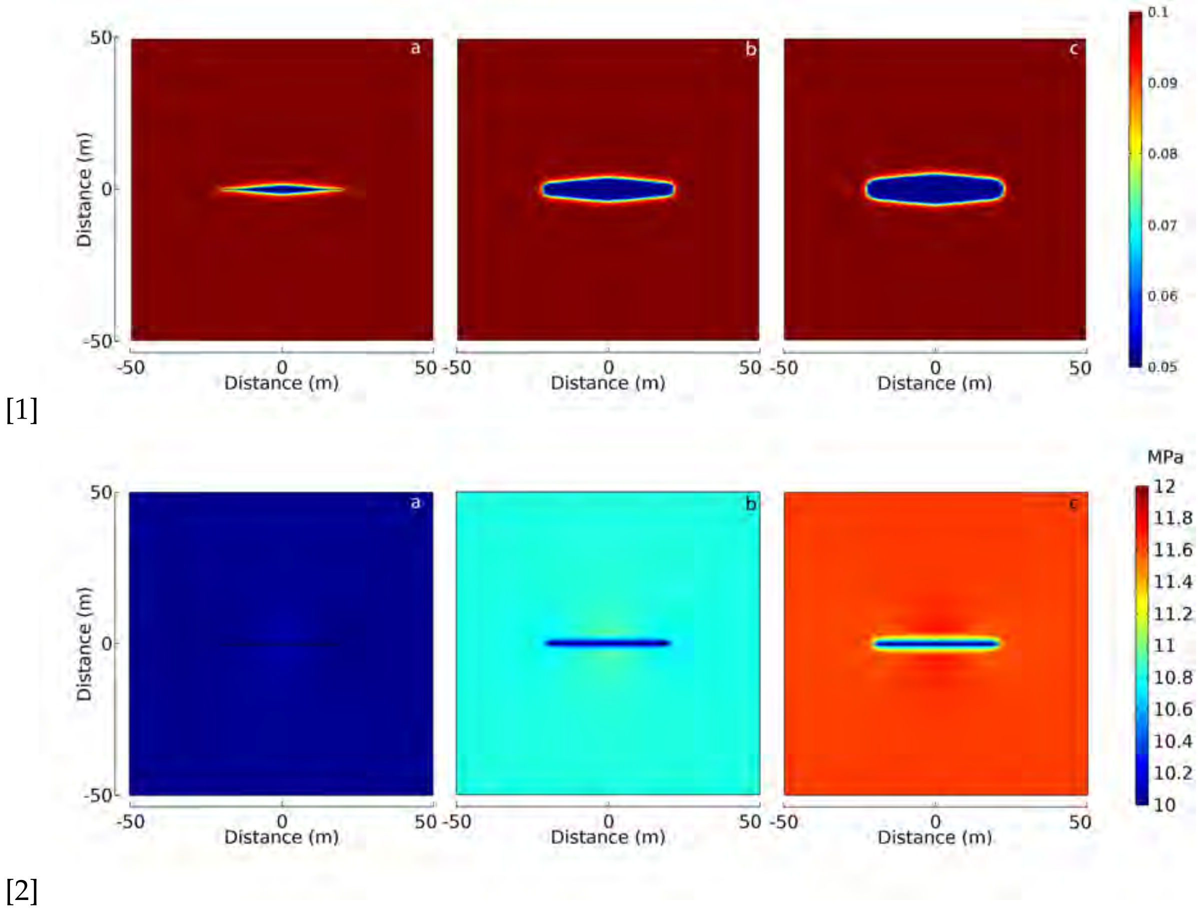

FIGURE 3.28: [1] Porosity and [2] pore pressure after 365 days, assuming (a) Ψ_{min}, (b) Ψ_{med}, and (C) Ψ_{max}.

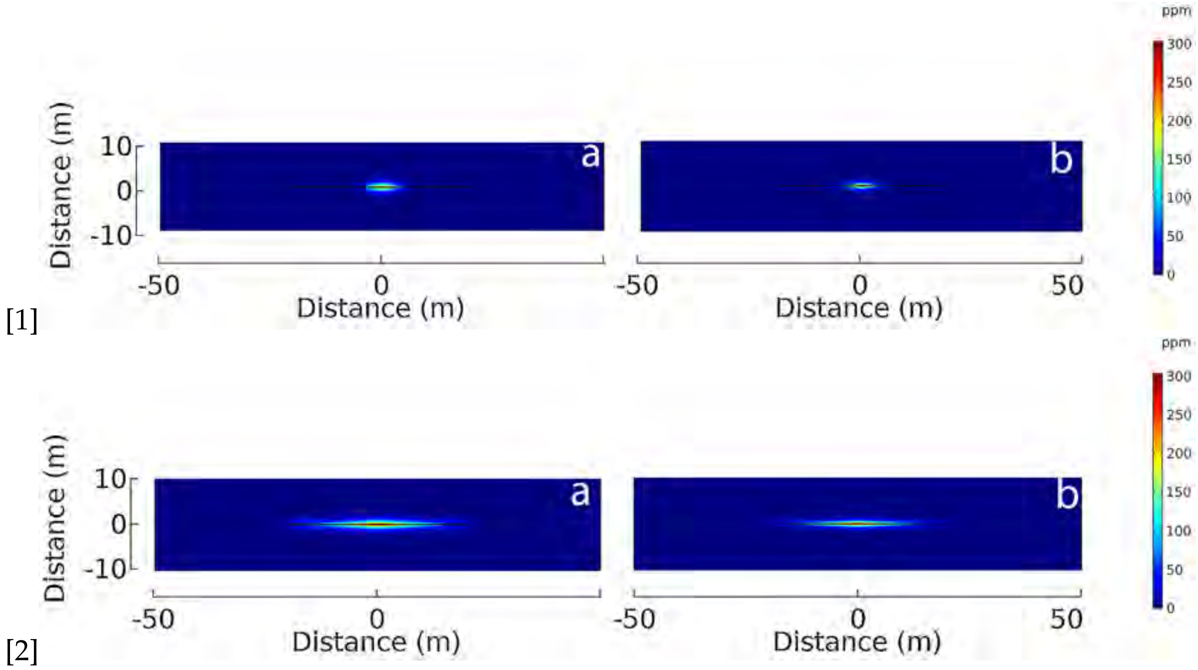

FIGURE 3.29: Effective silica concentration after [1] 30 days and [2] 365 days of injection, assuming (a) constant porosity (cp), and (b) Ψ_{max}.

One clearly sees the decrease in the concentration of deposited silica at the center of the fracture due to the decrease of the pore space in that region. Although not shown, once the system reaches the critical porosity and the porosity reduction rate nears zero, the concentration of deposited silica reaches a plateau and does not vary for example between 100 days and 365 days. Finally, Figure 3.30 shows temperature evolution after [1] 5 days, [2] 30 days, [3] 100 days, and [4] 365 days of injection assuming (a) constant porosity, (b) Ψ_{med}, and (c) Ψ_{max}. Results show that the thermal cooling front due to the cold fluid injection becomes more pronounced in the presence of abrupt loss in porosity, as seen for the case of (c) Ψ_{max}, at all times. This is due to the negative pressure gradient, that transports the temperature from the surrounding rock towards the injection source, leading to a larger zone of decreased temperature around the fracture. These results are important because they show that porosity reduction affects the value and propagation radius of the thermal stresses acting along the fracture-matrix interface.

Finally, we examine the implications on rock-fracture stability by evaluating the failure potential of the rock due to silica rich-pore clogging injection fluid. We assume a combination of SPARROW and the simple Mohr-Coulomb (MC) failure condition for a point in a cohesionless and frictional rock with a friction failure slope μ of 0.6. We assume that the rock fails when $\tau - \mu\sigma_n^{'} > 0$, where τ is the shear stress [MPa], and $\sigma_n^{'}$ is the effective normal stress [MPa]. We consider a maximum horizontal stress σ_1 of 45[MPa] and σ_3 of 20[MPa], respectively. Figure 3.31 shows the Mohr-Coulomb failure criterion for constant porosity, Ψ_{med}, and Ψ_{max} calculated 5 days after injection. To further detail the results, Figure 3.32 shows that assuming only pore pressure, only fractures with an inclination range of 55°-65° are susceptible to slip. However, other inclinations fulfill the failure requirement when introducing the porosity reduction rate. The excess pore pressure, e.g. in excess of hydrostatic, allows inclinations of 45°-75°to slip in the case of Ψ_{med}, and all other inclinations 35°-85°to slip in the end case scenario of Ψ_{max}. Figure 3.33 displays the values of effective normal stress on a fracture with an inclination of 65°, assuming (a) constant porosity, (b) Ψ_{med}, and (c) Ψ_{max}. Neglecting the fracture aperture evolution of the inclined fracture, and based on the result that the excess pore pressure is 80% larger than the pore pressure, the effective stress at the center of the fracture (Figure 3.33(a)) is almost half of the one calculated assuming Ψ_{max} (Figure 3.33(c)).

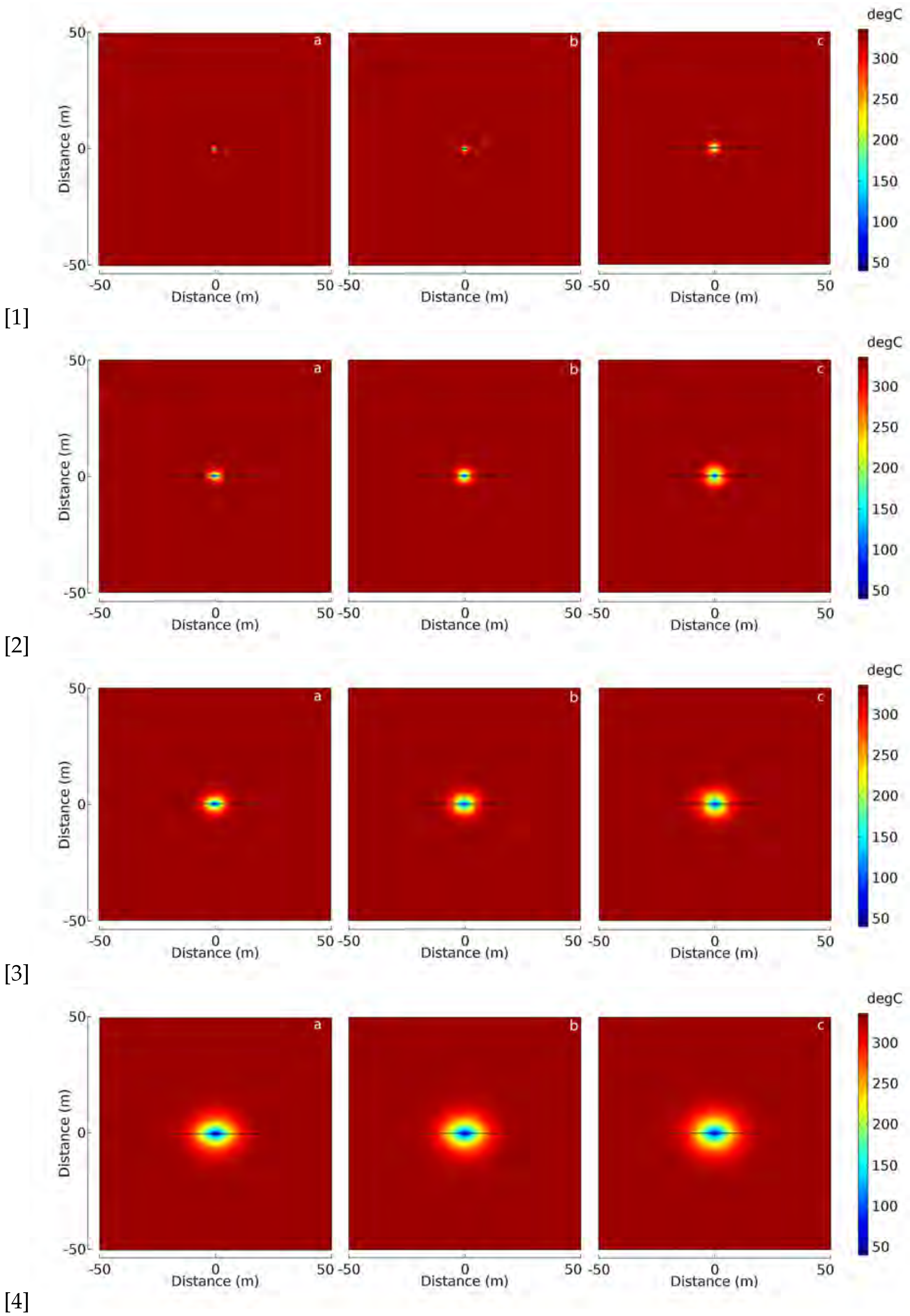

FIGURE 3.30: Temperature evolution after [1] 5 days, [2] 30 days, [3] 100 days, and [4] 365 days of injection, assuming (a) constant porosity, (b) Ψ_{med}, and (c) Ψ_{max}.

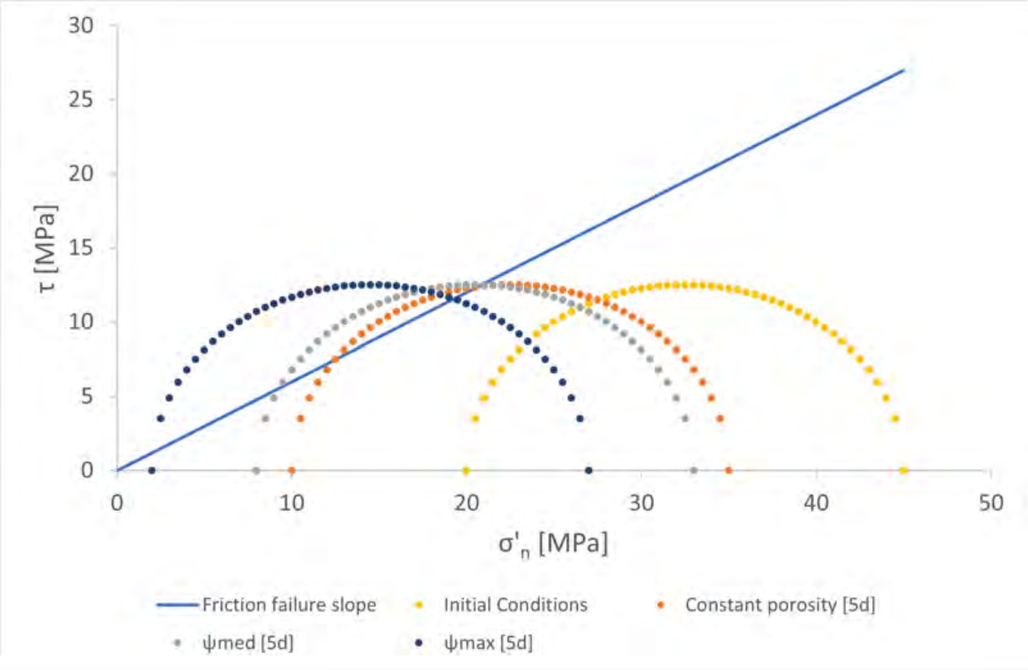

FIGURE 3.31: Mohr's circle assuming a cohesionless frictional rock with a friction failure slope μ of 0.6. We presume a maximum horizontal stress σ_1 of 45[MPa] and σ_3 of 20[MPa] respectively, each acting in the far field. We present the effective normal and shear stresses acting on the rock assuming the initial conditions, constant porosity and a porosity reduction rates Ψ_{med}, and Ψ_{max}, calculated 5 days after injection.

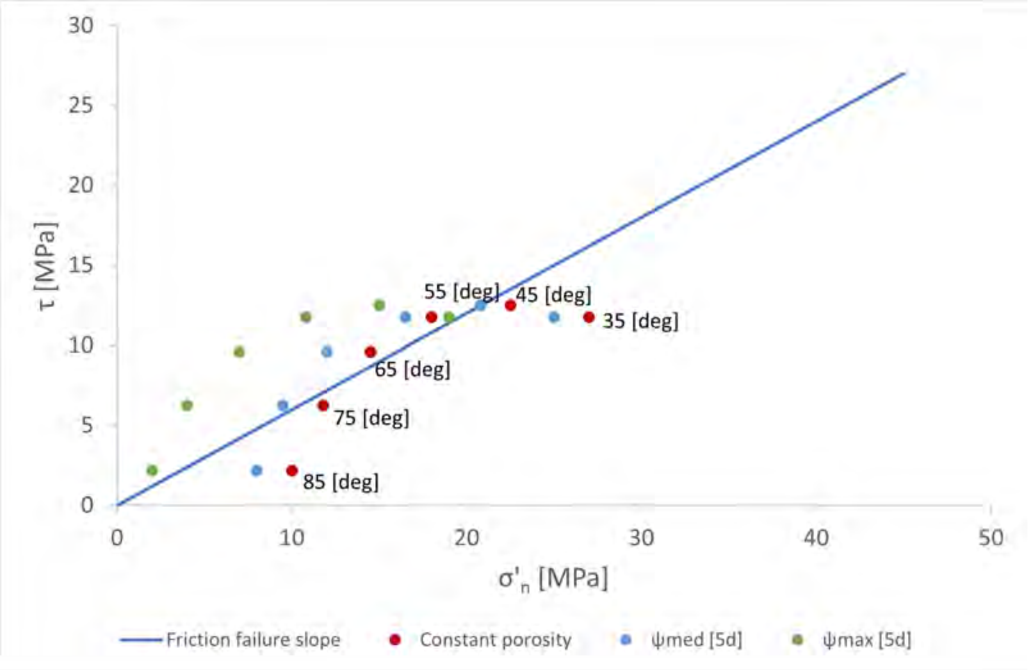

FIGURE 3.32: Failure study of a fracture for angle ranges (35,85) (notation above red dots), assuming a cohesionless rock with a friction failure slope μ of 0.6. We presume a maximum horizontal stress σ_1 of 45[MPa] and σ_3 of 20[MPa] respectively, each acting in the far field. The plot displays effective normal and shear stresses acting on the rock, assuming constant porosity and porosity reduction rates of Ψ_{med} and Ψ_{max}.

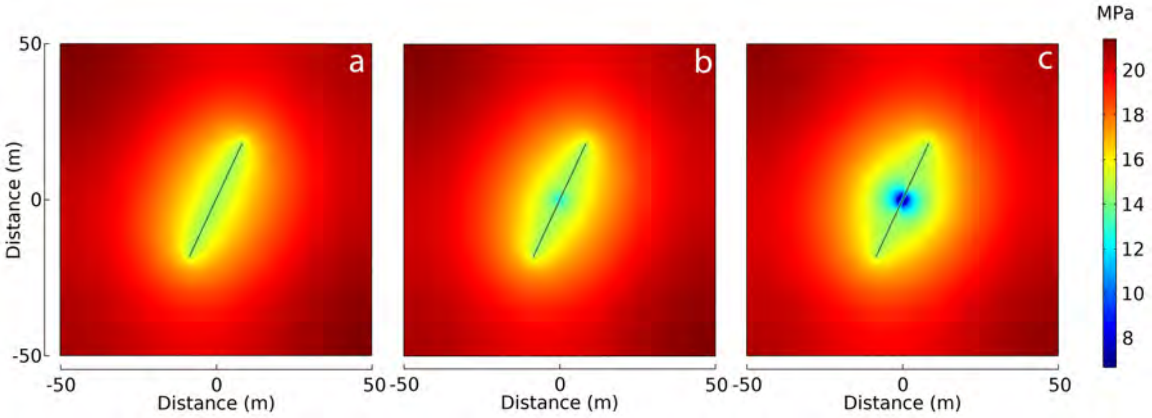

FIGURE 3.33: Effective normal stress after 5 days of injection, assuming a 65°inclination angle of the fracture, and (a) constant porosity, (b) Ψ_{med}, (c) Ψ_{max}

3.5 Conclusions

We numerically investigate the influence of a time-dependent porosity reduction mechanism on the evolution of pressure, temperature, and silica concentration in fractured geothermal systems. This is relevant to under-performing doublets because silica deposition lowers injectivity by clogging the vicinity around fractures. Results capture the dynamic interaction between the porosity reduction rate and the excess pore pressure, sufficient to reversed Darcy flow, with concomitant effects of advancing the thermal front and fracture aperture evolution in the system. The model shows that when neglecting porosity reduction, one can underestimate the thermal stresses acting on the fracture-matrix interface and, consequently, the fracture aperture. Results also show that fracture aperture is initially larger for smaller porosity reduction rates. However, at larger times, the fracture aperture becomes the largest for the highest porosity reduction rate due to the excess temperature decrease driven by the reversed Darcy flow. Furthermore, results show the influence of the porosity reduction rate on the stability of the rock, as it shifts the Mohr-circle further towards failure. Although the stability of the fracture depends highly on its orientation, we show that porosity reduction can lead to fracture failure even for highly mis-oriented faults relative to the principle stresses. Therefore, one can underestimate the effective stresses when neglecting porosity reduction and develop misleading conclusions surrounding the stability of the rock. This numerical model, SPARROW, can be used to study multiple mineral precipitations including Calcite, Feldspar, Illite etc., in conjunction with their respective kinetics. The coupling between the mechanical processes and SPARROW are subjects of current research.

Chapter 4

Subduction zone episodic tremor and slip due to silica enrichment: the big picture

4.1 Abstract

Fluids derived from progressive dehydration and melting reactions of the downgoing slab are instrumental in subduction zone episodic tremor and slip (ETS). The excess pressure generated from these slab-derived fluids introduce a change in the porosity/permeability structure of the rock by inducing hydrofractures. In addition, dissolved silica is transported by these rising fluids and deposits primarily downdip (near the base of the forearc crust) because of the high temperature dependence of silica solubility, leading to porosity and permeability reduction in the rock. When porosity reduction due to silica deposition (as quartz) is significant enough to drive the system in overpressure, the excess pressure results in low effective fault-normal stress, thus triggering reoccurring slow slip events. We introduce a two-dimensional numerical example using COMSOL Multiphysics to model pore pressure development in Cascadia subduction zone undergoing silica enrichment from quartz-saturated fluids generated from dehydration and melting processes. Results show that fracture or fault reactivation potential is a local problem and is controlled primarily by a time-dependent porosity reduction rate. The numerical model calculates the pore pressure in excess of hydrostatic and the resulting reduced effective stresses. The localised slip event alters the porosity-permeability of the system and its occurrence timescale is in agreement with the behavior of observed V_p/V_s forearc values measured in northern Cascadia.

4.2 Introduction

Episodic tremor and slip (ETS) involves repeated slow slip of faults accompanied by low-frequency tremor taking place at the boundaries of plate interface-within the forearc of young and warm subduction zones, downdip of the locked zone (Audet and Bürgmann, 2014; Schwartz and Rokosky, 2007; Beroza and Ide, 2011). Several authors have proposed that ETS is a fluid driven process resulting from dehydration reactions in the subducting plate, more specifically dehydration of serpentine; a mineral comprised of hydrated magnesium and silicate. Serpentization occurs through hydrothermal alteration of Basalts at the mid-ocean ridge. As pressure and temperature rise, serpentine dehydrates, thus releasing water that flows within the crust and upper mantle (Peacock, 2009; Miller et al., 2003). The degree of serpentinization depends on the age of the slab and the availability of fluids from slab dehydration, which in turn depends on the age of the subduction zone. A young and warm slab will show more serpentinization than an old and cold slab, because the younger one will release more of his bound H_2O in he forearc, whereas the older one will retain most of his H_2O until farther landward (Wada et al., 2008).

Silica deposition from a silica saturated rising fluid in a geothermal system may lead to the development of a low permeability cap zone in the near surface, as seen in Te Kopia geothermal field (situated near the southern termination of the Paeroa fault, which bounds the eastern margin of the Taupo fault belt) (Dempsey et al., 2012). The geometry of this formed cap zone allows thermal dilution as it allows heat to spread across a larger area and concomitantly insulates the fluids below it, thus increasing the reservoir fluid temperature, enthalpy and the geothermal potential of the reservoir. Furthermore, (Dempsey et al., 2012) suggests using a numerical model based on the hypothesis that silica deposition in hydrothermal systems promotes fault rupture and reactivation. Particularly, the author states that sealing of fault aperture due to silica depositing leads to overpressure and a consequent decrease in the effective normal stress acting on the fault boundary, thus triggering fault reactivation. As a result, fracture permeability increases, leading to higher fluid flow rate and more precipitation on the surface, leading to further hydrofracturing (Dempsey et al., 2012). Furthermore, experimental results from (Giger et al., 2007) show that porosity evolution is highly time-dependent and porosity reduction rate increases with increasing temperature being as high as 6x10^-5s^{-1} at $700°C$ and 7.4 x 10^-4 s^{-1} at $850°C$, assuming fine-grained quartz aggregates subjected to hot pressing experiments, with confining pressure of 250[MPa] and pore pressure of 150[MPa].

Furthermore, tests run on the quartz micro-structure prove that permeability reduction was controlled by dissolution-precipitation creep processes. Results also suggest that quartz rich fault zones can evolve from high permeability conduits to low permeability seals within the recurrence time of major earthquakes (Giger et al., 2007). Reoccurring earthquakes can also indicate the presence of economic-grade gold deposits (Weatherley and Henley, 2013). In this publication, the authors suggest that earthquake rupture and aftershock cycles lead to changes in fluid pressures which consequently triggers flash evaporation. Such extreme changes in pressure transients also indicate changes in temperature, density and compressibility of the fluid in theses seismically active faults (for example in western Australia) (Weatherley and Henley, 2013). Flash evaporation prompt co-deposition of silica and trace elements hence forming gold enriched quartz veins.

The overpressure, also defined as pore pressure in excess of hydrostatic, is introduced by the released fluids from dehydration processes causing the effective fault normal stresses to decrease. Accordingly, this pore pressure development triggers hydro fractures, fault weakening and brittle failure (Miller et al., 2003; Raleigh and Paterson, 1965). These slow earthquakes are further enabled by the deposition of quartz transported by these rising fluids, rich in dissolved silica. Quartz deposits primarily downdip because of the high temperature dependency of silica solubility (Audet and Bürgmann, 2014), and is confirmed by the low Poisson's ratio values measured using seismic tomography velocities of the base of the forearc lower crust (Ramachandran and Hyndman, 2012). High temperature enables progressive quartz deposition, thus decreasing the porosity-permeability structure of the rock and triggering overpressure (Audet and Bürgmann, 2014). Their study focuses on ETS detected at the northern Cascadia and Japan subduction zones, described as warm subduction zones because of the young incoming lithosphere (<20[Ma]) and modest plate convergence rates (40-60[mm/a]) (Peacock, 2009). In these warm subduction zones, dehydration processes take place at a shallower depth than cool subduction zones, where dehydration processes are predicted at depths of 100 [km] or more (Peacock, 2009; Ramachandran and Hyndman, 2012). Other factors, contribute to the nature and recurrence of ETS such as slab morphology (Audet et al., 2010) and crustal age (Audet and Schwartz, 2013). In a separate article, (Audet et al., 2009) suggests a direct correlation between regular ETS recurrence time intervals and steady state fluid pressure buildup from dehydration processes of the subducting slab. The released rising fluid causes precipitation sealing of the plate boundary which is also related to ETS recurrence time intervals.

In this chapter, we investigate porosity reduction due to silica enrichment as proposed by (Audet and Bürgmann, 2014) and report the results of a 2D numerical model. The model predicts the evolution of the effective normal stress assuming a time dependent reduction in porosity, thus predicting ETS and its occurrence time. We model pore pressure development due to silica enrichment from rising fluids in Northern Cascadia subduction zone. We focus the study on the mantle wedge because it is believed that silica deposition occurs from these silica-rich rising fluids and not the presence of quartz rich rocks. We present a 2D numerical model using COMSOL Multiphysics to calculate the excess pore pressure and resulting effective stress drop. Results show that a large-scale silica or mineral deposition event is not likely to trigger ETS, rather local pore pressure increases are the cause, as previously proposed by (Walder and Nur, 1984).In fact, Miller and Nur, 2000 propose permeability as a toggle switch in fluid-controlled crustal processes and explain that the local permeability can switch simultaneously from one extreme to an other. That is, high permeability in the form of dikes, faults and cracks and impermeable in the form of tight crystalline rocks and impermeable fault gauge/seals. The toggle switch assumption suggests that in order to model pore pressure behavior and its consequences on the system, one cannot simply assume a homogeneous permeability throughout the reservoir rock as it fails to represent the real fluid-controlled processes that are described in (Miller and Nur, 2000). A better and more realistic approach is to assume a local permeability that evolves based on the transient thermo-hydro-chemical-mechanical processes. In our proposed model, the evolution of the local permeability is calculated from the evolution of the local porosity due to silica precipitation in the system. We study a REV (representative elementary volume) of the subduction zone model to really focus on the local evolution of pore pressure and how it affects on the mechanical response (local) of the fault.

Furthermore, results suggest that excess pore pressure from silica deposition may be possible assuming a time dependent porosity reduction rate which varies depending on the concentration of deposited silica. It is believed that silica deposits quickly, and hence porosity and permeability suffer a severe decrease in the mantle wedge when immediately exposed to those rising fluids, rather than the assumption that the fluid deposits at a low steady state rate. However, faults reactivate and then heal in an incessant cycle, so consequently the fault is subjected to slower changes in effective stress; that is a lower recurrence times of episodic tremors and slip (ETS).

4.3 Conceptual model

Porosity reduction due to silica deposition from dehydrating rising fluids is studied in order to better understand fault failure potential and the consequent seismic tremor. In these low permeability, low porosity systems, fluid diffusion in the subducting slab is an extremely slow process, on the order of thousands to million of years (Audet and Bürgmann, 2014; Lee and Kim, 2021; Walder and Nur, 1984). An intuitive approach to numerically visualize the effect of porosity reduction on pore pressure development is to numerically model a representative elementary volume (REV) of the problem. We model a fault and the surrounding low permeability/low porosity rock as shown in Figure 4.1, over a 100[m] x 100[m] 2D block and apply the governing equations defined in Chapter 3. This approach to modeling fluid flow in the subduction zone was adopted from previous workKoerner, Kissling, and Miller, 2004 and shown in Figure 4.2.

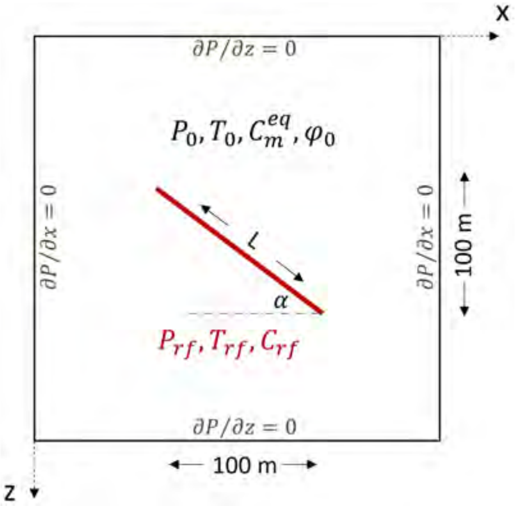

FIGURE 4.1: Conceptual model of the problem. P, T, C and ϕ are the pressure, temperature, silica concentration and porosity, respectively. subscripts 0, r and f represent initial, rock and fracture conditions, respectively. L is the length of the fracture, set to 70 [m], α is the fracture inclination angle, set to 45°. Superscript eq represents equilibrium. We also assume no flow and insulated boundary conditions.

We consider a fracture with a 45° inclination angle α and calculate fluid pressure, temperature, silica deposition and the effective stress acting on the fault/fracture boundary assuming a temporal evolution of porosity and permeability. Knowing the effective stress permits the study of fault stability and its tendency to failure/reactivation. Figure 4.1 presents the conceptual model of the problem, clearly defining the simplified geometry, the initial conditions (with the subscript 0), and boundary conditions (subscript f is for fracture and r is for rock). We assume no flow and insulated boundary conditions. Table 4.1 lists on the rock properties used for the numerical model, that differ with those used in Chapter 3. We assume that the silica-rich rising fluid from the dehydration process

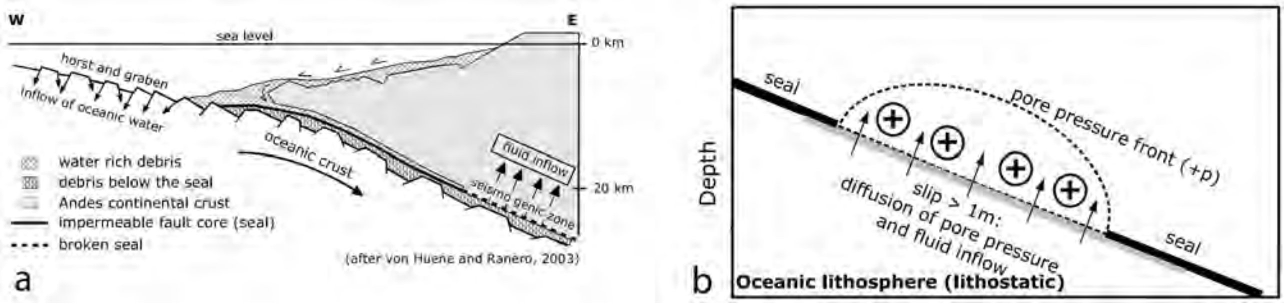

FIGURE 4.2: (a) Conceptual model based on the work of Huene and Ranero (2003), (b) cartoon of the pressure diffusion conditions along the lithostatic mantle or the seal (modified from Koerner, Kissling, and Miller, 2004)

introduces a pore pressure difference of 20[MPa] and a temperature difference of 30[$^\circ C$] into the rock system (Walder and Nur, 1984).

TABLE 4.1: Rock properties for the THC model.

Initial porosity of the rock, ϕ_o	0.04
Initial matrix permeability, k_o	10^{-22} m^2
Initial reservoir temperature, T_o	300 °C

4.4 Numerical model

We numerically investigate the effects of porosity reduction on pore pressure development in a representative region of the subducting plate using COMSOL multiphysics. We evaluate porosity and permeability evolution, pressure and temperature variations and the resulting effective normal stress applied on the fracture/fault boundary. Figure 4.3(a) shows the geometry representing the subduction zone and its components: (1) mantle wedge, (2) overlying continental crust, and the subducting slab comprised of (3) lithospheric mantle and (4)crust. Figure 4.3(b) shows the chosen mesh distribution for the problem; triangular meshing assumed fine in the overlying continental crust (region 2) and the lithospheric mantle (region 4), and extremely fine in the mantle wedge (region 1) and the subducting slab crust (region 3) because of their importance in fluid flow. Lee, Seoung, and Cerpa (2021) suggest that flow from rising fluids is concentrated at regions 1 and 3 because of the pressure and extremely favorable high temperatures.

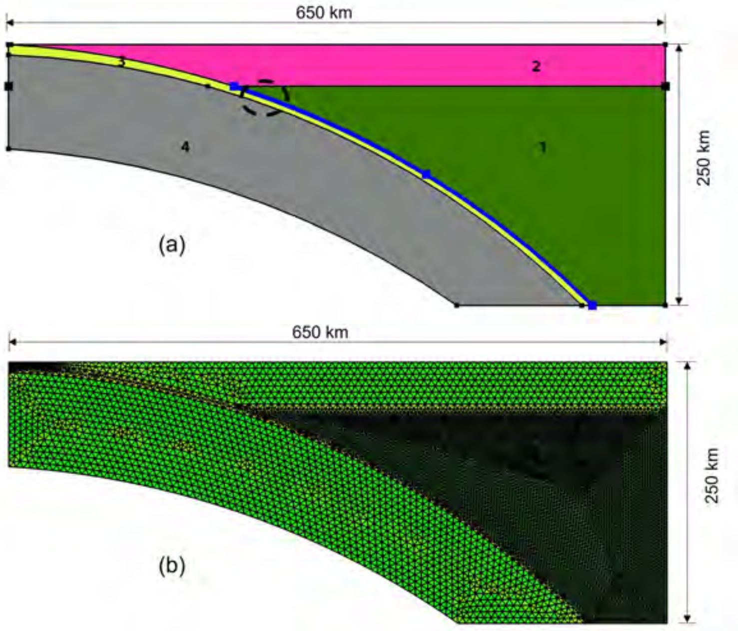

FIGURE 4.3: Geometry and mesh implemented in COMSOL multiphysics to model pore pressure development in the mantle wedge. a) The blue highlighted zone is the region at which ETS is triggered. The subduction zone is represented by 4 regions: (1) the mantle wedge, (2) the overlying continental crust, (3) is the crust and (4) is the lithospheric mantle. Slip is assumed in the bottom half of the blue curve on the edge. Figure b) shows mesh distribution consisting of triangular elements with finer distribution inside the mantle wedge (region 1) and the slab crust (region3).

4.5 Results and discussion

Pressure from dehydrating fluids is confined in the mantle wedge and the lithospheric mantle, and precipitation of silica in those regions increases the likelihood of porosity reduction and pore pressure build up. Figure 4.4 shows pore pressure buildup after 180 days of dehydration process assuming a constant porosity reduction rate. We choose a length of 180 days of simulation to portray the assumption made by Audet and Bürgmann, 2014, that possible episodic tremor and slip (ETS) result from pressure buildup due to silica enrichment.

As it can be seen the pore pressure gradient is difficult to visualize because of the low permeability/porosity in the system. Pore pressure diffusion clearly takes infinite time to be detected at a large scale because of the low permeability of this high enthalpy system (Figure 4.4). Even assuming a constant porosity reduction rate of $5x10^{-}16[s^{-1}]$ and impermeable boundary conditions, it is almost impossible to determine any pore pressure development in excess of hydrostatic. For this reason, we opt to represent the system at a smaller scale; a representative elementary volume (REV). We portray the blue highlighted line along the litospheric mantle as an element volume and model the pore pressure assuming porosity reduction due to silica enrichment. This assumption was already

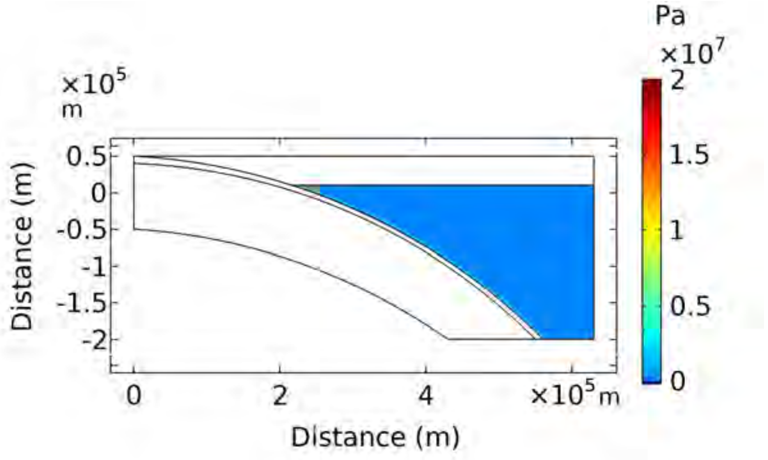

FIGURE 4.4: Pressure after 180 days of silica deposition assuming no flow boundary conditions and a constant porosity reduction rate of $5.10^{-}16[s^{-1}]$ showing that pore pressure diffusion is too slow to be visualized.

applied by Koerner, Kissling, and Miller (2004), who model fluid flow in the deep crust by assuming a simplified geometry, as seen in Figure 4.2(b).

Figure 4.5 shows the (a) porosity reduction rate, (b) permeability and (c) fracture/fault aperture evolution set for this problem. The chosen porosity reduction rate is time dependent because it implicitly depends on the concentration of silica depositing from the rising silica-rich fluids. Furthermore, rising fluid pressure and temperature conditions are assumed at the center of the fault or fracture.

Figure 4.6 shows pore pressure development around the fracture assuming constant porosity after 10 days, 30 days and 180 days of simulating rising fluids. Figure 4.7 shows pore pressure development around the fracture assuming a time-dependent porosity reduction rate provided in Figure 4.5. Pore pressure development is pronounced at the fault/fracture boundary reaches a value of 50[MPa], which is almost 3 times larger than the introduced pore pressure difference of 20[MPa] Walder and Nur, 1984 by the rising fluids, 180 days after silica rich fluids are introduced in the system via dehydration processes. Fracture aperture exponentially decreases with the imposed porosity reduction rate.

Figure 4.8 shows temperature distribution at the vicinity of the fault/fracture. Based on the results shown in Chapter 3, temperature cooling will occur faster because of the negative Darcy flow and propagate farther. However, in this low permeability reservoir and the small temperature difference between the rising fluid temperature and the rock temperature, results show no significant difference in the radius of temperature reduction propagation at the vicinity of the fracture/fault.

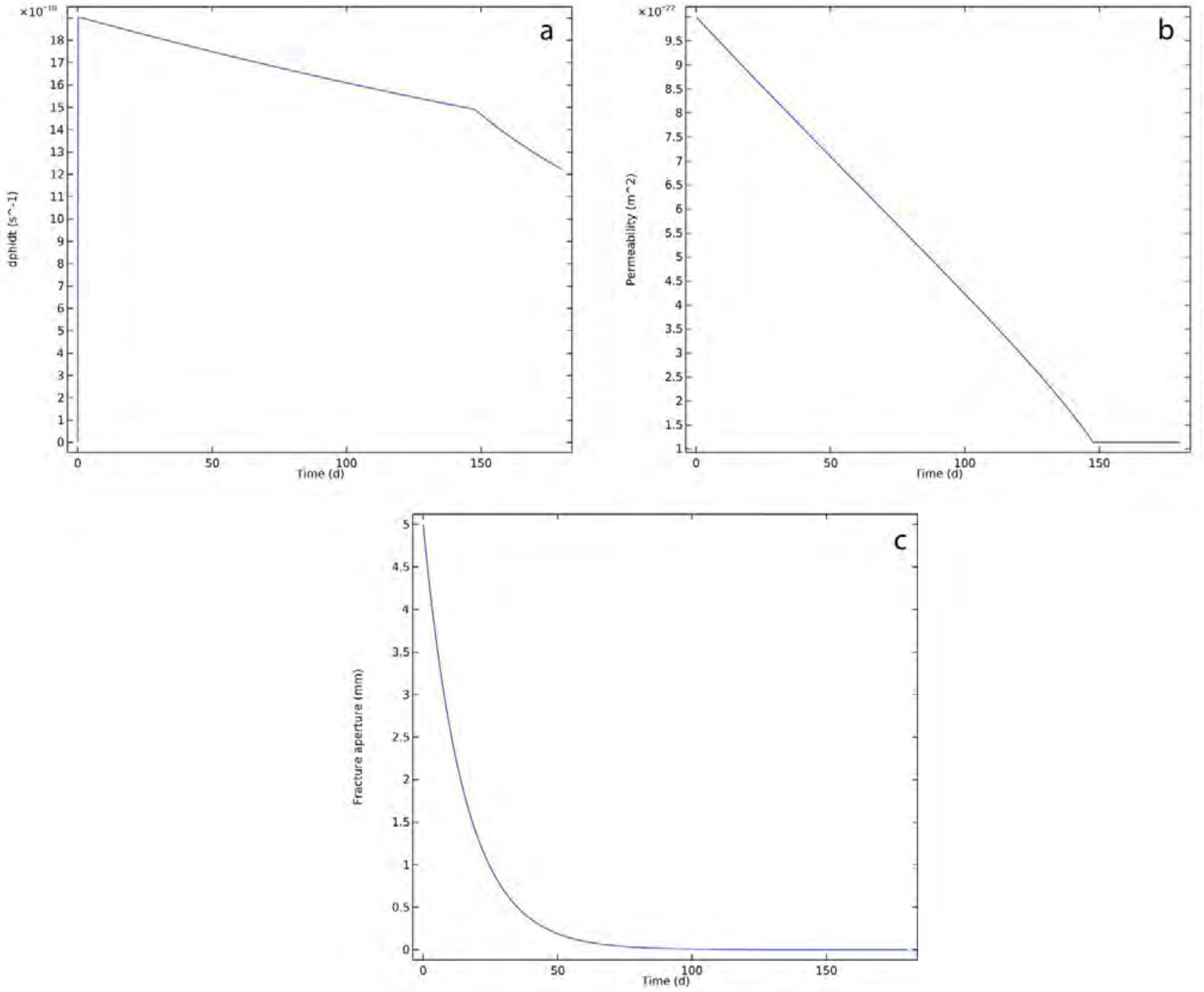

FIGURE 4.5: Time-dependent (a)porosity reduction rate $dphi/dt$, (b) permeability and (c) aperture evolution defined to numerically model the problem.

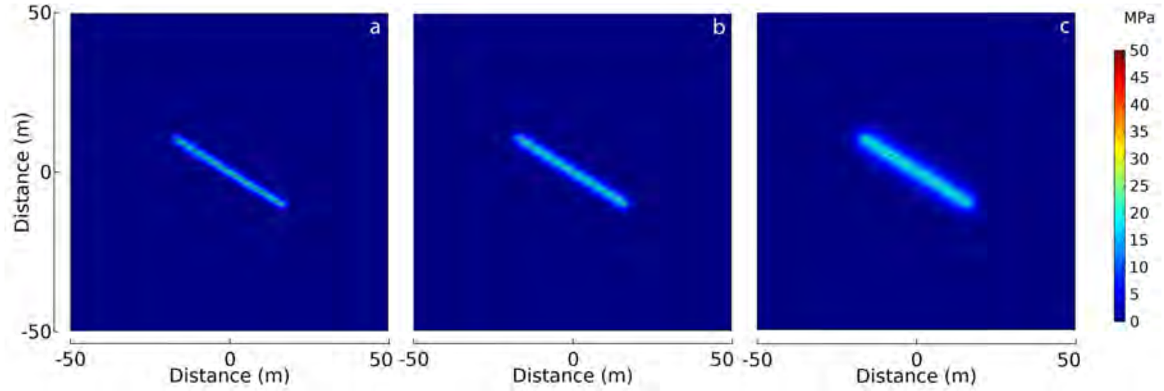

FIGURE 4.6: Fluid pressure (a) 10 days, (b) 30 days and (c) 180 days after fluid introduction via dehydration processes assuming constant porosity in the system.

Figure 4.9 shows time-dependent porosity reduction, where the critical porosity is of 0.02 (half of the initial porosity). The region subjected to porosity reduction becomes more and more visible

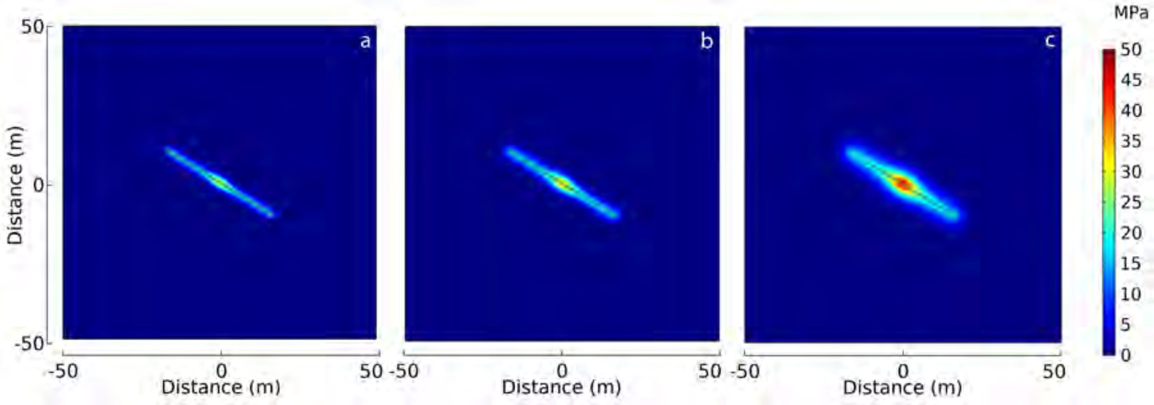

FIGURE 4.7: Fluid pressure (a) 10 days, (b) 30 days and (c) 180 days after fluid introduction via dehydration processes assuming the time-dependent porosity reduction rate as mentioned in Figure 4.5.

with time, although porosity reduction rate stabilizes with time (value taken at the center of the fracture/fault). Figure 4.9 shows time-dependent porosity reduction rate, with the critical porosity is of 0.02 (half of the initial porosity). The region subjected to porosity reduction becomes more and more visible with time, although porosity reduction rate stabilizes with time (value taken at the center of the fracture/fault).

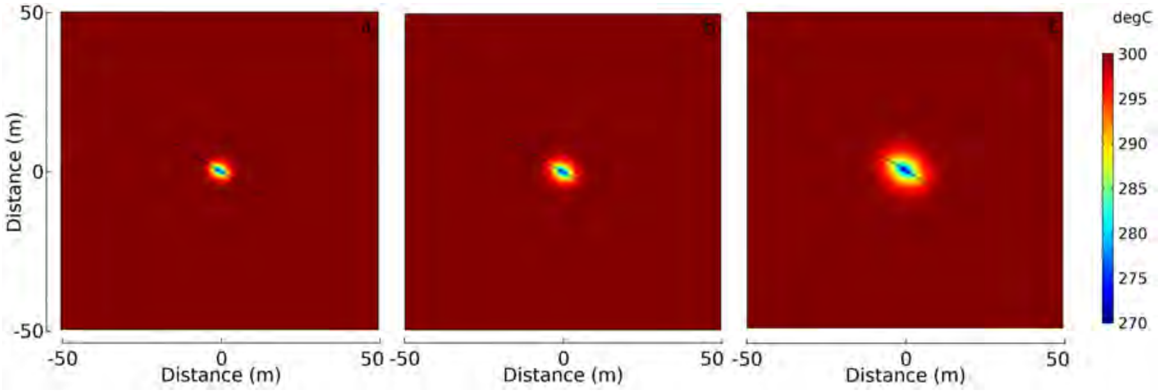

FIGURE 4.8: Temperature (a) 10 days, (b) 30 days and (c) 180 days after fluid introduction via dehydration processes assuming the time-dependent porosity reduction rate as mentioned in Figure 4.3.

Figure 4.10 shows the effective normal stresses acting on the fracture/fault boundary and vicinity assuming constant porosity, whereas Figure 4.11 shows the same variable assuming a time-dependent porosity reduction rate shown in Figure 4.5. We assume maximum and minimum horizontal stresses of 180[MPa] and 120[MPa], respectively. We base the values of maximum horizontal stress on Sulem and Famin, 2009 and we choose the minimum horizontal stress based on Peacock et al., 2011. Peacock et al., 2011 show that fault in cascadia zone is stable (closing or healing) initially when the confining pressure is larger than 100 [MPa]. Results in Figure 4.11 clearly show the

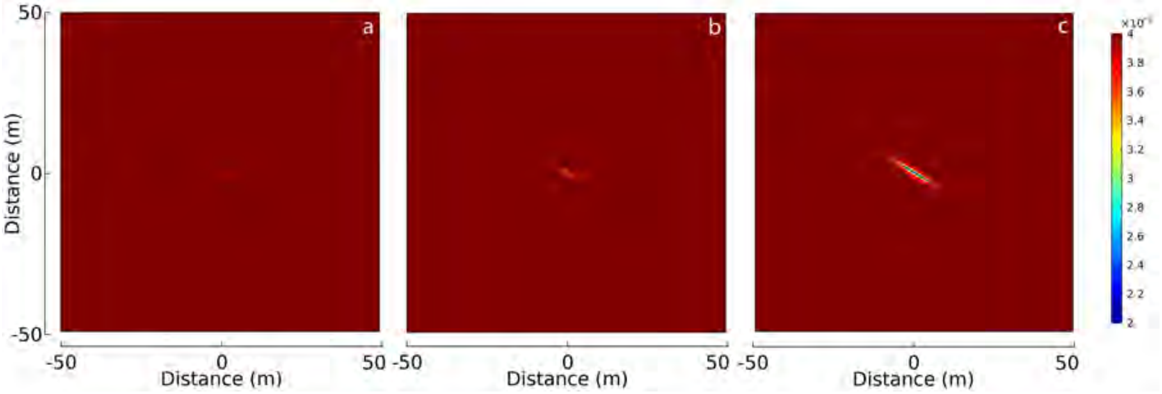

FIGURE 4.9: Porosity (a) 10 days, (b) 30 days and (c) 180 days after fluid introduction via dehydration processes assuming the time-dependent porosity reduction rate as assumed in Figure 4.3.

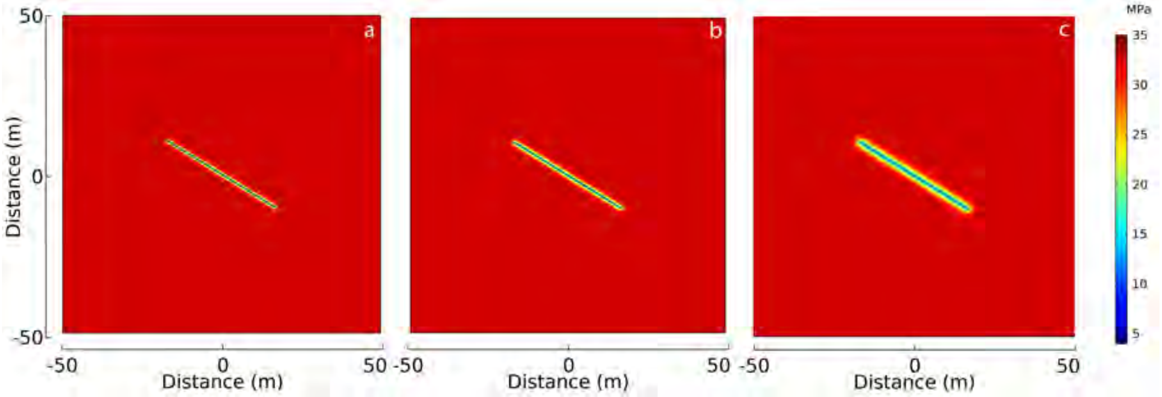

FIGURE 4.10: Effective normal stress (a) 10 days, (b) 30 days and (c) 180 days after fluid introduction via dehydration processes assuming constant porosity.

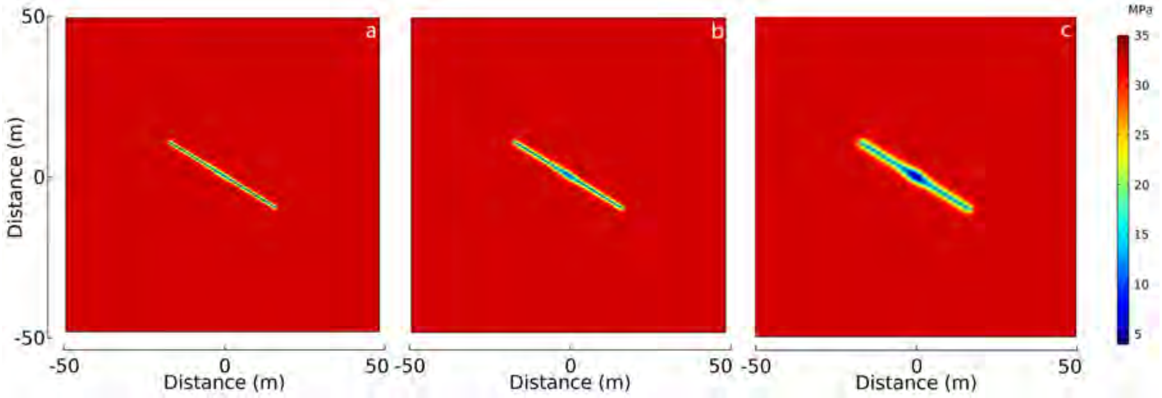

FIGURE 4.11: Effective normal stress (a) 10 days, (b) 30 days and (c) 180 days after fluid introduction via dehydration processes assuming the time-dependent porosity reduction rate as assumed in Figure 4.3.

effects of pore pressure development on the effective normal stress and its radius of influence. The larger the porosity reduction rate, the smaller the effective stress and the wider its effect on fracture stability region.

Figure 4.12 shows Mohr's circle for the studied fracture assuming the time-dependent porosity reduction rate (assumed in Figure 4.5) and a cohesionless rock and a friction coefficient of 0.6. Results show that the fracture/fault remains stable after 180 days of fluids rising via dehydration processes. We test Mohr's circle again assuming a faster porosity reduction rate as shown in Figure 4.13(a) and results show that 180 days after introducing silica-rich fluids, the effective stress crosses the failure slope (Figure 4.13(b)), thus indicating fault slip. Note that a larger porosity reduction rate (Figure 4.13(a)) takes longer time to stabilize, in comparison to porosity reduction rate shown in Figure 4.5(a).

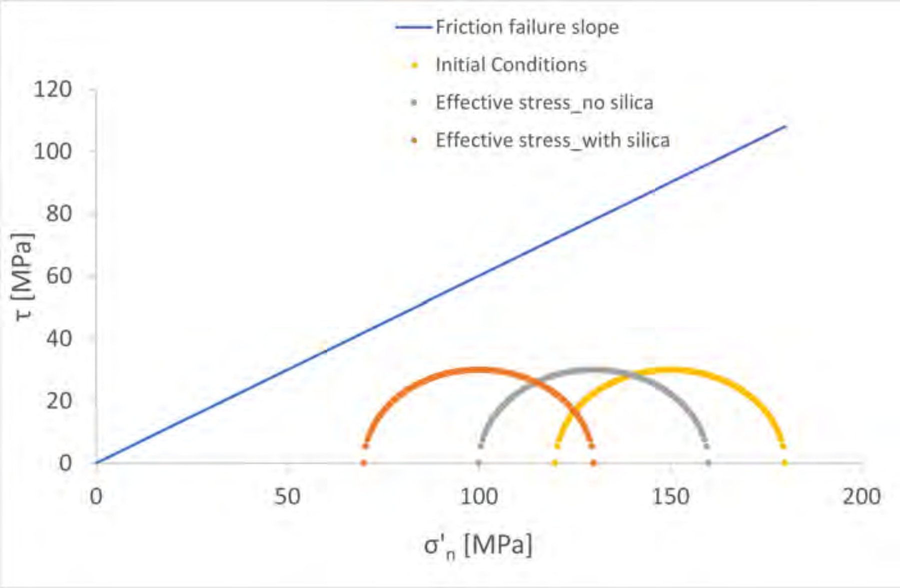

FIGURE 4.12: Mohr's circle 180 days after fluid introduction via dehydration processes assuming the time-dependent porosity reduction rate as assumed in Figure 4.5.

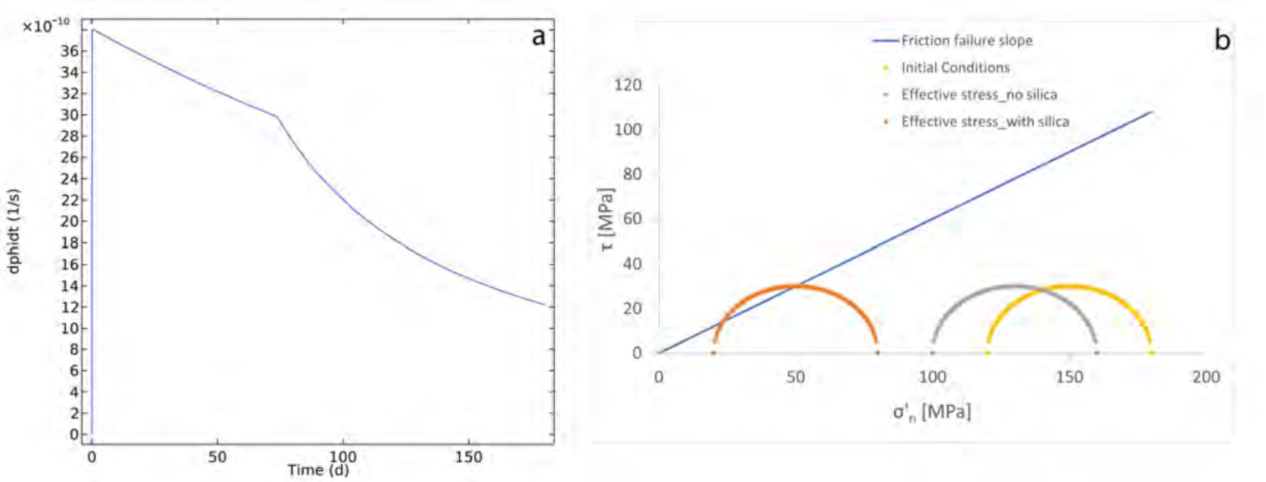

FIGURE 4.13: Mohr's circle 180 days after fluid introduction via dehydration processes (b), assuming a faster time-dependent porosity reduction rate dphidt (a).

4.6 Conclusions

A long standing question about episodic tremor and slip occurrence is how porosity reduction due to silica (as quartz) deposition can result in excess pore pressure, thus reducing the effective stresses and triggering localised slow earthquakes. In this paper, we show that quartz depositing from rising fluids -via dehydration processes- causes pore pressure development and fracture/fault instability. Nevertheless, the theory stands correct under two conditions. First, it is a local problem, particularly due to the low permeability and porosity of these deep high-enthalpy reservoirs. Second, the recurring fracture instability and healing process due to pore pressure development can only be linked to episodic tremor and slip (ETS) if the porosity reduction rate is time-dependent and concentration-based. A slow and steady porosity reduction rate, like what is almost always proposed, will not likely cause any significant increase in pore pressure and hence any fault/fracture instability or failure. For future studies, we encourage looking at possible ETS recurrence times (based on v_p/v_s values) overlap with pore pressure increase due to porosity reduction. Furthermore, it can be interesting to visualize temperature migration in these subduction zone, taking into account the pore pressure increase and accelerated loss in heat. Thus it is possible to visualize damage propagation (tensile failure or weakening) of faults/fractures due to pore pressure development due to the combined effects of porosity reduction and dehydrating fluids being introduced in these high enthalpy reservoirs.

Chapter 5

Conclusions and Outlook

5.1 Conclusions

This thesis investigates the consequences of porosity reduction in geothermal reservoirs due to mineral deposition. Specifically, we employ modern numerical tools to investigate pore pressure development (through porosity reduction Walder and Nur (1984)) and the resulting local fracture/fault instability. We numerically model porosity reduction due to silica (as quartz) precipitation in hydrothermal systems using the sophisticated COMSOL multiphysics platform. Silica is assumed to deposit at the injection well due to lower temperature and higher pressure and to dissolve at the extraction well, where temperature is high and pressure is lower.

This study is divided into three sections, with each section building on the previous. The first section studies the porosity reduction due to quartz precipitation in a geothermal doublet setting featuring an injection well and an extraction well and low porosity, low permeability rock. We investigated different methods of estimating the porosity reduction rate, and mainly compared between a deterministic and an empirical method of calculation. The deterministic method is time- and concentration-dependent, whereas the empirical method depends on coefficients deduced from experimental results run on quartz samples. Results show that the porosity reduction rate from the deterministic approach occurs more slowly than the empirical method, and revealed the importance of porosity reduction rate, rather than the new value of the reduced porosity. That is, a faster porosity reduction rate triggers an abrupt and higher pore pressure increase (in excess of hydrostatic), and resulting in a reverse Darcy flow where fluid flows from the matrix to the reservoir. Over time, this leads to low injectivity and underperforming doublets. Furthermore, heat is transferred from the rock to the injection well, activating quicker temperature losses. The combined effects of pore pressures in excess of hydrostatic and faster temperature losses results in decreasing effective normal stress and ultimately wellbore stability. Enthalpy of silica deposition is found to have negligible effects on temperature evolution. Finally, a simplified verification of stress and displacement shows that the borehole is more likely to suffer tensile failure in the presence of a high porosity reduction rates.

Building on the first section, the second section introduces fractures to the geothermal system in a model for fracture aperture evolution in the presence of quartz precipitation. We study two models; the first model assumes fluid injection from the well into the rock through a horizontal fracture, while the second model assumes a horizontal fracture with the injection well at the center. Fluid in the injection well is characterized by pressure and a temperature that is lower than the rock's temperature. Fracture aperture evolution is assumed to depend on the superposition of chemical and thermal effects. Chemical effects include silica depositing in the system under the right pressure and temperature conditions, thus reducing both rock porosity and fracture aperture.
But is there a connection between fracture aperture evolution and the porosity reduction rate of the surrounding rock?
We show that fracture aperture evolution is highly dependent on the porosity reduction rate of the surrounding rock, where the faster the porosity reduction rate, the higher the pore pressure development (in excess of hydrostatic) at the fracture-rock interface. Furthermore, the faster the porosity reduction rate of the rock surrounding the fracture, the larger the domain of increased pore pressure development (in excess of hydrostatic). Accordingly, reverse Darcy flow occurs and thus affects temperature evolution at the rock-fracture interface and the subsequent thermoelastic effects acting on the fracture aperture. As the system starts to lose heat because of pore pressure development, fracture aperture tends to increase. The initial fracture aperture decreases due to silica deposition, followed by fracture aperture increases due to heat loss when the concentration stabilizes and porosity reduction rate becomes low and constant (steady state). Furthermore, the excess pore pressure decreases the effective stress and renders the fracture unstable. A simplified verification of the effect of fracture inclination shows that fracture inclination can respect the stability conditions under constant porosity conditions and becomes unstable under variable porosity conditions, as seen for inclination angles (55°-85°). Furthermore, a sensitivity study shows that a higher initial injection rate can destabilize a wider range of fracture inclination angles(35°-85°).

The third section of this thesis investigated porosity reduction due to quartz precipitation from rising dehydrating fluids in subduction zones with potential application to episodic tremor and slip

(ETS). Results show that only a time-dependent porosity reduction rate (not a constant steady one) can lead to pore pressure development in such low permeability/porosity high enthalpy systems. Fracture instability can therefore occur assuming a time-dependent, concentration-based, porosity reduction rate. A steady and constant porosity reduction will not lead to any pore pressure jump in the system using the assumed boundary conditions we established. High pore pressure development likely occurs at the local scale, which would initiate fractures that link with neighbouring regions undergoing the same local processes. In this way, the system evolves to a larger-scale inter-connected network of fluid overpressure. We showed that episodic pore pressure development was followed by a decrease in the effective stress and slip of the fracture. This phenomenon can take place about every six months, consistent observationsAudet and Bürgmann, 2014.

5.2 Outlook

Time-dependent porosity reduction and pore pressure development is a complex topic because it involves coupled Thermal, Hydraulic, Mechanical, and Chemical (THMC) processes and interactions. This thesis focused on some of these aspects using carefully established initial and boundary conditions and studied using the COMSOL Multiphysics computational platform. Pore pressure development from mineral deposition, and its consequences, requires additional study because of the many nuances involved, particularly in its likely contribution to slow earthquakes.

There are many means of optimising the study of the effects of pore pressure development due to porosity reduction. First, the porosity reduction term in the pore pressure diffusion equation presented by Walder and Nur, 1984 accounts for reversible and irreversible porosity reduction rate. We considered only irreversible porosity reduction concomitant with mineral precipitation. Future studies linked explicitly with mechanics could include the reversible component of porosity reduction.

Additionally, more thorough modeling of fracture aperture evolution could consider the effects of fracture stiffness and pore pressure development, which was not included in this thesis. We also suggest improving the model by including other minerals that may be encountered in a geothermal system and allow for a multi-mineral deposition model that accounts for a global porosity reduction rate.

Another interesting addition to the study would be to model fracture damage propagation due to pore pressure development in a single fracture or multi-fracture network. An example of fracture activation and damage propagation due to fluid injection was developed by Lei, Doonechaly, and

Tsang, 2021 and modeled using COMSOL Multiphysics. However, an extension of the study to add a source term that depicts porosity reduction rate may be of value, especially when dealing with a high porosity reduction rate and the consequential thermoelastic effects on the fracture aperture evolution.

Finally, it would be interesting to model in greater detail pore pressure development and fracture instability recurrence times. That is, model fracture or fault slip and healing recurrence in high enthalpy reservoirs undergoing porosity reduction due to silica deposition and compare model results with observations (e.g.its recurrence times to that of the ETS using, for example, v_p/v_s).

Appendix A

Uncertainty Quantification for a Hydraulic Fracture Geometry: Application to Woodford Shale Data

A.1 Conclusions

Hydraulic fracturing enhances hydrocarbon production from low permeability reservoirs. Laboratory tests and direct field measurements do a decent job of predicting the response of the system but are expensive and not easily accessible, thus increasing the need for robust deterministic and numerical solutions. The reliability of these mathematical models hinges on the uncertainties in the input parameters because uncertainty propagates to the output solution resulting in incorrect interpretations. Here, I build a framework for uncertainty quantification for a 1D fracture geometry using Woodford shale data. The proposed framework uses Monte-Carlo-based statistical methods and is comprised of two parts: sensitivity analysis and the probability density functions. Results reveal the transient nature of the sensitivity analysis, showing that Young's modulus controls the initial pore pressure, which after 1 hour depends on the hydraulic conductivity. Results also show that the leak-off is most sensitive to permeability and thermal expansion coefficient of the rock and that temperature evolution primarily depends on thermal conductivity and the overall heat capacity. Furthermore, the model shows that Young's modulus controls the initial fracture width, which after 1 hour of injection depends on the thermal expansion coefficient. Finally, the probability density curve of the transient fracture width displays the range of possible fracture aperture and adequate proppant size. The good agreement between the statistical model and field observations shows that the probability density curve can provide a reliable insight into the optimal proppant size.

A.2 Introduction

Hydraulic fracturing (HF) improves the flow rate of recoverable reserves from low permeability geological formations (Economides, 2013, Valkó and Economides, 1995). The process induces rock failure by simply injecting fluid into the reservoir to counteract the in situ stresses and its tensile strength. Such newly created fractures are maintained using proppants often mixed with the fracturing fluid. HF is an expensive practice that requires careful design and good numerical modelling, and a principal problem with these mathematical models is that they are based on ideal systems with physical simplifications, thus neglecting either fracture initiation from wellbore, or near-tip effects, or fracture aperture evolution of preexisting fractures (Abousleiman, Hoang, and Liu, 2014). Although these simplifications facilitate the problem-solving process, they introduce sources of error that reduce the degree of confidence in the output solution (Le Maître and Knio, 2010). Furthermore, uncertainty is embedded in the initial conditions, boundary conditions, geometry, and input parameters (Le Maître and Knio, 2010). Some uncertainties create a large variance of the output solution and contribute most to the prediction of the degree of confidence while others have smaller effects (Wang, 2009). Here, I address the uncertainties in shale formation properties generally calculated in a laboratory/field setting. Shale is a sensitive material, easily disturbed by normal drilling techniques, and specimens are difficult to sample, core, characterize, and test (Lashkaripour, 2002). Furthermore, well logs measure formation properties such as Young's modulus, Poisson's ratio, and permeability, but well log interpretation is a subjective practice, where the tools have a margin of error and the measured properties are spatially limited. In this study, I investigate Woodford shale, a major source rock located in the Midwestern U.S. Its low permeability makes it difficult to fully profit from its potential, making it a perfect case study for HF. Field observations for Woodford shale (Portas Arroyal, 2009) show that its natural fractures have a vertical dip and strike West-East with an average distance between fractures of 1.2-1.5 (m) (Figure A.1).

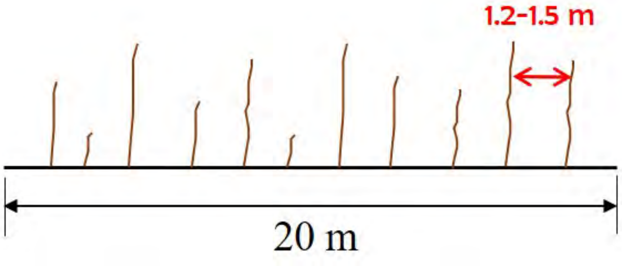

FIGURE A.1: Simplified drawing of the natural fractures in Woodford shale.

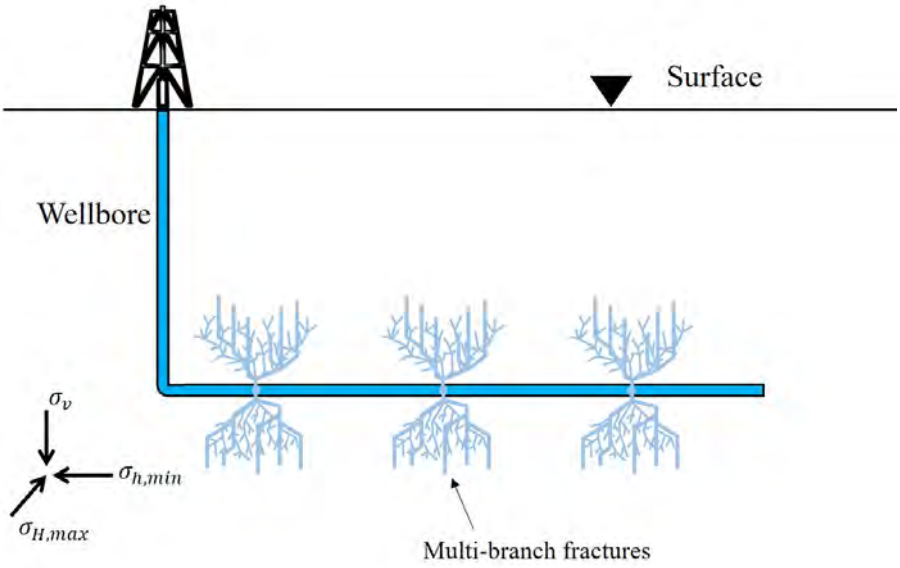

FIGURE A.2: Conceptual model for hydraulic fracturing in shale reservoir with preexisting natural fractures. Horizontal well injection initiates multibranch fractures. I delimit the study to one multibranch fracture highlighted with a purple dashed box.

Hydraulic fracturing reactivates these preexisting fractures, thus creating multibranch fractures (Figure A.2). Quantifying the effects of spatial variability in formation properties [8, 9] on the reliability of hydraulic fracture simulations has been studied (Lashkaripour, 2002, Amanipoor et al., Lashkaripour and Dusseault, 2020, Zio and Rochinha, 2012, Berrone et al., 2018) but is restricted by simplified deterministic solutions or computational timescales of numerical solutions. The uncertainty quantification for the simple linear elastic model given by (Zio and Rochinha, 2012) calculates the range of possible fracture apertures using Monte-Carlo simulations where Young's modulus and the confining stress are random parameters, and they consequently reformulate the governing equations as stochastic partial differential equations (SPDEs). They adopt a stochastic collocation method to solve these SPDEs and replace the classic Monte-Carlo methods with two different methodologies: (1) the input parameters respect a log-normal distribution function, where only the mean and the dispersion values are used to calibrate the model, and (2) the input parameters fall within 96% of the log-normal distribution (a method called maximum entropy). They show that the probability distribution function of Young's modulus and the confining stress greatly impact that of the fracture aperture. Furthermore, (Zio and Rochinha, 2012) were inspired by (Ma and Zabaras, 2011) who developed the stochastic framework to efficiently perform uncertainty quantification for fluid transport in porous media in the presence of both stochastic permeability and multiple scales and present the solution as a polynomial approximation. In a recent publication, (Berrone et al., 2018) address variability in discrete fracture network geometry using the very robust multilevel Monte-Carlo methods, rather than the stochastic methodology claiming that the classic stochastic collocation fails to provide reliable estimates of first-order moments of the output solution due to the lack of smoothness. In another recent publication, (Pieraccini, 2020) proposes the (MLMC) methods in conjunction with a well assessed underlying solver to perform DFN flow simulations using Darcy flow and prove that the method is robust enough to tackle complex geometrical configurations, even with very coarse meshes. (Nejadi et al., 2015) address the heterogeneities in fractured reservoirs and assume that the fracture intensity, orientation, and conductivity of different fracture sets are the uncertain parameters. They confer each parameter with a probability distribution and create an integrated history matching workflow for fractured reservoirs assuming numerical methods for multiphase flow simulation, while updating the fracture properties via dynamic flow responses, such as continuous rate and pressure measurements. They generate initial realizations using Monte-Carlo simulations and based on observed fractures at the well locations. The automated history matching approach results in multiple equally probable discrete fracture network models, where upscaled flow simulation models honour both the geological information and the dynamic production history. Furthermore, (Delgado and Kumar, 2014) use uncertainty quantification for coupled subsurface flow and deformation processes. They circumvent the slow convergence of the traditional Monte-Carlo methods using an intrusive polynomial chaos expansion method for Biot's poroelasticity equations based on Galerkin projection with uniform and log-normally distributed material parameters. Results show good agreement with the Monte-Carlo and ANOVA-based probabilistic collocation methods.

Although significant studies have been presented on uncertainty quantification in hydraulic fracturing, they are restricted to finite element schemes with defined mesh size and number of random values. Furthermore, they focus on geometric properties or are limited to elastic formation parameters, rather than rank all formation properties including the thermal properties, which is covered in this paper. The purpose here is to address formation inhomogeneity and spatial variability in low permeability shale reservoirs and their impact on fracture response using a unique but simple framework for uncertainty quantification comprising of sensitivity ranking and probability density curves. Then, I test the validity of the framework on the 1D porothermoelastic analytical solution for pressure, temperature, leak-off, and width given by (Abousleiman, Hoang, and Liu, 2014), with application to Woodford shale data. A series of simulations demonstrate uncertainty propagation in the deterministic solution and describe the probability density function (PDF) for the fracture width to explain why some proppants have higher success rates than others.

A.3 Materials and Methods

A.3.1 Conceptual model

Analytical solutions for pressure, temperature, strain and displacement are derived in detail by (Abousleiman, Hoang, and Liu, 2014) following the 1D consolidation theory.

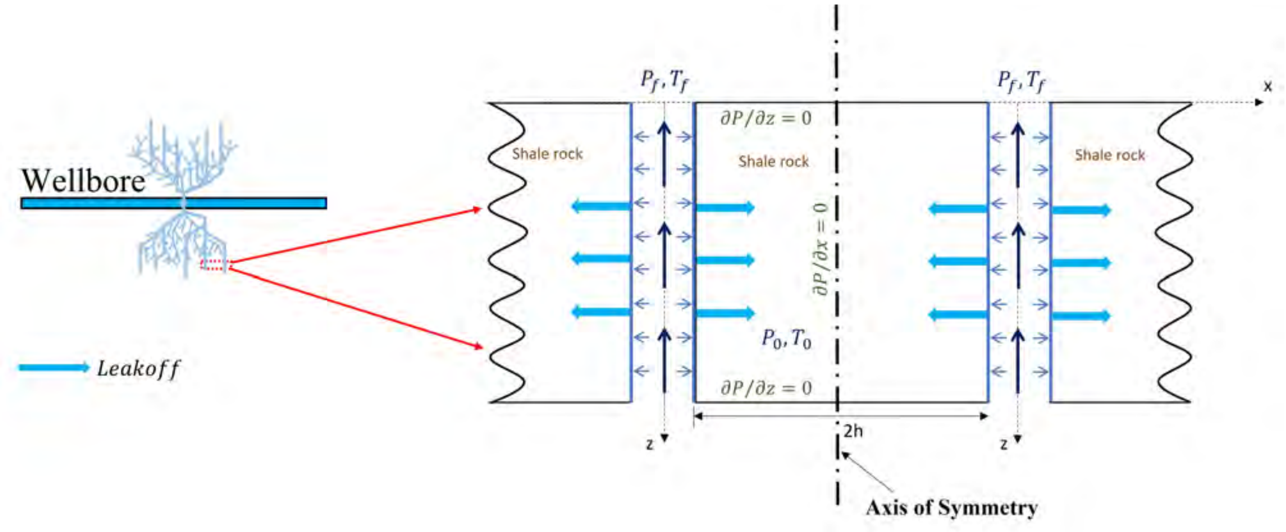

FIGURE A.3: The red dashed box zooms-in to two consecutive fractures and shows the fracture geometry with the initial and boundary conditions: P_f and T_f are the fluid pressure and temperature, respectively. P_0 and T_0 are the initial pressure and temperature, respectively. The 1D solution is limited to h because of the symmetry.

Figure A.3 zooms in to a multi-branch fracture and shows how the fracture apertures are perpendicular to the minimum horizontal stress $\sigma_{h,min}$, and intersect a porous medium characterized with an initial pore pressure P_0 and an original temperature T_0, and subject to fracturing fluid with pressure P_f and temperature T_f at its faces (Figure A.3). Figure A.3 also shows that the distance between two consecutive fracture apertures is 2h, but because of the mirror symmetry, the one-dimensional solution is constrained to the length h. Furthermore, the pore pressure gradient induces fluid leakoff from the fracture into the formation at each fracture face, and impermeable, adiabatic, and frictionless boundary conditions prevail at the axis of symmetry.

A.3.2 Governing Equations

The one-dimensional consolidation for transversely isotropic material is described in detail by (Abousleiman, Hoang, and Liu, 2014), but a brief summary of the equations is presented here for the sake of completeness. Assuming the xy plane is the isotropic plane and the z axis is the axis of rotational symmetry (Figure A.4), the coupled equations for pressure, temperature, and displacement represent the response of the hydraulic fracture system.

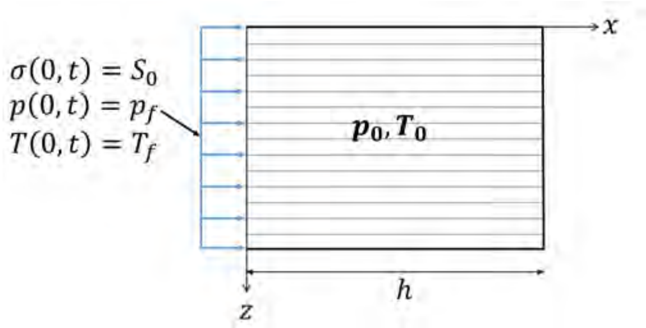

FIGURE A.4: One-dimensional consolidation setup showing the initial and top boundary conditions, where the plane xy is the isotropic plane, where the x axis has a subscript of 1, and the z axis is the axis of rotational symmetry with a subscript of 3. The top, bottom and right boundaries (in bold) are assumed impermeable, adiabatic and frictionless.

First, the analytical pressure solution is derived as:

$$p(x,t) = \frac{2}{h} \sum_{m=0}^{\infty} \frac{1}{\xi} \left(c_1 e^{-\gamma_1 \xi^2 t} + c_2 e^{-\gamma_2 \xi^2 t} \right) \sin \xi x + \Delta P \tag{A.1}$$

then, the temperature is given by:

$$T(x,t) = \frac{2}{h} \sum_{m=0}^{\infty} \frac{1}{\xi} \left(c_3 e^{-\gamma_1 \xi^2 t} + c_4 e^{-\gamma_2 \xi^2 t} \right) \sin \xi x + \Delta T \tag{A.2}$$

finally, the displacement is given by:

$$\begin{aligned} u\left(x,t\right) = {} & \frac{S_0 - \alpha_1 \Delta P - \beta_1^s \Delta T}{M_{11}} (x-h) + \frac{2\alpha_1}{M_{11} h} \sum_{m=0}^{\infty} \frac{1}{\xi^2} \left(c_1 e^{-\gamma_1 \xi^2 t} + c_2 e^{-\gamma_2 \xi^2 t} \right) cos \xi x \\ & + \frac{2\beta_1^s}{M_{11} h} \sum_{m=0}^{\infty} \frac{1}{\xi^2} \left(c_3 e^{-\gamma_1 \xi^2 t} + c_4 e^{-\gamma_2 \xi^2 t} \right) cos \xi x \end{aligned} \tag{A.3}$$

where h is the half distance [m], ξ is $(2m+1)\,\pi 2h$ [m^{-1}], S$_0$ is the stress boundary condition that is the difference between the fracturing fluid pressure Pf [MPa] and the minimum horizontal stress S$_{hmin}$ [MPa], M11 is the stiffness coefficient [MPa] calculated from Young's modulus and Poisson's ratio, β_1^s is a thermal parameter calculated from the stiffness coefficients and the solid thermal expansion coefficient [MPa deg C^{-1}] and α_1 is Biot's coefficient [1], and c1, c2, c3, c4, γ_1,γ_2 are lumped parameters defined as: $c_1 = \frac{\gamma_1 \gamma_2 [g_{11}(p_0 - \Delta P) - g_{12} \Delta T] - (p_0 - \Delta P)\gamma_1}{(-\gamma_1 + \gamma_2)}; c_2 = p_0 - \Delta P - c_1; c_3 = \frac{c_1(1 - \gamma_1 g_{11})}{\gamma_1 g_{12}}; c_4 = -\Delta T - c_3 \gamma_1 = \frac{g_{11} + g_{22} + \sqrt{(g_{11} + g_{22})^2 - 4g^*}}{2g^*}; \gamma_2 = \frac{g_{11} + g_{22} - \sqrt{(g_{11} + g_{22})^2 - 4g^*}}{2g^*}$ and g$_{11}$, g$_{12}$, g$_{21}$, g$_{22}$, and g* are

defined as: $g_{11} = \frac{\mu}{k_1}\left(\frac{1}{M} + \frac{{\alpha_1}^2}{M_{11}}\right); g_{12} = \frac{\mu}{k_1}\left(\frac{\alpha_1 \beta_1^s}{M_{11}} - \beta^{sf}\right);$
$g_{21} = \frac{\alpha_1 \beta_1^s T_0}{\lambda_1 M_{11}}; g_{22} = \frac{1}{\lambda_1}\left(v + \frac{\left(\beta_1^s\right)^2 T_0}{M_{11}}\right); g^* = g_{22}g_{11} - g_{12}g_{21}$

Where is the fluid viscosity [Pa s], k_1 is the permeability [m^2], M is a poroelastic parameter in [MPa], λ_1 is the thermal conductivity [J m^{-1} s^{-1} deg C^{-1}], and ρC_v is the overall thermal capacity [J/(m^3 deg C)]. Note that subscripts 1 and 3 represent the x direction and the z direction, respectively. The initial and boundary conditions associated with Eqs. (1)-(3) are given as follows: p(x,0)=p$_0$; $p(0,t) = p_f; T(x,0) = T_0; T(0,t) = T_f;$ $\left.\frac{\partial p}{\partial x}\right|_{(h,t)} = 0;$ $\left.\frac{\partial T}{\partial x}\right|_{(h,t)} = 0; u(h,t) = 0.$

Despite the complexity of the poro-thermo-elastic solution, one can easily identify the contributing formation properties. The theory of linear elasticity assumes the rock as a dry solid material characterized by E, Young's modulus [GPa] and ν, Poisson's ratio []. However, pore fluid alters the mechanical behaviour of the porous rock, thus introducing three additional poroelastic parameters:α Biot's coefficient [], M Biot's modulus [GPa] and κ the mobility ratio (ratio between permeability of the formation and viscosity of the pore fluid: $k\mu$) [m^2 Pa^{-1} s^{-1}]. In addition, the one-dimensional anisotropic solution couples the poroelastic solution with the effects of the thermal gradient (between the fracturing fluid and the rock formation), thus introducing thermal parameters to the solution: the solid skeleton linear thermal expansion coefficient ${\alpha_i}^s$[deg C^{-1}] in the i^{th} direction, the volumetric thermal expansion coefficient of the pore fluid α^f [deg C^{-1}], the thermal conductivity of the porous medium λ_1 (in the x direction) [J m^{-1} s^{-1} deg C^{-1}] and the overall thermal capacity ρ C_v [J m^{-3} deg C^{-1}]. Finally, the anisotropic nature of shale has a significant impact on its mechanical responses (Abousleiman, Hoang, and Liu, 2014) and is included in this study. Table 1 enumerates the formation properties contributing to the uncertainty study for the 1D anisotropic poro-thermo-elastic solution.

TABLE A.1: Formation properties used to model the uncertainty in the hydraulic fracture responses.

E$_i$	Young's Modulus in the ith direction
ν_i	Poisson's ratio
${\alpha_i}^s$	Solid skeleton linear thermal expansion coefficient in the ith*direction*
κ_1	Mobility ratio in the x direction
λ_1	Thermal conductivity in the x direction
ρC_v	Overall thermal capacity

Below I detail the proposed uncertainty quantification (UQ) framework comprised of two parts: 1) sensitivity ranking to rank the input parameters by order of degree of influence on the output solution and 2) probability density function of the output solution that depicts all possible HF responses and their corresponding likelihood.

A.3.3 Part I: Sensitivity analysis

To analyse the propagation of uncertainties, one must study how the output solution varies when the input variable takes on different values (Wang, 2009). Using the popular Monte Carlo methods, one generates a set of realizations of the input data $\{d_1, d_2, d_3, \ldots\}$, each characterized by a known probability distribution law, and calculate the correspondent solution s of the model $\{s_1, s_2, s_3, \ldots\}$, then measure its statistics (Le Maître and Knio, 2010). The Monte-Carlo methods have the advantage of being robust; that is, there are no constraints on the variances of the input data and the output. These methods are independent from the dimensionality of the random values (RVs) but require the deterministic solution and are characterized with a slow convergence rate. Although there are methods to increase the convergence rate such as variance reduction methods, a convergence rate of $M^{-1/2}$ governs all Monte-Carlo methods, thus requiring a large population size M (Le Maître and Knio, 2010, Wang, 2009). As a result, these methods are impeded by high computational cost and time.

Sensitivity Analysis addresses the first part of the framework, where I rank input parameters by their order of influence on the variance of the solution. One of simplest and most practical methods to perform sensitivity analysis is the one at a time method (OAT). In this method, one studies each parameter individually to minimize the chances of computer crashes. Typically, one random input parameter is assumed, while maintaining all others to their originally assigned values. The sensitivity analysis is driven by this random parameter that produces a host of possible output solutions. The steps for the OAT approach are listed in the below text for a deterministic solution, $y = f\,(x_{i=1}, x_{i=2}, \ldots . x_{i=m})$ with m input parameters.

- Consider x_1 a random input parameter that fits a defined distribution function, e.g. normal distribution, with an assigned mean and standard deviation, and generate $N_{population}$ of $_1$. Figure A.5 shows the population distribution for Young's modulus E_1 [GPa] converging for $N_{population} = 15,000$.
- Calculate the deterministic solution for each value of x_1.
- Calculate the variance of the $N_{population}$ values of output solution and note it as y_1;
- Repeat procedure for each of the other input parameters $i = [2 : m]$.
- Calculate the sum of the output solution y_i for m values of variance. $\sum_{i=0}^{m} y_i$.

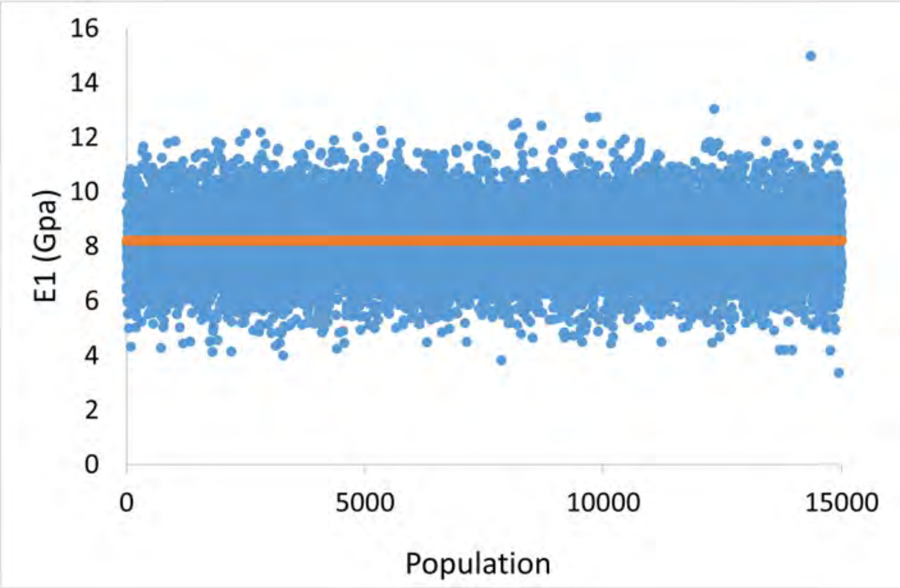

FIGURE A.5: Monte-Carlo population simulation for Young's modulus with $N_{population} = 15,000$ with an average of 8.21 [GPa] and a standard deviation of 1.2 [GPa] assuming a normal distribution.

- Calculate the coefficient of variation $\frac{y_1}{\sum_{i=1}^{m} y_i}$ for each input parameter. This coefficient represents the degree of influence of each input parameter on the output solution.

A.3.4 Part II: Probability density curves

Proposed methods for uncertainty quantification include the probability density function (PDF), where its value is always positive and its integral over the entire range of possible values equals to one. To generate the PDF, one simultaneously introduces the high-ranking random input variables (from first part of the framework) in the deterministic solution and fit the range of output results to a probabilistic distribution type (normal, triangular, Gumbel, lognormal, etc…). The procedure for a deterministic solution $y = f\ (x_{i=1}, x_{i=2}, \ldots .x_{i=m})$ with m input parameters is as follows:

- Select the input parameters with a high sensitivity ranking (from sensitivity analysis) as random variables and keep the formation parameters with a negligible effect to their original value.
- Generate a population of n values for each of the selected random variables and calculate the output solution.
- Plot the histogram of all the n output values.
- Fit the histogram to a distribution function and calculate the PDF function.

A.4 Results

A.4.1 Woodford Shale Data

I test the proposed framework on the 1D solution with typical Woodford Shale data presented in Table 2 (Gilliam and Morgan, 1987, Abousleiman et al., 2007, Aoudia, 2009, Sierra et al., 2010). The transversely isotropic nature of this low permeability shale signifies that its properties depend on the direction, where x has a subscript of 1 and z a subscript of 3 (Figure A.3), except for the linear thermal expansion coefficient that is independent of the direction and is replaced with one value α^s. The model considers thermal effects because of the significant temperature difference $\Delta T = 60°C$ between the fracturing fluid temperature $\left(T_f = 30°C\right)$ and the formation temperature $(T_0 = 90°C)$.

TABLE A.2: Woodford shale data used to test the sensitivity of the model to the input uncertainties.

Mobility ratio, κ_1	$45\ m^2/(Pa\ s)$
Solid skeleton linear thermal expansion coefficient, α^s	$2 \times 10^{-5}°C$
Overall heat capacity, ρC_v	$2.75\ J/(m^3°C)$
Thermal conductivity, λ_1	$1.4\ J/(m\ s°C)$
Original pore pressure, p_o	27.6 MPa
Original temperature, T_o	90 °C
Minimum horizontal stress, $\sigma_{h,min}$	52 MPa
Stress boundary condition, S_0	12 MPa
Fracturing fluid pressure, p_f	64 MPa
Fracturing fluid temperature, T_f	30 °C
Young's modulus, E_1, E_3	5.6, 4.6 GPa
Poisson's ratios, ν_1, ν_3	0.3
Distance between vertical apertures, $2h$	1.2 m

However, literature review (Gilliam and Morgan 1987, Abousleiman, Tran et al. 2007, Sierra, Tran et al. 2010) confirms a large variability in some of those properties, summarized in Table 3.

TABLE A.3: Variability of some Woodford shale formation properties from field measurements.

Mobility ratio, κ_1	20-60 nD/cP
Solid skeleton linear thermal expansion coefficient, α^s	$(0.9\text{-}4.8)\times 10^{-5}$ °C
Overall thermal capacity, ρC_v	$2.57\text{-}2.94\ J/(m^3\ °C)$
Thermal conductivity, λ_1	$0.7\text{-}1.4\ J/(m\ s°C)$
Young's modulus, E_1, E_3	6.8-9.8; 3.85-5.6 GPa
Poisson's ratio, ν_1, ν_3	0.1-0.15; 0.23-0.3

A.4.2 Sensitivity Analysis: Application to Woodford shale

The saturated porous medium in Figure A.4 is subjected to an instantaneous compression due to injection, and as a result experiences a pore pressure jump, also known as the Skempton's effect. The pressure at the shale-fracture interface is the constant injection pressure Pf and consequently, the sensitivity score for all parameters is zero at x=0 [m] (Figure A.6). Figure A.6 shows that the dominant control on the initial pore pressure (Equation 1) is the elastic Young's modulus E_1 with a sensitivity score of 90%. As pressure distribution stabilizes inside the half-space, the sensitivity of the pore pressure to E_1 decreases and other formation properties come into play, as shown in Figure A.7. Figures A.7(a)-(c) show that as the pore pressure front diffuses inside the formation, the sensitivity of pressure to E_1 significantly decreases and the pore pressure becomes more sensitive to the mobility ratio κ_1, the thermal conductivity λ_1 and the skeleton linear thermal expansion coefficient α^s, respectively. The reason why thermal properties influence the pore pressure response is that the temperature gradient forces the fluid and rock to contract as the cooling front penetrates further inside the half-space.

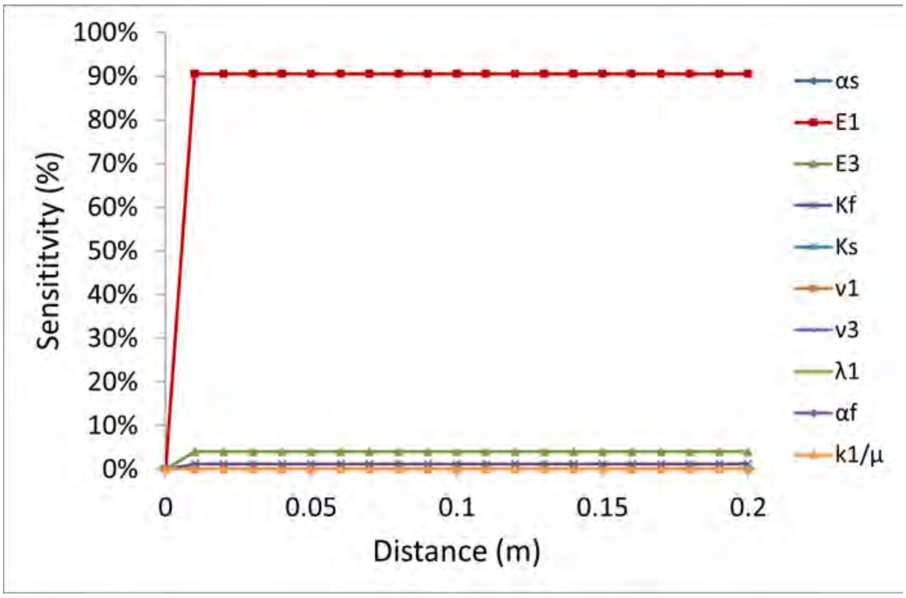

FIGURE A.6: Sensitivity ranking for pressure in the fracture at time t=0+. The instantaneous pore pressure jump is 90% governed by Young's modulus E_1.

λ_1 is the second most dominant parameter, where its influence reaches 0.09 [m] at t=15 [min] (Figure A.7(a)), 0.12 [m] at t=30 [min] (Figure A.7(b)) and 0.18 [m] at t=60 [min] (Figure A.7(c)), and α^s is the third most dominant parameter, where its influence reaches 0.06 [m] at t=15 [min] (Figure A.7(a)), 0.09 [m] at t=30 [min] (Figure A.7(b)) and 0.12 [m] at t=60 [min] (Figure A.7(c)).

The thermal conductivity λ_1 sensitivity curve presents a peak that coincides with the dip in the mobility ratio sensitivity curve for x=0.04 [m] at t=15 [min] (Figure A.7(a)), x=0.05 [m] at t=30 [min]

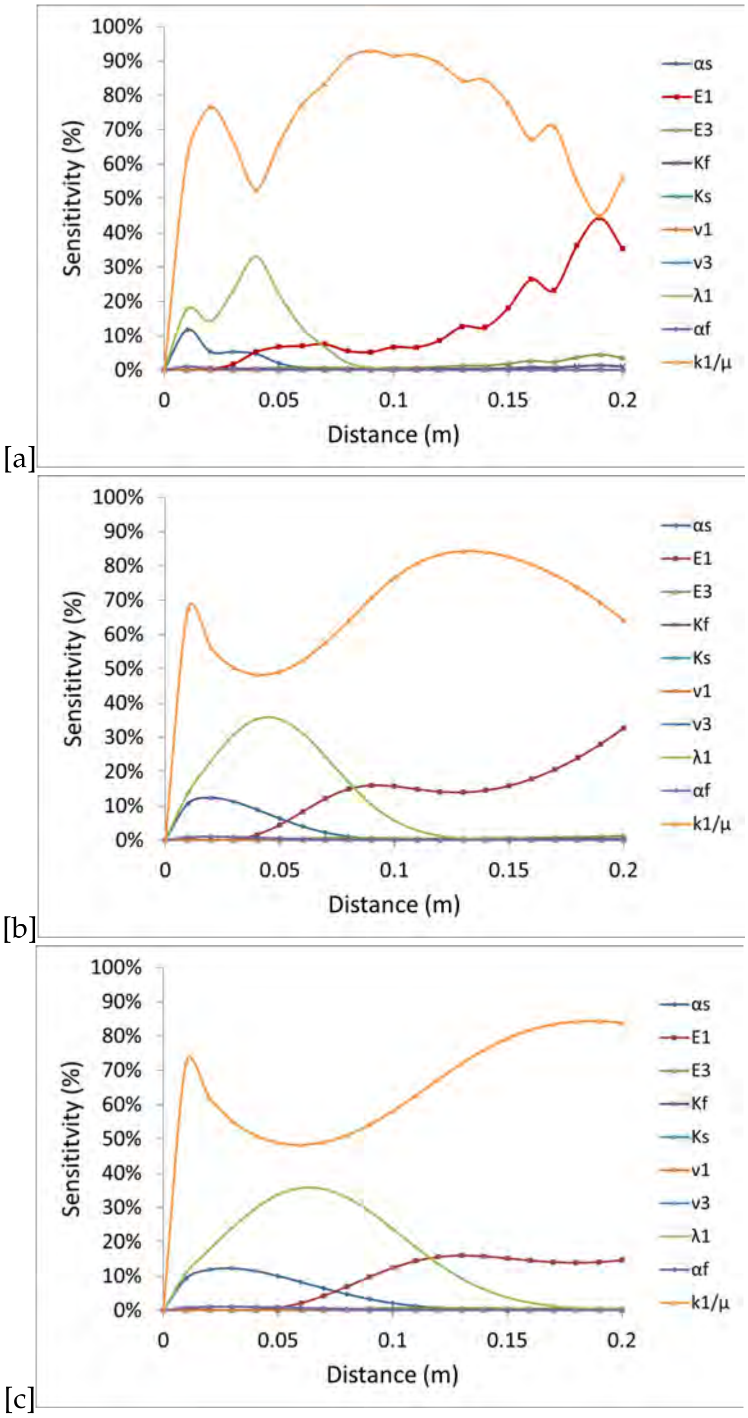

FIGURE A.7: Sensitivity ranking for pressure in the fracture at time a) t=15 [min], b) t=30 [min] and c) t=60 [min].

(Figure A.7(b)) and x=0.06 [m] at t=60 [min] (Figure A.7(c)), highlighting a lower pressure zone, as seen in (Abousleiman, Hoang, and Liu, 2014). After 30 [min] of injection, the dip of the mobility ratio κ_1 stabilizes at 48% and the peak in the thermal conductivity λ_1 stabilizes at 38%. Figure A.7(a)-(c) also show that beyond the pore pressure front lies a zone where pore pressure is only sensitive to E_1 and κ_1, such as: $x > 0.1$ [m] at t=15 [min] (Figure A.7(a)), $x > 0.12$ [m] at t=30 [min] (Figure A.7(b)) and $x > 0.18$ [m] at t=60 [min] (Figure A.7(c)).

I proceed to perform sensitivity ranking for the Temperature (Equation 2), where contrary to the pore pressure, temperature is independent of any formation parameter at time t=0+, because the temperature front takes finite time to diffuse inside the formation.

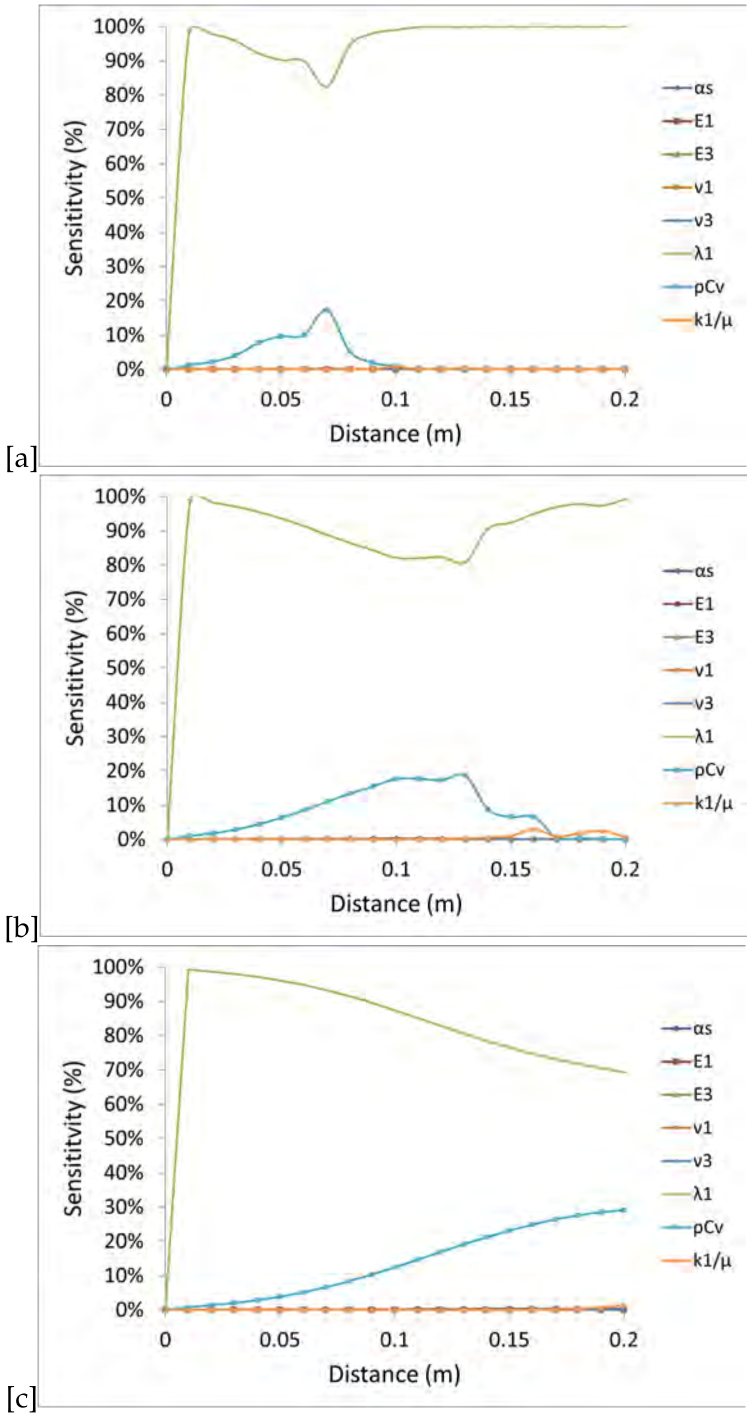

FIGURE A.8: Sensitivity ranking for temperature in the fracture at time a) t=15 [min], b) t=30 [min] and c) t=60 [min].

Figure A.8(a) shows that at t=15 [min], the cooling front reaches 0.11 [m] and depends on the thermal conductivity λ_1 and the overall thermal capacity ρC_v. Figure A.8(b)-(c) show that the sensitivity of the temperature to ρC_v increases while the influence of λ_1 continues to decrease but remains dominant, with a sensitivity score of 70% for λ_1 and for of 30% for ρC_v at $t = 60$ [min] and for $x = 0.2$ [m]. This is particularly interesting because while pressure depends on thermal properties, temperature only depends on two temperature properties, where the temperature at the shale-fracture interface ($x = 0$ [m]) only depends on the thermal conductivity λ_1. Note that the Monte-Carlo simulation for temperature becomes smoother as the system stabilizes and reaches a steady condition. Next, the 1D solution provides an expression for the fluid flow based on Darcy's law, where the leakoff velocity is the flow at the shale-fracture interface ($x = 0$ [m]).

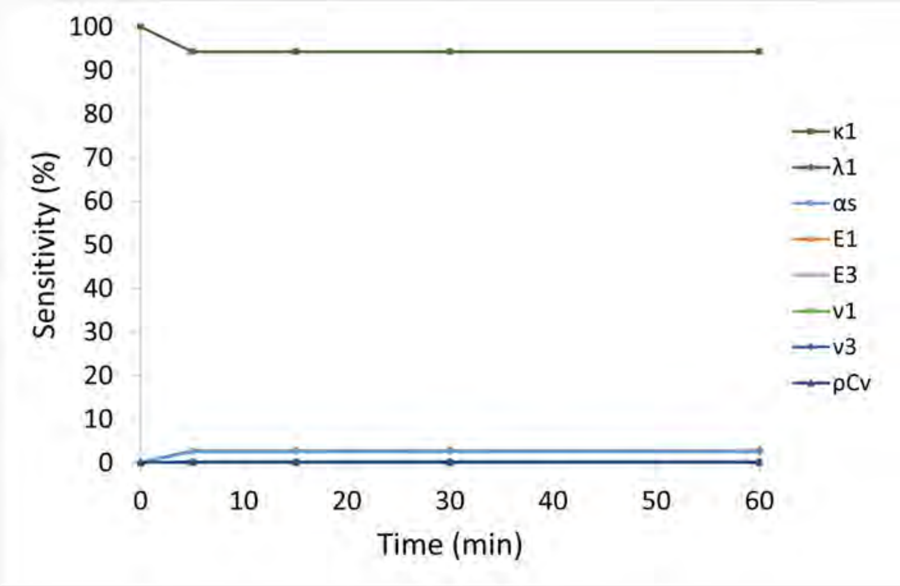

FIGURE A.9: Sensitivity ranking for the transient leakoff velocity [m/s].

Figure A.9 shows that the leakoff velocity is most sensitive to the mobility ratio κ_1 and the thermal conductivity λ_1, with a sensitivity score of 90% and 10%, respectively. Finally, the fracture width is the displacement at the shale-fracture interface, $x = 0$ [m] (Equation 3). Similar to the pressure (Figure A.6 (a)), fracture width is initially ($t = 0+$) most sensitive to the elastic Young's modulus E_1 (Figure A.10), but because thermal effects are factored in the rock deformation process, the influence of E_1 decreases with time, while the linear thermal expansion coefficient α^s, the mobility ratio κ_1 and the thermal conductivity λ_1 start to play a larger role in the displacement solution. Figure A.10 shows that after 60 [min], the fracture width becomes most sensitive to α^s (75%), followed by κ_1 (12%), λ_1 (9%) and E_1(3%).

Table A.4 summarizes the formation properties with a high sensitivity ranking. I consider the

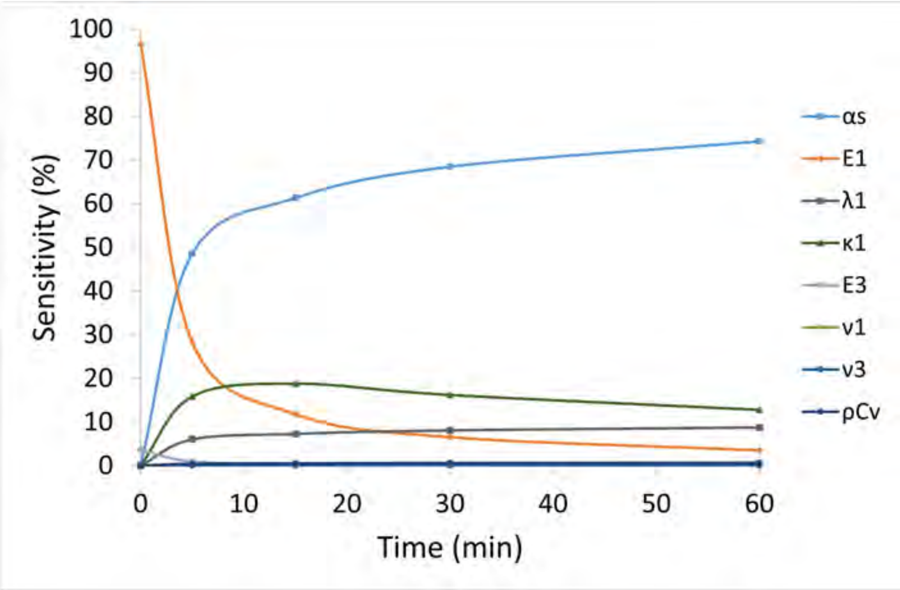

FIGURE A.10: Sensitivity variation of the fracture width [mm].

parameters with Y attribute for this second part and generate the probability density functions to quantify uncertainty in the output solution.

TABLE A.4: Sensitivity analysis summary showing which input parameters influence the solution. Y is for yes and N is for No. Output Parameters

Output	Parameters							
	α^s	E_1	E_3	ν_1	ν	λ_1	ρC_v	κ_1
Pressure	Y	Y	N	N	N	Y	N	Y
Temperature	N	N	N	N	N	Y	Y	N
Leakoff	N	N	N	N	N	N	N	Y
Fracture width	Y	Y	N	N	N	Y	N	Y

A.4.3 Probability Density Functions: Application to Woodford shale

Figures A.11(a)-(c) show the probability density functions (PDFs) of the pore pressure response (considering the simultaneous variability of the four parameters indicated with Y in Table 4), at times $t = 15$ [min], 30 [min] and 60 [min], respectively. The pore pressure variability fits a normal distribution function, where the pressure is fixed at 64 [MPa] at the shale-fracture interface, $x = 0$ [m]. That is, PDF at this boundary is 100% and is not included in the plots.

Figure A.11(a) shows that the transient pore pressure front diffuses from the boundary and reaches a depth of $x = 0.1$ [m] at $t = 15$ [min], to stabilize at a pressure range of 30-35 [MPa], for $x > 0.1$[m], which corresponds to the pore pressure jump felt in the porous medium at $t = 0^+$. Figure A.11 (b) shows that the pressure diffusion reaches 0.15 [m] and Figure A.11 (c) shows diffusion

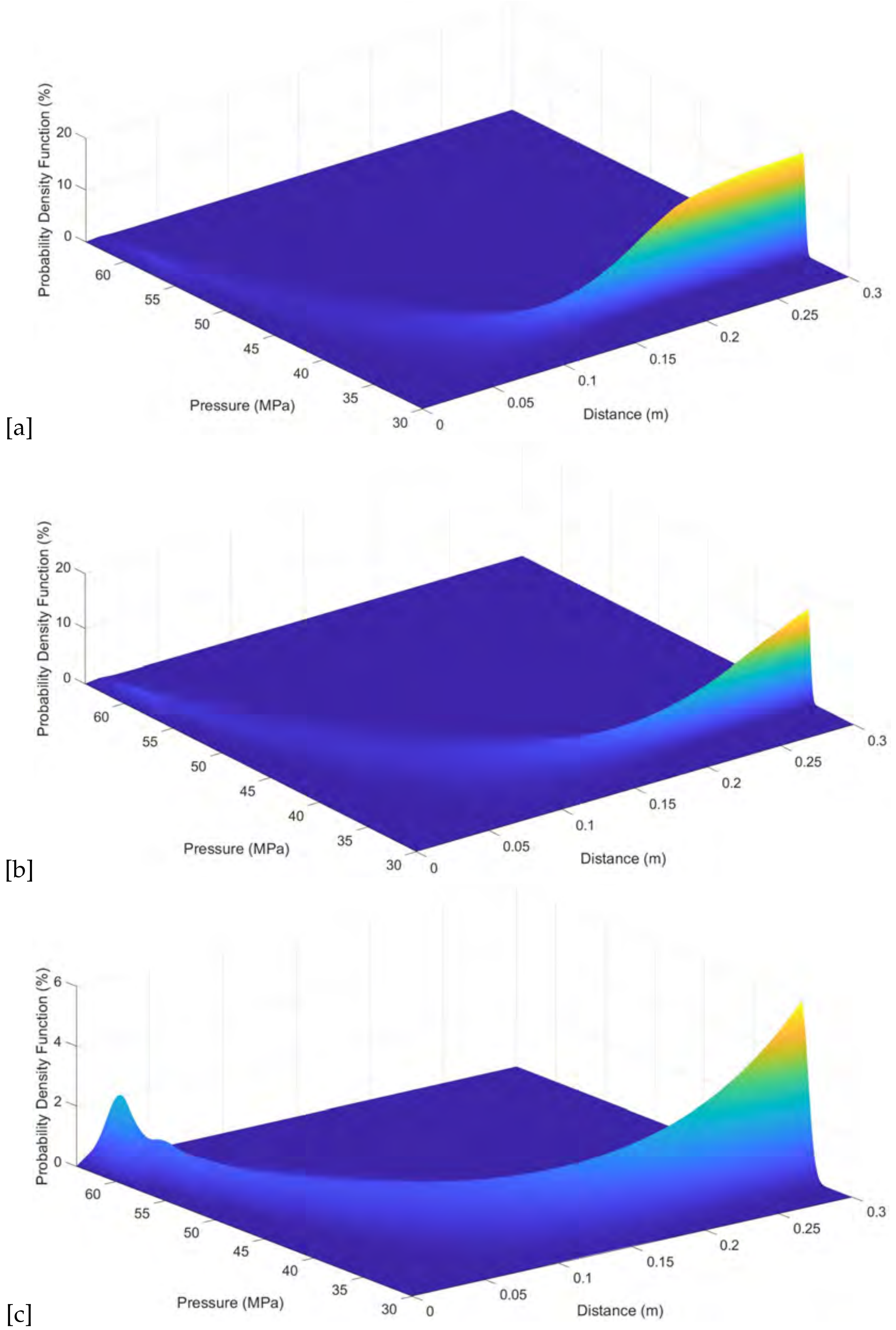

FIGURE A.11: Probability density functions for pressure at times a) $t = 15$ [min], b) $t = 30$ [min] and c) $t = 60$ [min].

reaches 0.2 [m]. Also, it is important to talk about the standard deviation because it indicates the amount of dispersion or variation observed in the population (Kanj, Abousleiman, and Ghanem, 2003). The pressure PDF follows a normal distribution function and has the highest standard deviation at t=15 [min], which decreases with time, where the PDF curve becomes sharper at 30 [min] and 60 [min]. Figures A.12(a)-(c) show the probability density functions (PDF) of the thermal diffusion, assuming a random thermal conductivity λ_1 and a random overall heat capacity ρC_v , calculated at times $t = 15$ [min], $t = 30$ [min], and $t = 60$ [min], respectively. Like pressure, PDF of the temperature at the shale-fracture boundary is 100% (constant injection temperature of 30 [$^{\circ}$C]) and is not included in the plots. The thermal diffusion front fits a normal distribution function and shows that the temperature of the porous medium decreases as a cooling front progresses deeper inside the medium to reach a depth of about 0.13 [m] at $t = 60$ [min] (Figure A.12(c)). The temperature also follows a normal distribution PDF, where its standard deviation, contrary to the pore pressure, does not seem to decrease with time. Figure A.13 shows the transient PDF of the leakoff velocity characterized by a normal distribution function. The leakoff velocity is the Darcy flow at the shale-fracture interface, which depends on the pore pressure gradient and is highest in the beginning of the injection 1.5x10-3 [m s^{-1}] and slows down to 0.3x10-3 [m s^{-1}] after 30 [min] of injection, as the pressure gradient nears zero.

Finally, Figure A.14 shows the PDF of the transient fracture width, assuming the variability of the four input parameters (Table A.4) for time interval [0,60] [min]. The mean fracture width is 0.72 [mm] at $t = 0^+$ and 0.84 [mm] at $t = 60$ [min]. All possible values of fracture width fit a normal distribution and fall within a narrow range with a standard deviation of $\sigma = 0.04$ [mm] at $t = 0^+$, then the range of variation widens, and the standard deviation is $\sigma = 0.15$ [mm] at $t = 60$ [min]. The reason for this is that, at early times the fracture width evolution is an elastic problem, depending primarily on one parameter Young's modulus E_1, and with time becomes a poro-thermo-elastic problem that depends on both the thermal and hydraulic properties, therefore simultaneously considering random parameters (Young's modulus E_1, linear thermal expansion coefficient α^s, the mobility ratio κ_1 and the thermal conductivity λ_1).

A.5 Discussion of Findings

When ranking the parameters by order of influence on the solution, one must pay attention to the parameters with high variability as this may affect the sensitivity score. In this problem, the mobility ratio, thermal conductivity and thermal expansion coefficient are high variability parameters (Table A.3) and are also the dominating parameters for the pressure solution (Figure A.7). Although high

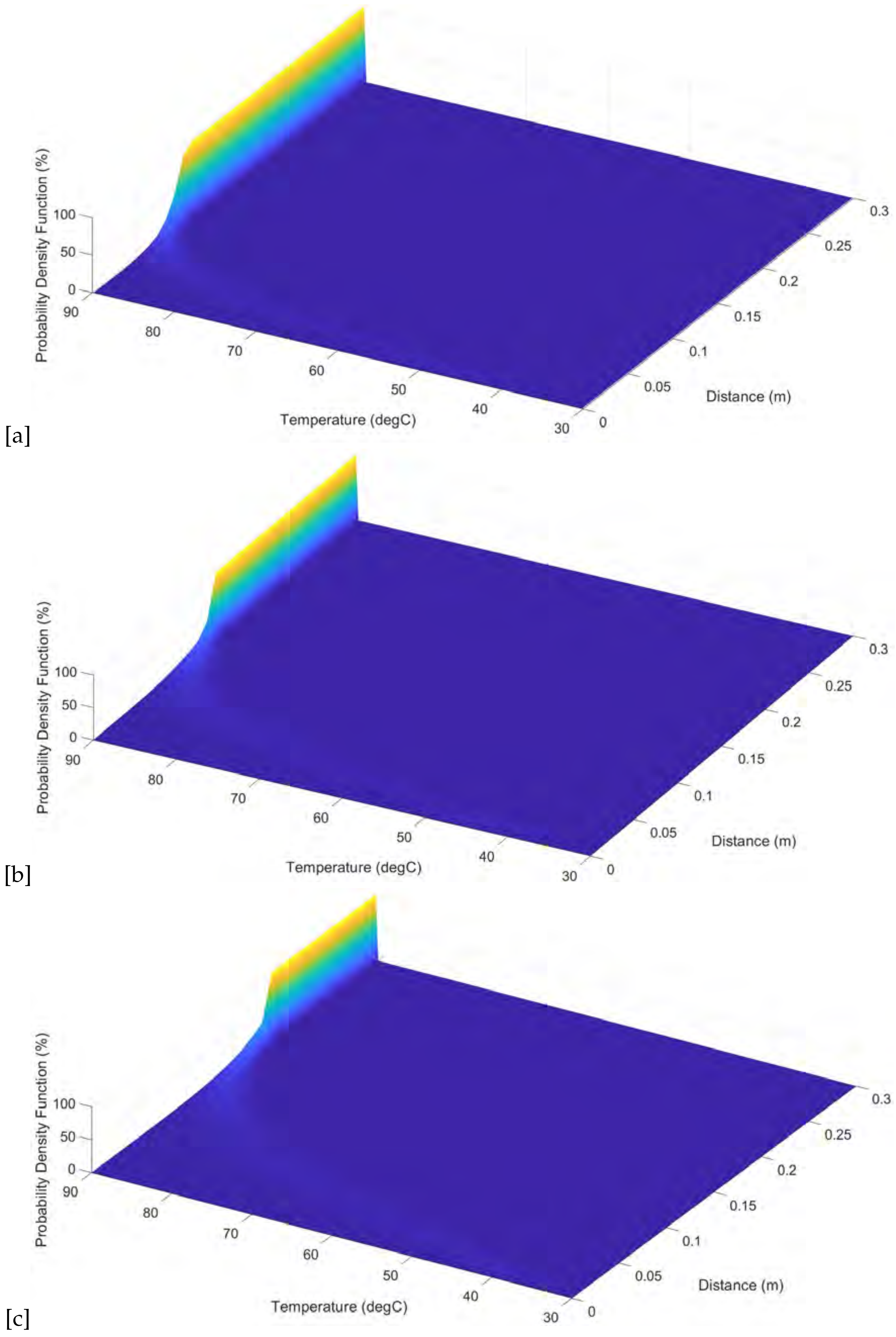

FIGURE A.12: Probability density functions for temperature at times a) $t = 15$ [min], b) $t = 30$ [min] and c) $t = 60$ [min].

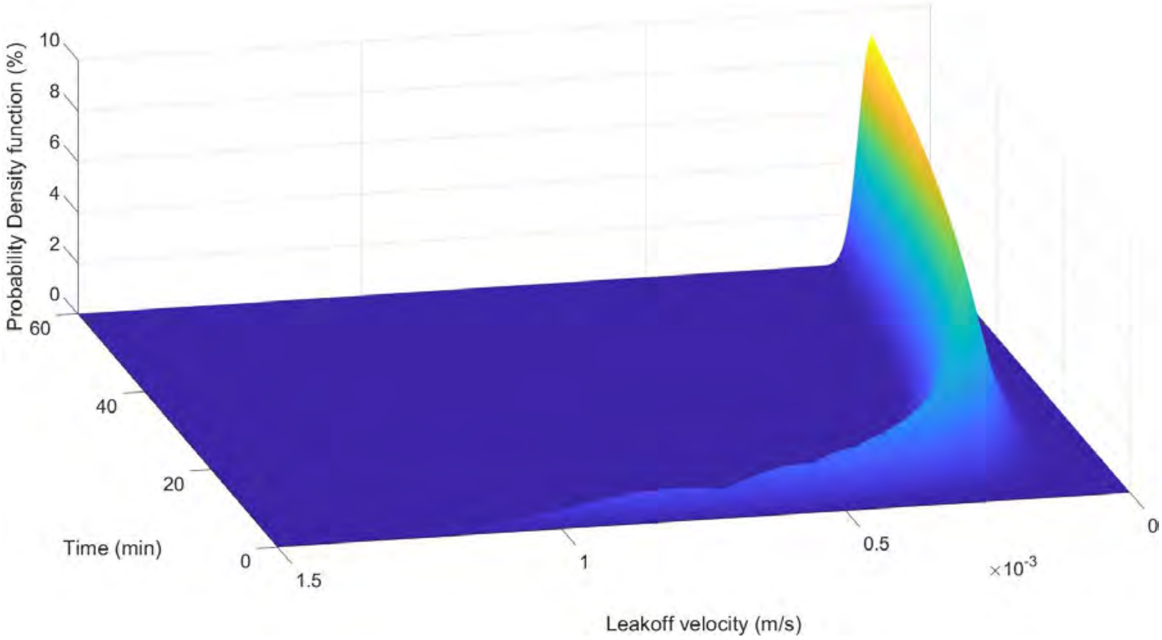

FIGURE A.13: Probability density function of the leakoff velocity at different for time interval $t = [0, 60]$ [min].

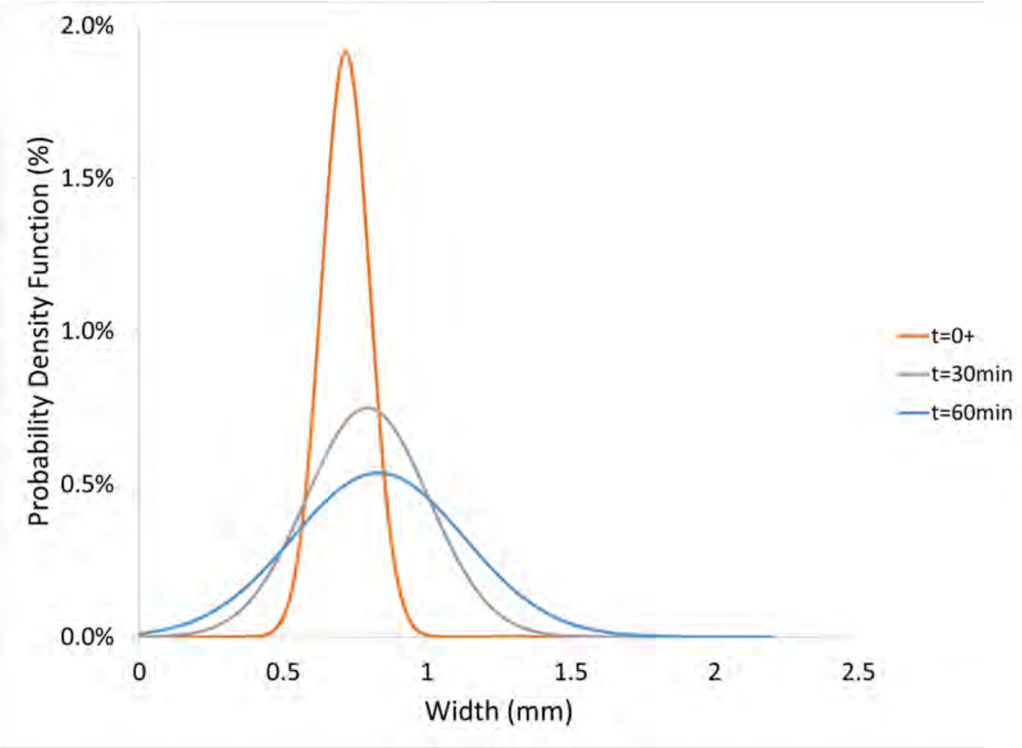

FIGURE A.14: Probability density function for fracture width at different for time interval $t = [0, 60]$ [min].

variability affects the sensitivity score, it does not eliminate the reliability of the method, because its main purpose is to rank the contributing parameters, as can be seen in Figure A.8 where ρC_v does not have a large variability but is the second most important parameter in the temperature solution. Results also show that temperature takes longer than pressure to stabilize in the system, clearly depicted in the resonance of the sensitivity curves in Figure A.8. While at 30 [min] the pressure sensitivity ranking curves stabilize, the temperature ones stabilize only at 60 [min]. Figure A.9 shows that the sensitivity ranking for the leakoff velocity, that is Darcy flow at the shale-fracture interface, depends primarily on the mobility ratio, where its sensitivity score remains constant after 5 [min], thus indicating that the pressure gradient tends to zero and consequently generates a slow leakoff. Figure A.10 shows that the fracture width evolution depends initially only on the elastic parameter E_1, and with time becomes mainly driven by thermal effects and depends primarily on the thermal expansion coefficient α^s of the rock. Figure A.11 shows that the applied excess pore pressure at the shale-fracture interface leads to an instantaneous pore pressure jump in the medium with a variability of [30-35] [MPa], and then as time progresses, pressure diffuses further and deeper into the formation. We can also note that the normal distribution of the PDF of the pressure becomes narrower with time, meaning that as time progresses, the effects of the variability in formation properties decreases. Figure A.12 clearly shows the temperature diffusion, where the cooling front reaches $x < 0.08$ [m] after 15 [min] and $x < 0.12$ [m] at 30 [min] and $x < 0.175$ [m] at 60 [min]. Results also show that the standard deviation of the temperature PDF is independent of time. Further, Darcy flow at the shale-fracture interface (the leakoff) stabilizes after 20 [min] (Figure A.13), thus meaning that pressure at the boundary is reaching a constant value. Finally, the PDF of the fracture width (Figure A.14) provides its range of possible values and corresponding likelihood, which in turn determines if proppants will fit inside the created fracture. Figure A.15 shows the "most likely" fracture width for three different time steps, $t = 0^+$, $t = 30$[min]and $t = 60$[min]. Because of the thermal gradient at the shale-fracture interface, fracture width is continuously widening to reach a range of 0-1.5 [mm] after 60 [min] of injection, which means that one must wait before pumping proppants to profit from this mechanism. (Abousleiman, Hoang et al. 2014) found that fracture aperture can be as much as 70% larger when the temperature gradient at the interface is 60 [$^\circ C$], contrary to when the rock and the injected fluid have the same temperature, in which case the fracture width starts to decrease shortly after pumping.

A proper combination of fracturing fluid and proppant kind/mesh size is paramount for a successful fracture job. The industry designs proppants to migrate far enough, thus maintaining a sufficient length/width of the fracture, and to keep the induced hydraulic fracture open, thus providing good fracture conductivity. According to API standards two types of proppant mesh/size are primarily used in the field: $D_{20/40}$ with a diameter of 0.69 [mm] and $D_{40/70}$ with a diameter of 0.33 [mm]. I test the agreement between the width PDF and the industry preferred proppant mixture of

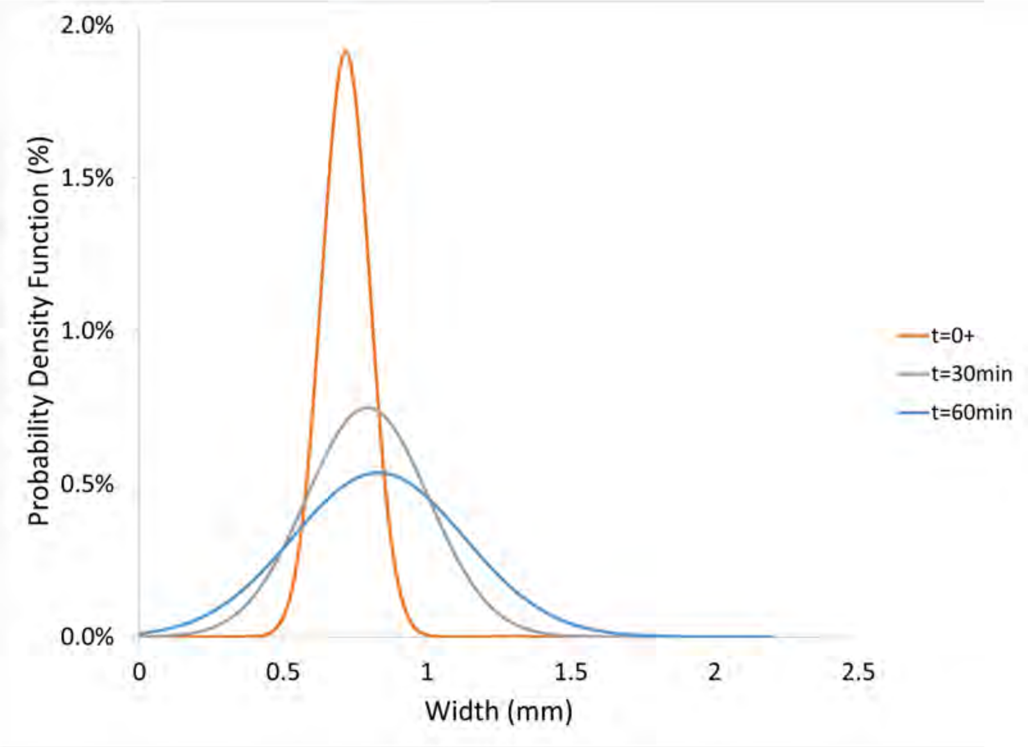

FIGURE A.15: Probability density function of the fracture width at different time steps.

D_{100} (0.152 [mm]) (60%) and $D_{40/70}$ (40%) and find that the probability that the proppants and $D_{40/70}$ will fit inside the fracture at $t = 0^{+}$, is 63% and 100%, respectively (Figure A.16). Consequently, the mixture of 60% D_{100} and 40% $D_{40/70}$ has a probability success rate of 100%, which is observed in the field.

Figure A.17 shows the PDF for the fracture aperture at $t = 60$ [min], where the probability that the proppants $D_{20/40}$ and $D_{40/70}$ will fit the fracture is 68% and 96%, respectively. This explains the success rate of the 60% D_{100} and 40% $D_{40/70}$ mixture even at larger times

A.6 Conclusions

I investigate here two important parts of uncertainty quantification in hydraulic fracture responses: sensitivity analysis and probability density functions. The study examines the impact of the uncertainty in the formation properties on the one-dimensional problem output solution. The analysis indicates that a large variability in the formation properties propagate a large uncertainty in the fracture responses, most importantly the fracture width. The result is consistent with field observations of successful proppant size, thus proving that uncertainty quantification for fracture width can be a powerful decision-making tool to seek critical proppant mesh/size. Nevertheless, the investigated

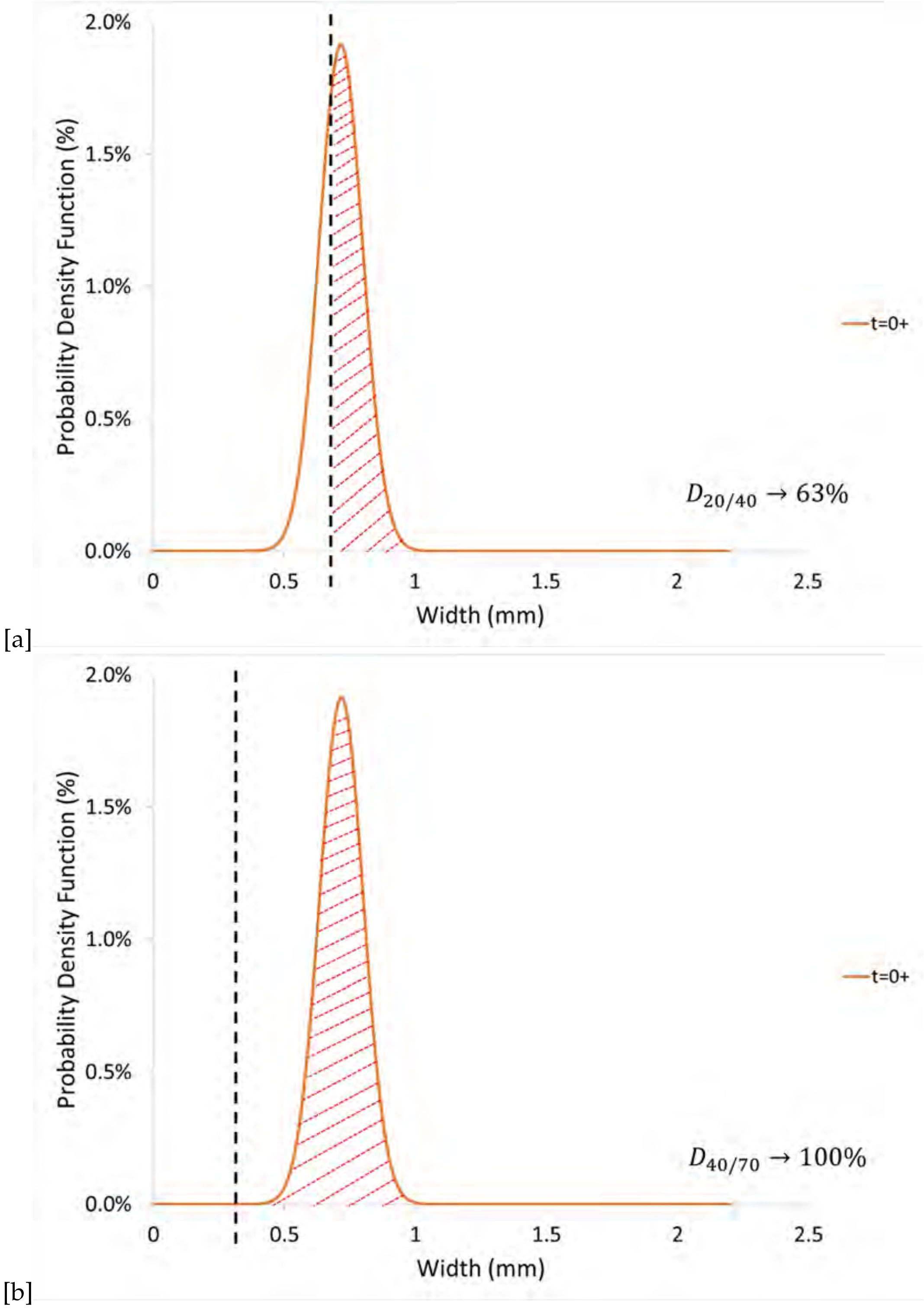

FIGURE A.16: PDF of the fracture width at t=0+. The probability of the proppant to fit inside the created fracture width is represented by the hashed area. Success rate of (a) 63% for $D20/40$ and (b) 100% for $D40/70$.

problem has some limitations. First, the one-dimensional solution is limited to model the flow of a Newtonian fluid with a constant viscosity, independent from both pressure and temperature. Further, we assume the fracturing fluid pressure and temperature inside the apertures to be constant

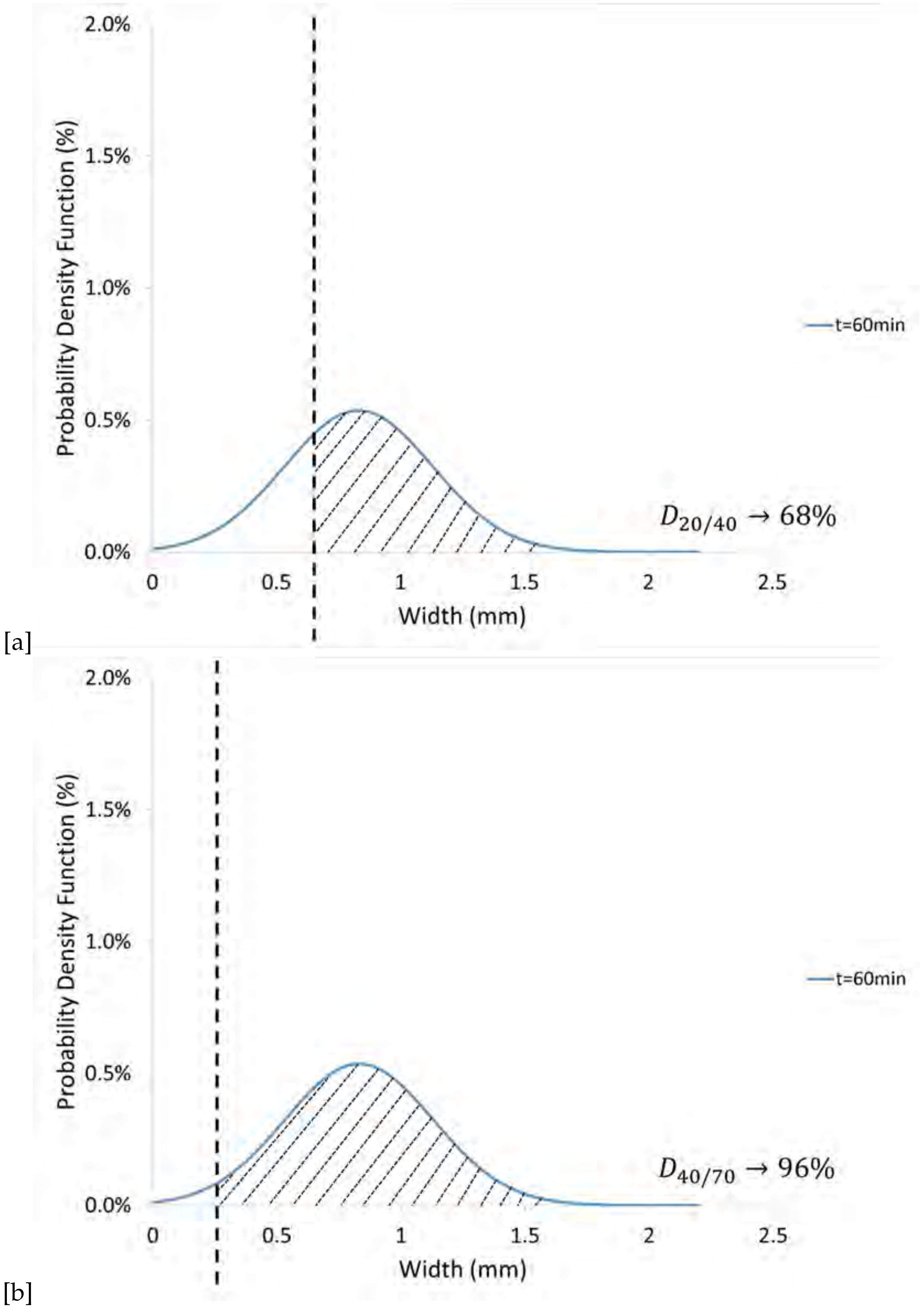

FIGURE A.17: Probability density function of the fracture width at $t = 60$ [min]. The probability of the proppant to fit inside the created fracture width is represented by the hashed area. Success rate of 68% for $D20/40$ and 96% for $D40/70$.

throughout the stimulation period and only address the leakoff and heat transfer from the fracture into the formation. Secondly, despite the simplicity of the Monte-Carlo methods and their robustness, they have the disadvantage of a slow convergence rate and consequently require a large sampling of the stochastic (or random) input parameters. To determine the variability induced on the solution, one must repeatedly calculate the solution with the generated population of random input parameters. Furthermore, these methods are limited to the local variability of the solution because the impact of the input uncertainties is not simultaneously considered (one at a time) to avoid long computation times and computer crashes. In conclusion, uncertainty quantification (UQ) is a large field of study where some methods may be more effective than others depending on the complexity of the problem. The choice of the optimum statistical method is usually achieved through trial and error and past literature review. Other statistical methods characterized by lower computational time and population size include the spectral methods and dimensional analysis and are worth further developing with application to hydraulic fracturing.

A.7 Data Availability

Data is available upon reasonable request.

A.8 Conflicts of Interest

The author declares that there is no conflict of interest regarding the publication of this paper.

A.9 Funding Statement

This publication is supported by the University of Neuchâtel.

A.10 Acknowledgments

The author appreciates helpful comments from Stephen A. Miller.

Bibliography

Abousleiman, Younane N, Son K Hoang, and Chao Liu (2014). "Anisotropic porothermoelastic solution and hydro-thermal effects on fracture width in hydraulic fracturing". In: *International Journal for Numerical and Analytical Methods in Geomechanics* 38.5, pp. 493–517.

Abousleiman, Younane N et al. (2007). "Geomechanics field and laboratory characterization of the Woodford Shale: The next gas play". In: *SPE Annual Technical Conference and Exhibition*. OnePetro.

Aoudia, Khodir (2009). "Analysis of rock mechanical properties by mineralogy and their potential effects on hydraulic fracturing in the Woodford Shale, West Texas". PhD thesis. Colorado School of Mines.

Audet, Pascal and Roland Bürgmann (2014). "Possible control of subduction zone slow-earthquake periodicity by silica enrichment". In: *Nature* 510.7505, pp. 389–392.

Audet, Pascal and Susan Y Schwartz (2013). "Hydrologic control of forearc strength and seismicity in the Costa Rican subduction zone". In: *Nature Geoscience* 6.10, pp. 852–855.

Audet, Pascal et al. (2009). "Seismic evidence for overpressured subducted oceanic crust and megathrust fault sealing". In: *Nature* 457.7225, pp. 76–78.

Audet, Pascal et al. (2010). "Slab morphology in the Cascadia fore arc and its relation to episodic tremor and slip". In: *Journal of Geophysical Research: Solid Earth* 115.B4.

Beroza, Gregory C and Satoshi Ide (2011). "Slow earthquakes and nonvolcanic tremor". In: *Annual review of Earth and planetary sciences* 39, pp. 271–296.

Berrone, Stefano et al. (2018). "Uncertainty quantification in discrete fracture network models: Stochastic geometry". In: *Water Resources Research* 54.2, pp. 1338–1352.

Bödvarsson, Gunnar (1960). "Exploration and exploitation of natural heat in Iceland". In: *Bulletin Volcanologique* 23.1, pp. 241–250.

Browne, PRL (1978). "Hydrothermal alteration in active geothermal fields". In: *Annual review of earth and planetary sciences* 6, pp. 229–250.

Canals, Martin and Jean Dominique Meunier (1995). "A model for porosity reduction in quartzite reservoirs by quartz cementation". In: *Geochimica et Cosmochimica Acta* 59.4, pp. 699–709.

Civan, Faruk (2001). “Scale effect on porosity and permeability: Kinetics, model, and correlation”. In: *AIChE journal* 47.2, pp. 271–287.

Collettini, C and RE Holdsworth (2004). “Fault zone weakening and character of slip along low-angle normal faults: insights from the Zuccale fault, Elba, Italy”. In: *Journal of the Geological Society* 161.6, pp. 1039–1051.

Costa, Antonio (2006). “Permeability-porosity relationship: A reexamination of the Kozeny-Carman equation based on a fractal pore-space geometry assumption”. In: *Geophysical research letters* 33.2.

De Marsily, Ghislain (1986). *Quantitative hydrogeology*. Tech. rep. Paris School of Mines, Fontainebleau.

Delgado, Paul and Vinod Kumar (2014). “A stochastic Galerkin approach to uncertainty quantification in poroelastic media”. In: *Fluids Engineering Division Summer Meeting*. Vol. 46247. American Society of Mechanical Engineers, V01DT40A002.

Dempsey, DE et al. (2012). “Modeling the effects of silica deposition and fault rupture on natural geothermal systems”. In: *Journal of Geophysical Research: Solid Earth* 117.B5.

Economides, Michael J (2013). *Petroleum production systems*. Pearson Education.

Galvan, Boris and Stephen Miller (2013). “A full GPU simulation of evolving fracture networks in a heterogeneous poro-elasto-plastic medium with effective-stress-dependent permeability”. In: *GPU solutions to multi-scale problems in science and engineering*. Springer, pp. 305–319.

Ghassemi, Ahmad and G Suresh Kumar (2007). “Changes in fracture aperture and fluid pressure due to thermal stress and silica dissolution/precipitation induced by heat extraction from subsurface rocks”. In: *Geothermics* 36.2, pp. 115–140.

Ghassemi, Ahmad, Andrew Nygren, and Alexander Cheng (2008). “Effects of heat extraction on fracture aperture: A poro–thermoelastic analysis”. In: *Geothermics* 37.5, pp. 525–539.

Giger, Silvio B et al. (2007). “Permeability evolution in quartz fault gouges under hydrothermal conditions”. In: *Journal of Geophysical Research: Solid Earth* 112.B7.

Gilliam, TM and IL Morgan (1987). *Shale: Measurement of thermal properties*. Tech. rep. Oak Ridge National Lab., TN (USA).

Gisler, Batoul M (2021). “Uncertainty Quantification for a Hydraulic Fracture Geometry: Application to Woodford Shale Data”. In: *Geofluids* 2021.

Gisler, Batoul M and Stephen A Miller (2021). “A thermo-hydro-chemical model with porosity reduction and enthalpy production: Application to silica precipitation in geothermal reservoirs”. In: *Energy Reports* 7, pp. 6260–6272.

Hammond, Glenn E, Peter C Lichtner, and RT Mills (2014). "Evaluating the performance of parallel subsurface simulators: An illustrative example with PFLOTRAN". In: *Water resources research* 50.1, pp. 208–228.

Heinrich, DH et al. (2014). "Treatise on geochemistry". In: *Pergamon, Oxford, pp 181222Giggenbach WF (1992a) The composition of gases in geothermal and volcanic systems as a function of tectonic setting. In: Kharaka YF, Maest AS (eds) Waterrock interaction: Proceedings WRI-7, vols* 1, 873878Giggenbach.

Henley, Richard W and Alan John Ellis (1983). "Geothermal systems ancient and modern: a geochemical review". In: *Earth-science reviews* 19.1, pp. 1–50.

Horne, Roland N (1982). "Geothermal reinjection experience in Japan". In: *Journal of Petroleum Technology* 34.03, pp. 495–503.

Huene, Roland von and Cesar R Ranero (2003). "Subduction erosion and basal friction along the sediment-starved convergent margin off Antofagasta, Chile". In: *Journal of Geophysical Research: Solid Earth* 108.B2.

Jaeger, John Conrad, Neville GW Cook, and Robert Zimmerman (2009). *Fundamentals of rock mechanics*. John Wiley & Sons.

Jansen, Gunnar and Stephen A Miller (2017). "On the role of thermal stresses during hydraulic stimulation of geothermal reservoirs". In: *Geofluids* 2017.

Kanj, Mazen, Younane Abousleiman, and Roger Ghanem (2003). "Poromechanics of anisotropic hollow cylinders". In: *Journal of engineering mechanics* 129.11, pp. 1277–1287.

Kennedy, George Clayton (1950). "A portion of the system silica-water". In: *Economic geology* 45.7, pp. 629–653.

Kittilä, Anniina et al. (2020). "Solute tracer test quantification of the effects of hot water injection into hydraulically stimulated crystalline rock". In: *Geothermal Energy* 8, pp. 1–21.

Koerner, A, E Kissling, and SA Miller (2004). "A model of deep crustal fluid flow following the Mw= 8.0 Antofagasta, Chile, earthquake". In: *Journal of Geophysical Research: Solid Earth* 109.B6.

Koponen, A, M Kataja, and J Timonen (1997). "Permeability and effective porosity of porous media". In: *Physical Review E* 56.3, p. 3319.

Kumar, G Suresh and Ahmad Ghassemi (2005). "Numerical modeling of non-isothermal quartz dissolution/precipitation in a coupled fracture–matrix system". In: *Geothermics* 34.4, pp. 411–439.

Kutun, Kaan, Omer Inanc Tureyen, and Abdurrahman Satman (2014). "Temperature behavior of geothermal wells during production, injection and shut-in operations". In: *proceedings, 39th workshop on geothermal reservoir engineering, Stanford University, Stanford, California*.

Lashkaripour, Gholam Reza (2002). “Predicting mechanical properties of mudrock from index parameters”. In: *Bulletin of Engineering Geology and the Environment* 61.1, pp. 73–77.

Lashkaripour, Gholam Reza and Maurice B Dusseault (2020). “A statistical study on shale properties: Relationships among principal shale properties”. In: *Probabilistic Methods in Geotechnical Engineering*. CRC Press, pp. 195–200.

Le Maître, Olivier and Omar M Knio (2010). *Spectral methods for uncertainty quantification: with applications to computational fluid dynamics*. Springer Science & Business Media.

Lee, Changyeol and YoungHee Kim (2021). “Role of warm subduction in the seismological properties of the forearc mantle: An example from southwest Japan”. In: *Science Advances* 7.28, eabf8934.

Lee, Changyeol, Donghoon Seoung, and Nestor G Cerpa (2021). “Effect of water solubilities on dehydration and hydration in subduction zones and water transport to the deep mantle: Implications for natural subduction zones”. In: *Gondwana Research* 89, pp. 287–305.

Lei, Qinghua, Nima Gholizadeh Doonechaly, and Chin-Fu Tsang (2021). “Modelling fluid injection-induced fracture activation, damage growth, seismicity occurrence and connectivity change in naturally fractured rocks”. In: *International Journal of Rock Mechanics and Mining Sciences* 138, p. 104598.

Lima, Marina Grimm et al. (2019). “Thermally driven fracture aperture variation in naturally fractured granites”. In: *Geothermal Energy* 7.1, pp. 1–28.

Lubawski, Wojciech and Wacław Marzantowicz (2015). “Invariant topological complexity”. In: *Bulletin of the London Mathematical Society* 47.1, pp. 101–117.

Ma, Xiang and Nicholas Zabaras (2011). “A stochastic mixed finite element heterogeneous multiscale method for flow in porous media”. In: *Journal of Computational Physics* 230.12, pp. 4696–4722.

Manning, Craig E (1994). “The solubility of quartz in H2O in the lower crust and upper mantle”. In: *Geochimica et Cosmochimica Acta* 58.22, pp. 4831–4839.

Miller, SA et al. (2003). “A fluid-pressure feedback model of dehydration reactions: experiments, modelling, and application to subduction zones”. In: *Tectonophysics* 370.1-4, pp. 241–251.

Miller, Stephen A (2015). “Modeling enhanced geothermal systems and the essential nature of large-scale changes in permeability at the onset of slip”. In: *Geofluids* 15.1-2, pp. 338–349.

— (2020). “Aftershocks are fluid-driven and decay rates controlled by permeability dynamics”. In: *Nature communications* 11.1, pp. 1–11.

Miller, Stephen A and Amos Nur (2000). “Permeability as a toggle switch in fluid-controlled crustal processes”. In: *Earth and Planetary Science Letters* 183.1-2, pp. 133–146.

Miller, Stephen A et al. (2004). “Aftershocks driven by a high-pressure CO2 source at depth”. In: *Nature* 427.6976, pp. 724–727.

Morey, GW, RO Fournier, and JJ Rowe (1962). “The solubility of quartz in water in the temperature interval from 25 to 300 C”. In: *Geochimica et Cosmochimica Acta* 26.10, pp. 1029–1043.

Nejadi, Siavash et al. (2015). “Integrated characterization of hydraulically fractured shale-gas Reservoirs—Production history matching”. In: *SPE Reservoir Evaluation & Engineering* 18.04, pp. 481–494.

Pandey, SN and A Chaudhuri (2017). “The effect of heterogeneity on heat extraction and transmissivity evolution in a carbonate reservoir: A thermo-hydro-chemical study”. In: *Geothermics* 69, pp. 45–54.

Pandey, SN, Vikram Vishal, and A Chaudhuri (2018). “Geothermal reservoir modeling in a coupled thermo-hydro-mechanical-chemical approach: a review”. In: *Earth-Science Reviews* 185, pp. 1157–1169.

Pandey, SN et al. (2014). “Investigation of permeability alteration of fractured limestone reservoir due to geothermal heat extraction using three-dimensional thermo-hydro-chemical (THC) model”. In: *Geothermics* 51, pp. 46–62.

Pandey, SN et al. (2015). “Fracture transmissivity evolution due to silica dissolution/precipitation during geothermal heat extraction”. In: *Geothermics* 57, pp. 111–126.

Peacock, Simon M (2009). “Thermal and metamorphic environment of subduction zone episodic tremor and slip”. In: *Journal of Geophysical Research: Solid Earth* 114.B8.

Peacock, Simon M et al. (2011). “High pore pressures and porosity at 35 km depth in the Cascadia subduction zone”. In: *Geology* 39.5, pp. 471–474.

Pieraccini, Sandra (2020). “Uncertainty quantification analysis in discrete fracture network flow simulations”. In: *GEM-International Journal on Geomathematics* 11.1, pp. 1–21.

Portas Arroyal, Romina Marisa (2009). “Characterization and origin of fracture patterns in the Woodford Shale in southeastern Oklahoma for application to exploration and development”. In.

Raleigh, CB and MS Paterson (1965). “Experimental deformation of serpentinite and its tectonic implications”. In: *Journal of Geophysical Research* 70.16, pp. 3965–3985.

Ramachandran, K and RD Hyndman (2012). “The fate of fluids released from subducting slab in northern Cascadia”. In: *Solid Earth* 3.1, pp. 121–129.

Rawal, Chakra and Ahmad Ghassemi (2014). “A reactive thermo-poroelastic analysis of water injection into an enhanced geothermal reservoir”. In: *Geothermics* 50, pp. 10–23.

Rimstidt, James Donald and HL Barnes (1980). “The kinetics of silica-water reactions”. In: *Geochimica et Cosmochimica Acta* 44.11, pp. 1683–1699.

Robinson, Bruce A and John Pendergrass (1989). *A combined heat transfer and quartz dissolution/deposition model for a hot dry rock geothermal reservoir*. Tech. rep. Los Alamos National Lab., NM (USA).

Rybach, Ladislaus and Leroy J Patrick Muffler (1981). “Geothermal systems: principles and case histories”. In: *Chichester*.

Satman, Abdurrahman et al. (2017). “Effect of Carbon Dioxide Content on the Well and Reservoir Performances in the Kizildere Geothermal Field”. In: *Proceedings*.

Schwartz, Susan Y and Juliana M Rokosky (2007). “Slow slip events and seismic tremor at circum-Pacific subduction zones”. In: *Reviews of Geophysics* 45.3.

Scott, Samuel W and Thomas Driesner (2018). “Permeability changes resulting from quartz precipitation and dissolution around upper crustal intrusions”. In: *Geofluids* 2018.

Scott, Samuel Warren (2017). “The thermo-hydraulic structure of high-enthalpy geothermal systems”. PhD thesis. ETH Zurich.

Sierra, R et al. (2010). “Woodford shale mechanical properties and the impacts of lithofacies”. In: *44th US rock mechanics symposium and 5th US-Canada rock mechanics symposium*. OnePetro.

Simpson, Guy (2017). *Practical finite element modeling in earth science using matlab*. Wiley Online Library.

Sohrabi, Reza, Samuel Omlin, and Stephen A Miller (2019). “GEYSER: 3D thermo-hydrodynamic reactive transport numerical simulator including porosity and permeability evolution using GPU clusters”. In: *Computational Geosciences* 23.6, pp. 1317–1330.

Steefel, Carl I (1994). “Coupled model for transport of multiple chemical species and kinetic precipitation/dissolution reactions with application to reactive flow in single phase hydrothermal systems”. In: *Am. J. Sci.* 294, pp. 529–592.

Steefel, Carl I, Donald J DePaolo, and Peter C Lichtner (2005). “Reactive transport modeling: An essential tool and a new research approach for the Earth sciences”. In: *Earth and Planetary Science Letters* 240.3-4, pp. 539–558.

Steefel, Carl I and Peter C Lichtner (1998). “Multicomponent reactive transport in discrete fractures: I. Controls on reaction front geometry”. In: *Journal of Hydrology* 209.1-4, pp. 186–199.

Sulem, Jean and Vincent Famin (2009). “Thermal decomposition of carbonates in fault zones: Slip-weakening and temperature-limiting effects”. In: *Journal of Geophysical Research: Solid Earth* 114.B3.

Tester, Jefferson W et al. (2006). "The future of geothermal energy". In: *Massachusetts Institute of Technology* 358.

Valkó, Peter and Michael J Economides (1995). *Hydraulic fracture mechanics*. Vol. 28. Wiley Chichester.

Wada, Ikuko et al. (2008). "Weakening of the subduction interface and its effects on surface heat flow, slab dehydration, and mantle wedge serpentinization". In: *Journal of Geophysical Research: Solid Earth* 113.B4.

Walder, Joseph and Amos Nur (1984). "Porosity reduction and crustal pore pressure development". In: *Journal of Geophysical Research: Solid Earth* 89.B13, pp. 11539–11548.

Wang, Qiqi (2009). *Uncertainty quantification for unsteady fluid flow using adjoint-based approaches*. Stanford University.

Weatherley, Dion K and Richard W Henley (2013). "Flash vaporization during earthquakes evidenced by gold deposits". In: *Nature Geoscience* 6.4, pp. 294–298.

Weir, Graham J and Stephen P White (1996). "Surface deposition from fluid flow in a porous medium". In: *Transport in Porous Media* 25.1, pp. 79–96.

Wohletz, Kenneth and Grant Heiken (1992). *Volcanology and geothermal energy*. Vol. 432. University of California Press Berkeley.

Xu, Peng and Boming Yu (2008). "Developing a new form of permeability and Kozeny–Carman constant for homogeneous porous media by means of fractal geometry". In: *Advances in water resources* 31.1, pp. 74–81.

Xu, Tianfu (1998). "Coupled modeling of non-isothermal multiphase flow, solute transport and reactive chemistry in porous and fractured media: 2. Model Applications". In.

Yanaze, Takumi et al. (2019). "Prediction of permeability reduction due to silica scale deposition with a geochemical clogging model at Sumikawa Geothermal Power Plant". In: *Geothermics* 79, pp. 114–128.

Yariv, Shmuel and Harold Cross (1979). "Colloid geochemistry of clay minerals". In: *Geochemistry of Colloid Systems*. Springer, pp. 287–333.

Yu, Boming and Jianhua Li (2001). "Some fractal characters of porous media". In: *Fractals* 9.03, pp. 365–372.

Zio, Souleymane and Fernando A Rochinha (2012). "A stochastic collocation approach for uncertainty quantification in hydraulic fracture numerical simulation". In: *International Journal for Uncertainty Quantification* 2.2.

Zoback, Mark D (2010). *Reservoir geomechanics*. Cambridge University Press.